POST-STALL HYSTERESIS AND FLOW FIELD UNSTEADINESS ON AN NACA 0012 AIRFOIL

BY

GEORGI HRISTOV

THESIS

Submitted in partial fulfillment of the requirements
for the degree of Master of Science in Aerospace Engineering
in the Graduate College of the
University of Illinois at Urbana-Champaign, 2017

Urbana, Illinois

Adviser:

Assistant Professor Phillip J. Ansell

Abstract

The current study was conducted to understand flow field unsteadiness associated with static stall hysteresis on an NACA 0012 airfoil at $Re_c = 1.0 \times 10^6$. Unsteady pressure measurements were acquired to evaluate the performance of the airfoil, and a hysteresis loop was identified in the vicinity of the airfoil $C_{l,max}$. Two fundamentally different flow regimes were observed at post-stall angles of attack for the airfoil during the upstroke and downstroke branches of the hysteresis loop. A Fourier analysis of the surface pressure distributions was used to attribute the flow field unsteadiness to a low-frequency, high-amplitude oscillation across the leading-edge region during the upstroke, along with a regular bluff-body shedding frequency across the separated region of the airfoil. The low-frequency oscillations were observed to be more dominant for the upstroke branch, while the bluff-body shedding process was more dominant in the downstroke branch. The flow field unsteadiness was observed to become more energetic at lower post-stall angles of attack. In addition, time-resolve particle image velocimetry data were acquired across the leading-edge region of the airfoil to qualitatively and quantitatively describe the unsteadiness in the flow. These data were used to link the low-frequency oscillations across the leading edge of the airfoil during the upstroke to a quasi-periodic surging of the flow, which was also associated with an advancing and retreating of the separation location across the surface.

Acknowledgements

First and foremost, I would like to thank my academic advisor at the University of Illinois at Urbana-Champaign, Prof. Phil Ansell. I am forever grateful for his continuous support for my Master's degree and related research, for his patience and guidance. My research would not have been complete without his active help. I consider myself fortunate to have him as my advisor.

I would also like to express my gratitude to my undergraduate advisor Prof. David Williams at the Illinois Institute of Technology who provided invaluable guidance during my first research experience and helped me achieve my academic goals.

I am thankful to my longtime friends as well as the friends I made at Illinois. They all made my experience in graduate school unforgettable. I am especially grateful to the people who have always been there for me and encouraged me through my darkest days. I am also thankful to all the members of the Aerodynamics and Unsteady Flows research group who have been great officemates and made the daily work experience more enjoyable. I am extremely grateful to everyone who spent time to help me with research or have an insightful conversation.

Finally, I would like to thank my entire family for their never-ending support and encouragement though the years away from home. I would not be the person I am today without my parents and I am forever indebted for their love and unwavering support.

Table of Contents

List of Figures

List of Tables

Nomenclature

List of Symbols

α	airfoil angle of attack
A_{ss}	cross-section area of the wind tunnel settling section
A_{ts}	cross-section area of the wind tunnel test section
b	span of the airfoil model
c	airfoil chord length
C_d	airfoil drag coefficient
C_l	airfoil lift coefficient
C_m	airfoil pitching moment coefficient
C_p	pressure coefficient
$C_{p,SD}$	standard deviation in the pressure coefficient
D	airfoil drag
ε	tunnel blockage velocity increment factor
f	dimensional frequency
F	aerodynamic forces
h	test section height
L	airfoil lift
M	airfoil pitching moment or Mach number
P	static pressure
P_o	total pressure
q	dynamic pressure
ρ	density
R	universal gas constant
Re_c	chord-based Reynolds number
σ	streamline curvature compensation factor
S	airfoil reference area
t	airfoil thickness
T	static temperature
T_u	Turbulence intensity

U	velocity or uncertainty
V	velocity magnitude
V_m	volume of the airfoil model
ω	vorticity
x	airfoil chordwise direction
y	airfoil chord-normal direction

List of Abbreviations

EDM	electrical discharge machining
ESP	electronic pressure scanner
FFT	fast Fourier transform
PIV	particle image velocimetry
PSD	power spectral density
RMS	root mean square
RPM	rotations per minute
SCXI	signal conditioning eXtensions for instrumentation
SD	standard deviation
TR-PIV	time-resolved particle image velocimetry

Chapter 1

Introduction

Separated flows inevitably lead to losses in performance during stall of fixed wing aircraft, highly deflected control surfaces, stalled compressor or turbine blades, or other off-design conditions of aerodynamic geometries. The underlying physics of the stall process, whether static or dynamic, and the flow phenomena that occur with it are often poorly understood. One of the least understood stall-related phenomena, called hysteresis, is the ability of the flow to "remember" its past history. In this case, the flow state of an airfoil at a fixed instance is dependent on the preceding flow field conditions. The dynamic stall hysteresis associated with a rapidly pitching airfoil is a topic that has been intensively studied, but far less attention has been devoted to hysteresis in the static stall process. Large variability in the lift coefficient due to hysteresis at high angles of attack is often observed for airfoils operating in low Reynolds (Re) number flow regimes. The increased interest in low-speed flight due to the rapid development of unmanned aerial vehicles makes hysteresis of practical importance since it commonly appears across a wide range of cambered and symmetrical airfoils.

Previous approaches to understanding static stall hysteresis can be divided in three categories – experimental, computational, and theoretical. Numerical simulations have provided detailed data of the entire flow field for an airfoil, but they also tend to require adequate numerical models which are computationally expensive, limiting them to low Reynolds numbers. Theoretical

predictions have helped to provide an understanding of the underlying physics associated with stall hysteresis but making simplifying assumptions is often necessary. Finally, carefully-designed experiments require no modeling to produce an accurate representation of the flow but can be expensive to conduct.

1.1 Review of Literature

Biber and Zumwalt[1] reported that the stall hysteresis phenomenon occurs for not only single-element but also multi-element airfoils. Traub[2] tested airfoils ranging from highly cambered to symmetrical sections, including the NACA 0015 (t/c = 0.15), S8036 (t/c = 0.16), E591 (t/c = 0.157), and SD7062 (t/c = 0.14). Experiments were conducted for chord-based Reynolds numbers ranging from 40,000 to 160,000 and all airfoils exhibited hysteresis loops. It was established that there was a strong correlation between the presence of hysteresis and the airfoil thickness.

Early experimental studies on static stall hysteresis were performed by Pohlen and Mueller[3] and Mueller[4], who investigated the aerodynamic characteristics of Miley M06-13-128 and Lissaman 7769 airfoils at low Reynolds numbers. Using force balance measurements and smoke visualization, they found hysteresis loops in both airfoils when operated below chord-based Reynolds numbers of 300,000. Typical clockwise and counterclockwise hysteresis loops from the study are presented in Fig. 1.1. Qualitative flow visualization conducted by these authors suggested that the aerodynamic hysteresis is closely related to laminar separation bubbles and transition about the airfoils. More recently, Yang and Igarashi[5] experimentally investigated the static stall hysteresis characteristics of a NASA low-speed GA(W)-1 at Re_c = 160,000. The upstroke of the hysteresis loop was characterized by a marginally separated flow with low unsteadiness, whereas the downstroke was associated with large unsteadiness. It was again concluded that the hysteresis was closely related to the laminar boundary layer separation and laminar-turbulent transition on the airfoil.

In another study in the literature, Hoffmann[6] investigated the aerodynamic characteristics of an NACA 0015 airfoil at Re_c = 250,000 at various levels of freestream turbulence. Hysteresis could be observed for low freestream turbulence with up to 2% turbulence intensity. Qualitative oil flow visualization showed that the disappearance of the hysteresis for the high freestream turbulence cases was linked to the elimination of the laminar separation bubble.

Unlike the aforementioned studies which found that the presence of laminar transitional bubbles on the upper surface of the airfoil contributes to hysteresis, a computational study on an NACA 0012 by Mittal and Saxena[7] revealed a hysteretic-type behavior where transitional bubbles were absent. The hysteresis was, instead, attributed to a larger unsteady lift component for the decreasing angle of attack solution. It was noted that the difference in the location of the separation point between decreasing angles of attack and increasing angles of attack was correlated to the hysteresis loop.

Studies on airfoil stall have also revealed the presence of multiple mechanisms for periodic and quasi-periodic sources of flow field unsteadiness.[8-14] The unsteady flow about airfoils has generally been linked to vortex shedding processes from separation bubbles,[15] bluff-body shedding,[16] unsteady motions in shear layers,[17] or low-frequency unsteadiness represented by global oscillations in airfoil circulation.[8,18-21] Specific sources of unsteadiness are often linked to a universal Strouhal number scaling when the oscillation frequency of a given mode is normalized by the appropriate length and velocity scales. When considering bluff body shedding, the fundamental frequency is commonly attributed to the well-known shedding frequency of a Karman vortex street of St = 0.2 for a circular cylinder, though variations from this bluff-body Strouhal number exist with variations in geometry and Reynolds number.[16] Conversely, the low-frequency oscillation in an airfoil flow field has been linked to a feedback coupling of the viscous-inviscid flow regions, where separated flows act to decamber the airfoil, which leads to a change in circulation, which subsequently leads to changes in the separated flow region.[22] An example of such low-frequency oscillation observed in near stalling conditions is seen in Fig. 1.2 and in Fig. 1.3, after Zaman et al.[8,23] Until recently it was thought that such low-frequency oscillations were only present prior to stall at high angles of attack. However, a recent study by Bernardini et al.[21] showed that low-frequency oscillations can also be excited and exist in the post-stall flow field.

1.2 Research Motivation and Objectives

The extensively studied NACA 0012 section which has exhibited post-stall hysteresis was chosen for the current investigation. A study on airfoil stalling characteristics conducted by Gault[24] classified the NACA 0012 as a problematic section with respect to its stalling behavior, which lies on the boundary between two stalling types. Depending on the Reynolds number, it might have a trailing-edge stall or a combined leading-edge and trailing-edge type stall. According to Gault, a

trailing edge type stall is observed at all Reynolds numbers, which is characterized by an upstream movement of the turbulent separation point from the trailing edge with increasing angle of attack. However, as also mentioned by Gregory et al.[25], an intermediate range of Reynolds numbers exists over which the NACA 0012 airfoil stalling behavior is strongly influenced by a leading-edge type stall. This is characterized by a laminar separation of the flow in the leading-edge region. When the flow fails to reattach right after the laminar separation at the leading edge, the subsequent stall is accompanied by a sharp drop of lift. As the Reynolds number is increased, the laminar to turbulent flow transition would be expected to occur before the laminar flow separates. Thus, the stalling behavior at sufficiently high Reynolds numbers would be purely due to turbulent separation from the trailing edge. This complex stalling behavior of the NACA 0012, on the boundary between two stalling types, provides the perfect opportunity to study the stalling mechanisms at high angles of attack, and the unsteadiness associated with those flows.

The current study aims to facilitate the understanding of static stall, and the hysteresis effects that are associated with it, by directly investigating the unsteady flow physics across with the upstroke and downstroke branches of the hysteresis loop. Since not all earlier studies agree on the reasons for the onset of static stall hysteresis, the current study is expected to shed light on the different flow fields across each branch of the hysteresis loop and characterize the unsteady flow modes that contribute to the bistable state of the lift curve at high angles of attack. An advantage to previous investigations is the ability to operate at a significantly higher chord Reynolds numbers on the order of $Re_c = 1.0 \times 10^6$ ($M_\infty = 0.1$). The primary objectives of the current investigation can be summarized as follows:

- Identify the stalling behavior of the airfoil and the behavior of the C_l, C_m, and C_d polars.
- Understand the physics of the flow by considering the steady and unsteady pressures, and the spectral content of the flow.
- Study the temporal characteristics of the off-body flow by employing advanced flow visualization techniques.

1.3 Chapter 1 Figures

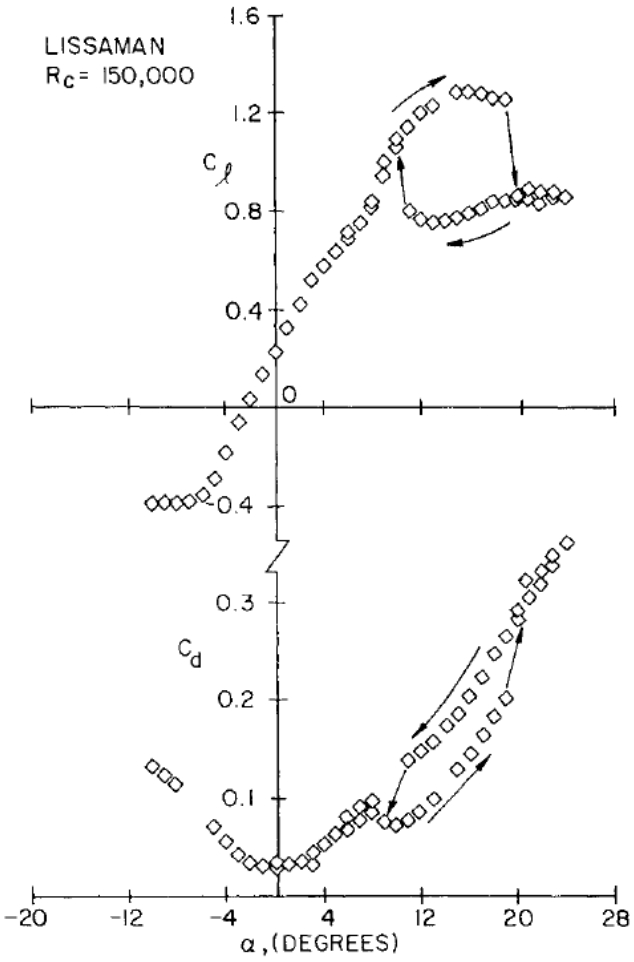

Fig. 1.1 Typical clockwise and counterclockwise hysteresis loops observed in C_l and C_d respectively on a Lissman 7769 airfoil at $Re_c = 1.5 \times 10^5$, after Mueller et al.[4]

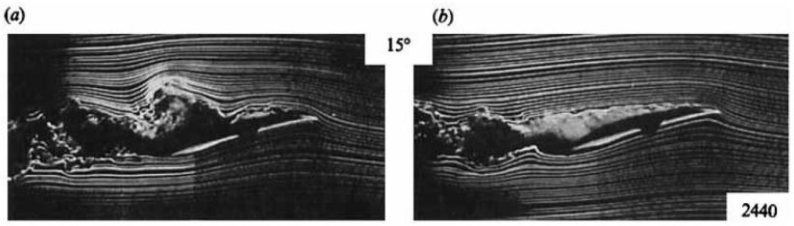

Fig. 1.2 Flow visualization at $Re_c = 0.40 \times 10^5$ and $\alpha = 15°$ (a) Natural low-frequency oscillation occuring at frequency $f = 4.5$ Hz; (b) The natural low-frequency oscillation is suppressed after actuation at frequency $f = 2440$ Hz, after Zaman et al.[23]

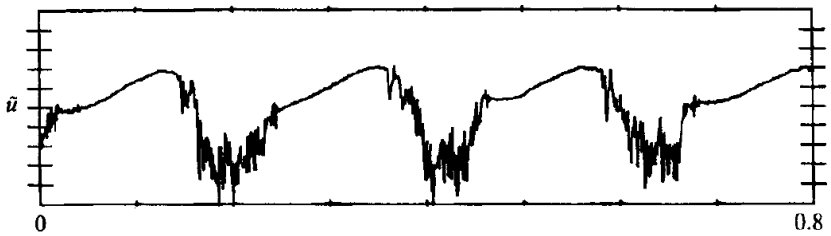

Fig. 1.3 A time trace of a single hot-wire output voltage at $Re_c = 0.47 \times 10^5$ with excitation frequency of $f = 800$ Hz yielding a 4.5 Hz oscillation, after Zaman et al.[8]

Chapter 2

Experimental Methods

This chapter describes the experimental methods, equipment and facilities used in this investigation. It features a detailed description of the experimental setup, measurement systems, data acquisition practices, and data reduction techniques.

2.1 Aerodynamic Testing Environment

2.1.1 Wind Tunnel

The current experiment was performed in the Aerodynamics Research Laboratory located at the University of Illinois at Urbana-Champaign. An open-return type, subsonic, low turbulence wind tunnel was used, shown in Fig. 2.1, having a rectangular cross section with a height of 2.8 ft, width of 4 ft, and streamwise length of 8 ft. In order to accommodate for the growth of the boundary layer along the walls, the cross-sectional area of the test section was intentionally designed to expand linearly such that the width of the upstream end was 0.5 inches smaller than the width of the downstream end. Since boundary-layer displacement effects can act to reduce the effective cross-sectional area of the test section, this expansion in the streamwise direction allowed the freestream velocity to remain constant across the test section length. The flow in the test section

was preconditioned using a four-inch thick honeycomb flow straightener and four anti-turbulence screens located at the inlet of the tunnel such that the turbulence intensity remained below 0.1% at all operating speeds. The ratio between the inlet cross section to the cross section of the upstream end of the test section was 7.5:1.

A 125-horsepower AC motor, powered by an ABB ACS 800 Low Voltage AC Drive, was used to drive a five-bladed fan installed near the end of the tunnel diffuser. The maximum angular speed that the motor was limited to was approximately 1200 RPM, which corresponded to a maximum empty test section speed of approximately 165 mph (242 ft/sec). The Reynolds number of an airfoil model was calculated based on the chord using,

$$\mathrm{Re} = \frac{\rho U_\infty c}{\mu} \tag{2.1}$$

where U_∞ is the test-section freestream velocity, c is the airfoil chord, ρ is the air density, and μ is the dynamic viscosity of air. During all wind tunnel tests the chord-based Reynolds number was kept to within 0.5% of the desired value through an iterative computer routine.

The difference in static pressures (ΔP) between the inlet settling section and the test-section inlet ($P_{ss} - P_{ts}$) was used to implicitly determine the freestream velocity in the test-section. A Setra 239 15" WC differential pressure transducer was used to measure ΔP. The settling section pressure was averaged across four pressure taps located just downstream of the anti-turbulence screens, with one tap located on each tunnel wall, which was used as reference for the pressure transducer. Likewise, the test section pressure was averaged across four pressure taps located just upstream of the test section, with one tap located on each tunnel wall, which was connected to the sensing port of the differential pressure transducer. Knowing the difference in static pressure across the wind tunnel inlet, ΔP, and assuming a steady, inviscid, and incompressible flow through the tunnel, the velocity in the test section can be calculated using an expression of the constant volume flow rate (Eq. 2.2) across each section of the wind tunnel in combination with Bernoulli's equation (Eq. 2.3) applied at the settling section and the test section inlet. The velocity in the test section was then obtained through Eq. 2.4.

$$A_{ss} U_{ss} = A_{ts} U_{ts} \tag{2.2}$$

$$\frac{1}{2}\rho U_{ts}^2 + P_{ts} = \frac{1}{2}\rho U_{ss}^2 + P_{ss} \tag{2.3}$$

$$U_{ts} = \sqrt{\frac{2\left(P_{ss} - P_{ts}\right)}{\rho_{amb}\left(1 - \left(\frac{A_{ts}}{A_{ss}}\right)^2\right)}} \tag{2.4}$$

The term A_{ts}/A_{ss} in Eq. 2.4 represents the ratio between the cross-sectional areas of the test section and the tunnel inlet, and ρ_{amb} represents the ambient air density. The ideal gas law (Eq. 2.5) was used to calculate the air density,

$$\rho_{amb} = \frac{P_{amb}}{RT_{amb}} \tag{2.5}$$

where R is the specific ideal gas constant for air. The ambient pressure (P_{amb}) and the ambient temperature (T_{amb}) were measured using a Setra 270 absolute pressure transducer and a National Instruments Type-J thermocouple respectively.

2.1.2 Airfoil Model

The current study was performed using a single element NACA 0012 airfoil, presented in Fig. 2.2. It had an 18-inch chord and 33.5-inch span. The trailing edge was designed to have 0.125-inch finite thickness to allow for the installation of instrumentation at the x/c = 1.0 location. A potential flow based solver, XFOIL[26], was first used during the design phase to compute the airfoil performance coefficients. The airfoil geometry was defined by starting with the standard NACA 0012 geometry. XFOIL was then used to modify it in order to create the finite-thickness trailing edge. The trailing edge thickness was increased to 0.6944% of the chord and the airfoil contour was blended to accommodate for the trailing edge thickness. The blending distance was selected to be the full chord length of the airfoil. The resulting geometry was used to design the airfoil model and to calculate estimates of the airfoil performance coefficients and pressure distributions.

The model was installed vertically in the wind tunnel such that it spanned the height of the test section. A small gap of approximately 0.1 inches was left between the model and the tunnel floor in order to provide clearance for the model angle of attack to be rotated. Similarly, a small gap of approximately 0.1 inches was left between the model and the tunnel ceiling. A photograph of the NACA 0012 model installed in the test section is presented in Fig. 2.3. The airfoil was constructed in three different sections consisting of an upper section, a lower section, and a middle section. The middle section of the NACA 0012 model was constricted from a solid block of

aluminum using a wire EDM manufacturing process. This aluminum center section was built with a hollow core in order to house the instrumentation, such that the wall thickness of the aluminum airfoil section was 0.3 inches. The upper and the lower sections, which flanked the central aluminum part on either side, were made out of extruded polystyrene foam covered in polyester resin. The separate parts were put together and the resin was finished down to form the NACA 0012 shape. Aluminum airfoil-shaped endplates with a chord length of 18 inches were attached to each side of each foam core section. An additional 0.25-inch thick endplate was mounted on either outboard side of the model using three screws. A total of four threaded rods, having lengths equal to the airfoil model span, were used to hold the model sections together. Additionally, a hollow steel spar shaft with a 57.5-inch length, 0.75 inches inner diameter, and 1.25 inches outer diameter was located at the quarter chord of the airfoil model. This spar was designed to protrude on both sides of the model, such that it went through holes in the tunnel test section floor and ceiling. The shaft extended 6.75 inches from the top endplate of the airfoil and 15.8 inches from the bottom endplate.

The steel spar shaft was mounted inside of two ball bearings, one above the wind tunnel ceiling and one below the wind tunnel floor, in order to hold the model in place and transfer loads. The longer part of the shaft below the wind tunnel floor was attached to a shaft coupling, which was also attached to a large 2.75-inch diameter steel shaft. This shaft was rotated using a Kollmorgen brushless servo motor (described in greater detail in Section 2.3.1), which was used to regulate the airfoil model angle of attack. Two holes on the shaft, located at the spanwise position of the central aluminum section of the model, were used to route the instrumentation wires through the hollow body of the shaft. The shaft was securely attached to the model by using steel collar pieces. The collar pieces were pinned to the shaft, then inserted into a cutout in the outermost endplate, such that it was flush with it and fastened to the foam core endplate using two screws. A second hollow 33.5-inch shaft with 0.375-inch outer diameter was also installed at the $x/c = 0.66$ location, and was installed across the model spanwise length to add stiffness and assist in alignment of the airfoil segments. A CAD picture of the model which shows how the three sections fit together was shown in Fig. 2.4.

The model was fitted with 27 ultra-miniature high frequency response pressure transducers, model XCS-062-5D (seen in Fig. 2.5) manufactured by Kulite Semiconductor Products Incorporated, distributed over the upper and lower surfaces. All of the unsteady pressure

transducers were configured and calibrated by the manufacturer for a ±5 psi differential maximum pressure. The unsteady pressure transducers were manufactured with a cylindrical outer shell, having a length of 0.375-inches and a diameter of 0.066-inches. Each transducer was equipped with four lead wires and a reference tube, which allowed a pressure to be supplied to the reference side of the transducer. The lead wires were routed to the designated temperature compensation modules. The signal wires out of the temperature compensation modules were used to provide excitation and obtain voltage measurements from the pressure transducer.

These transducers were integrated in the middle of the central aluminum section and were used to acquire unsteady pressure measurements (described in greater detail in Section 2.4.1). Two of the Kulite transducers were located at the leading and the trailing edge at x/c = 0.000 and x/c = 1.000 respectively. Six of the transducers were located on the lower surface of the model at x/c = 0.650, 0.500, 0.350, 0.207, 0.100, and 0.040, with the remaining 19 integrated across the upper surface at x/c = 0.023, 0.033, 0.044, 0.056, 0.067, 0.094, 0.117, 0.150, 0.206, 0.300, 0.361, 0.422, 0.483, 0.544, 0.606, 0.667, 0.728, 0.789, and 0.850. Fig. 2.6 shows a diagram of the location of the Kulite pressure transducers across the airfoil surface. The reference pressure ports of each of these unsteady pressure transducers were connected to a separate polyurethane tube. All 27 polyurethane tubes were then connected to a pressure distribution manifold which was in turn connected to a single polyurethane tube such that the reference pressure supplied to all transducers would be the same. The common pressure tube was routed, together with the transducer wires, through the hollow steel shaft out the top of the wind tunnel test section. The reference pressure tube was connected to the test section static pressure (P_{ts}) of the tunnel, such that the readings provided by the pressure transducers were referenced to the free stream conditions.

2.2 Data Acquisition System

National Instruments Lab View software, run on Dell Precision T3400 computer with a Windows XP 32-bit system, was used to acquire the data for all the measurements. A graphical user interface was used to send commands and tasks to the tunnel variable frequency drive controller, and Zaber traverse system (used to run the wake traverse described in Section 2.4.2) via RS-232 communication. Two miniature electronic differential pressure measurement units, models ESP-32HD manufactured by Esterline, Inc. in combination with a Digital Temperature Compensation (DTC) Initium Data Acquisition System were used to take wake surveys.

A National Instruments Signal Conditioning eXtensions for Instrumentation (SCXI) measurement system and a National Instruments PCI-MIO-16XE-10 A/D board were used to acquire unsteady pressure measurements. The SCXI system consisted of two SCXI-1001 chassis, each configured with three groups of four modules. Each group of SCXI modules consisted of one SCXI-1140 Simultaneous-Sampling Differential Amplified module, one SCXI-1142 Low-pass Bessel Filter module, and two SCXI-1121 Isolation Amplifiers with Excitation modules. SCXI-1321 terminal blocks, which provided a simple platform to connect the signal and the excitation cables of the measurement instruments, were connected to each of the SCXI-1121 modules. Each of the six SCXI-1321 modules per SCXI-1001 chassis had four channels. All of the SCXI modules were integrated into the individual SCXI-1001 chassis. A photograph of the SCXI system is presented in Fig. 2.7.

The SCXI-1142 modules were configured to low-pass filter the analog voltages from the transducers at the Nyquist frequency in order to prevent aliasing. The filter specifications that were used were provided by the manufacturer. With use of the SCXI-1140 module, the signals from each of the 27 pressure transducers and the Dynapar hollow-shaft encoder (discussed in Section 2.3.2) to be sampled simultaneously. This sampling capability was realized by storing the voltages acquired at any instant of time in a series of capacitors. The voltages stored in the capacitors were then successively sampled by the A/D system. Although the acquired voltages at a given instance were not digitalized simultaneously, the voltages across all channels were stored in capacitors simultaneously, allowing for the digitized signals to be representative of the analog signals at that instance. In order to increase the signal to noise ratio and improve the digitization of the analog signal, a small gain was also applied to the measured voltages.

The SCXI modules were configured in groups of four which allowed for a total of eight channels to be sampled per module grouping. Since each of the two SCXI-1001 chassis allowed for three groups of modules, a total of 48 channels could be sampled simultaneously. The 27 Kulite pressure transducers and the Dynapar hollow-shaft encoder were connected to separate channels on the SCXI chassis. The first SCXI-1001 chassis was connected to both the PCI-MIO-16XE-10 A/D board and the second SCXI-1001 chassis. A representative schematic of the SCXI module configuration setup is presented in Fig. 2.8.

2.3 Model Attitude Measurement and Control

2.3.1 Kollmorgen Cartridge Brushless Servo Motor

The airfoil model angle of attack was regulated using a Kollmorgen Cartridge DDR series direct drive brushless servo motor with a peak torque of 233 ft-lb and maximum rotational speed of 350 RPM. The Kollmorgen Cartridge Brushless Servo Motor was installed vertically on a steel frame support structure, shown in Fig. 2.9, under the test section of the wind tunnel. A shaft coupling was used to connect the motor to the main spar of the vertically installed airfoil model. The motor featured an integrated, factory-aligned high resolution feedback device in a unique bearing-less, one-component design that coupled directly to the load, using the machine's own bearings to support the rotor. The servo motor was driven by an AKD servo drive and was close-loop controlled with an NI PCI-7354 motion controller. The PCI-7354 included eight, 16-bit A/D converters for onboard data acquisition, as well as a host of advanced motion trajectory and triggering features. The motor programming, configuration, drive management, position and motion control were all executed via the manufacturer-provided Kollmorgen WorkBench user interface software.

2.3.2 Hollow-shaft Encoder

In addition to the Kollmorgen software, the angle of attack was tracked through the use of a Dynapar hollow-shaft encoder, series HS35R (shown in Fig. 2.10). It featured a Wide Gap Phased Array sensor which increased the air gap over ten times compared to traditional mask-on sensor designs. This, in combination with a rugged design, resulted in high resistance to shocks (up to 400g) and vibrations (up to 20g), while also eliminating signal drift due to time and temperature. The encoder was designed to produce reliable data while operated in the temperature range from -40°C to 100°C. The incremental feedback-type encoder used optical technology to provide up to 5000 pulses per revolution which resulted in resolution of 0.072°/pulse. The resulting signal would be a square wave with rise and fall times of less than 1 microsecond.

The hollow shaft encoder was mechanically attached to the main spar of the airfoil model using a clamp down collar. In order to prevent the encoder from moving around the model shaft, the body of the encoder was connected to a tether (refer to Fig. 2.10) using three screws. Fixing the encoder position to a stationary object with the tether ensured that only the rotation of the shaft

was measured. After installation, the encoder output signal was connected to the data acquisitioning system, described in detail in Section 2.2, and the resulting model position data were acquired simultaneously with the unsteady pressure readings.

2.4 Airfoil Performance

2.4.1 Unsteady Pressure Measurements

The XCS-062 high frequency response pressure transducers, discussed in Section 2.1.2, were integrated in the airfoil surface in order to collect unsteady pressure measurements. The SCXI system provided 10V excitation to each transducer, which consisted of a diaphragm connected in a four arm Wheatstone bridge configuration with an output voltage linearly proportional to the applied pressure. A calibration slope and intercept for each transducer were determined by the manufacturer using a five-point calibration procedure at room temperature. Therefore, the differential pressure sensed by the transducer (ΔP_{trans}) could be calculated using,

$$\Delta P_{trans} = mV_{trans} + b \tag{2.6}$$

where m and b represent the calibration slope and the intercept of the calibration respectively, and V_{trans} represents the output voltage of the transducer. Changes in temperature caused slight changes in the zero-pressure voltages. Thus, all transducers were re-zeroed prior to every run while the wind tunnel fan was idle. Since all pressure measurements were zero-corrected by subtracting the zero-pressure voltages from the acquired voltages, Eq. 2.6 simplified to,

$$\Delta P_{trans} = mV_{0,trans} \tag{2.7}$$

where $V_{0,trans}$ was the transducer voltage after the correction was applied.

2.4.1.1 Unsteady Model Pressures and C_p Distributions

The Setra 239 pressure transducer was used for measuring ($P_{ss} - P_{ts}$), as outlined in Section 2.1.1. Therefore, the pressure measurements about the surface of the airfoil model were non-dimensionalized by the freestream dynamic pressure, based on the Setra 239 measurements, to obtain the model C_p distribution. The dynamic pressure of the freestream flow (q_∞) was calculated using,

$$q_\infty = \frac{1}{2}\rho_\infty U_\infty^2 \tag{2.8}$$

Using Eq. 2.4 for the test section freestream velocity, the above expression can be rewritten in terms of the tunnel contraction ratio as,

$$q_\infty = \frac{1}{2}\rho_\infty U_{ts}^2 = \frac{P_{ss} - P_{ts}}{1 - \left(\frac{A_{ts}}{A_{ss}}\right)^2} \tag{2.9}$$

where ρ_∞ represents the density of freestream air, which is assumed to be equal to the ambient density (ρ_{amb}) used in Eq. 2.4. This followed from the assumption of incompressible flow through the wind tunnel ($M_\infty \leq 0.3$). The freestream dynamic pressure (q_∞) was assumed to be constant between the inlet of the test section, where the test section static pressure (P_{ts}) was measured, and the near upstream region of the airfoil model. Since the total pressure was assumed to be constant, the static pressure at the inlet of the test section could be assumed to be equal to the static pressure by the airfoil.

The sensing sides of the Kulite unsteady pressure transducers were installed flush with the airfoil surface. Since all transducers were connected to a common test-section static reference pressure, they measured the difference between the instantaneous local airfoil surface pressure and the test section static pressure ($P_{s,i} - P_{ts}$). As a result, the instantaneous pressure coefficient ($C_{p,i}$) of a given location on the airfoil could be calculated by dividing the measured differential pressure ($P_{s,i} - P_{ts}$) by the dynamic pressure (q_∞), Eq 2.9.

$$C_{p,i} = \frac{P_{s,i} - P_{ts}}{q_\infty} \tag{2.10}$$

The mean pressure coefficient ($\overline{C_p}$) was determined from the measured unsteady pressures by taking a time average using,

$$\overline{C_p} = \frac{1}{N}\sum_{i=1}^{N} C_{p,i} \tag{2.11}$$

where N represents the number of instantaneous pressure samples acquired.

An estimate of the unsteadiness in the pressure signal was obtained by calculating the standard deviation ($C_{p,SD}$) of the unsteady C_p, using,

$$C_{p,SD} = \sqrt{\frac{1}{N}\sum_{i=1}^{N}\left(C_{p,i} - \overline{C_p}\right)^2} \qquad (2.12)$$

2.4.1.2 Airfoil Performance Coefficients from Surface Pressure Measurements

The mean pressure distribution measurements about the airfoil surface were used to determine the airfoil lift and pitching moment coefficients. The airfoil contour was approximated by a series of line segments, each constructed by drawing a line between any two adjacent pressure transducers. A total of (*n-1*) panels for (*n*) pressure taps were generated. The pressure across each of these linear sections was assumed to be the average of the two pressures measured by the pressure taps at each end of the linear segment. The resulting force due to the pressure on each segment acted in a direction normal to the surface of that segment. Therefore, knowing the segment orientation with respect to the chord line, the force was split into chord-normal and chord-axial components. The chord-normal force and chord-axial force across each linear segment ($\Delta F_N'$ and $\Delta F_A'$) were calculated using,

$$\Delta F_N' = \frac{P_i + P_{i+1}}{2}\left(x_{i+1} - x_i\right) \qquad (2.13)$$

$$\Delta F_A' = -\frac{P_i + P_{i+1}}{2}\left(y_{i+1} - y_i\right) \qquad (2.14)$$

The airfoil net axial and net normal forces were determined by summing the individual linear segment contributions. The airfoil chord-normal sectional force and the chord-axial sectional force were calculated using,

$$F_N' = \sum_{i=1}^{n-1}\Delta F_N' \qquad (2.15)$$

$$F_A' = \sum_{i=1}^{n-1}\Delta F_A' \qquad (2.16)$$

where *n* is the number of chordwise pressure taps on the airfoil model. Knowing the angle of attack, the airfoil sectional force was then calculated from the normal and axial sectional forces using,

$$L' = F_N' \cos\alpha - F_A' \sin\alpha \tag{2.17}$$

Similarly, the chord-normal and the chord-axial sectional forces across a given linear segment were used to calculate the sectional quarter-chord pitching moment using,

$$\Delta M'_{c/4_i} = \Delta F_N' \left(x_{c/4} - \frac{x_i + x_{i+1}}{2} \right) + \Delta F_A' \left(\frac{y_i + y_{i+1}}{2} \right) \tag{2.18}$$

The net airfoil sectional quarter-chord pitching moment was calculated by summing the contributions of all linear segments using,

$$M'_{c/4} = \sum_{i=1}^{n-1} \Delta M'_{c/4_i} \tag{2.19}$$

The sectional lift force and quarter-chord pitching moment were non-dimensionalized, using Eq. 2.20 and Eq. 2.21 respectively, to obtain the airfoil lift coefficient (C_l) and quarter-chord pitching moment coefficient (C_m).

$$C_l = \frac{L'}{q_\infty c} \tag{2.20}$$

$$C_m = \frac{M'_{c/4}}{q_\infty c^2} \tag{2.21}$$

2.4.2 Drag Calculation from Wake Pressures

While the surface pressure measurements could be used to provide pressure drag information for the airfoil, this only provided a contribution to the total airfoil drag. Therefore, a wake survey system was used to calculate the airfoil drag, using a momentum-based approach. The wake survey system consisted of a traversable wake rake and a two-axis traverse system. A total of 59 total pressure probes, each having an outer diameter of 0.04-inches, were aligned horizontally along the rake. The wake rake was suspended from the ceiling of the test section using a support structure as shown in Fig. 2.11 in order to acquire the total pressure profile of the airfoil

wake downstream of the vertically-oriented airfoil. A two-axis traverse mechanism, controlled precisely by a pair of stepper motors, was used to traverse the rake in the vertical (spanwise) and horizontal (chord normal) directions. The wake rake was traversed across a plane approximately 1.2 chord lengths downstream of the trailing edge of the airfoil model in the horizontal (chord-normal) direction until the tails of the wake profile were sufficiently captured. This process was automated through a LabView computer routine that determined the position of the wake tails by comparing the gradient of the total pressure deficit at multiple locations along the span of the wake profile.

The total pressure probes in the wake rake were connected to two ±0.35 psid (±10.0 in. WC) ESP scanners. The ESP scanners consisted of an array of silicon piezo-resistive sensors that were connected in a Wheatstone bridge configuration and generated a voltage proportional to the pressure input. Each of these scanners had 32 ports that could be connected through a pressure tube to a total pressure probe on the wake rake. All of the total pressure measurements acquired with the wake rake were zero-referenced against the ambient pressure inside the testing facility. A Digital Temperature Compensation (DTC) Initium Data Acquisition System was used to acquire the output voltages from the scanners.

The standard momentum deficit method described by Jones and Schlichting was used to calculate the drag of the airfoil. The method involves a control volume analysis around the body, assumes steady, two-dimensional flow and uniform freestream. The outflow plane of the control surface is placed sufficiently far downstream from the airfoil where the static pressure in the wake (P_w) is equal to the freestream static pressure (P_∞). Due to viscous effects however, the total pressure in the wake is expected to be lower than the freestream total pressure and this pressure loss can be attributed to the wake velocity deficit. Using the equation of conservation of momentum in the integral form, the drag at a given spanwise section of the airfoil model can be calculated using,

$$D' = \rho \int u_w (U_\infty - u_w) dy \tag{2.22}$$

Since the flow is incompressible (i.e. $M_\infty \leq 0.3$), the total pressure across the freestream plane and the *w*-plane can be expressed using Eq. 2.23 and Eq. 2.24 respectively.

$$P_\infty + \frac{1}{2}\rho U_\infty^2 = P_{0,\infty} \tag{2.23}$$

$$P_w = P_\infty + \frac{1}{2}\rho u_w^2 = P_{0,w} \tag{2.24}$$

The velocity terms in Eq. 2.23 and Eq. 2.24 are expressed in terms of static and total pressures. The resulting expressions are substituted into Eq. 2.22 to yield,

$$D' = 2\int \sqrt{P_{0,w} - P_\infty}\left(\sqrt{P_{0,\infty} - P_\infty} - \sqrt{P_{0,w} - P_\infty}\right)dy \tag{2.25}$$

Equations 2.23 and 2.24 can be combined to express the dynamic pressure at the wake plane in terms of the wake total pressure, freestream total pressure and the freestream dynamic pressure:

$$q_w = q_\infty - \left(P_{0,\infty} - P_{0,w}\right) \tag{2.26}$$

An expression for the sectional drag of the airfoil in terms of the wake total pressure deficit can be obtained using Eq. 2.25 and Eq. 2.26,

$$D' = 2\int \sqrt{q_\infty - (P_{0,\infty} - P_{0,w})}\left(\sqrt{q_\infty} - \sqrt{q_\infty - (P_{0,\infty} - P_{0,w})}\right)dy \tag{2.27}$$

The expression in Eq. 2.27 allows an accurate estimate of the sectional drag to be obtained in the wake surveys by directly measuring the difference between the freestream total pressure and the wake total pressure. This method was used since it did not require the freestream total pressure to be directly measured. The ESP scanners used for acquiring the wake pressures were referenced to a stable atmospheric pressure reference in the control room in order to achieve greater repeatability of the drag measurements. As a result, instead of directly measuring ($P_{0,\infty} - P_{0,w}$), it was calculated by,

$$P_{0,\infty} - P_{0,w} = \left(P_{0,\infty} - P_{atm}\right) - \left(P_{0,w} - P_{atm}\right) \tag{2.28}$$

where the gauge pressure measurements of the wake total pressure, ($P_{0,w} - P_{atm}$), were obtained in the wake of the airfoil and the gauge pressure measurements of the freestream total pressure, ($P_{0,\infty} - P_{atm}$), were obtained outside the wake of the airfoil.

Substituting the pressure difference ($P_{0,\infty} - P_{0,w}$) given by Eq. 2.28, along with q_∞, in Eq. 2.27 yielded an expression for the sectional drag of the airfoil. A numerical integration using the trapezoid method was used to solve Eq. 2.27. Thus, the sectional drag of the airfoil could be calculated using,

$$D' = \sum_{i=1}^{n_{rake}-1} \left[\sqrt{q_\infty - (P_{0,\infty} - P_{0,w_i})} \left(\sqrt{q_\infty} - \sqrt{q_\infty - (P_{0,\infty} - P_{0,w_i})} \right) + \sqrt{q_\infty - (P_{0,\infty} - P_{0,w_{i+1}})} \left(\sqrt{q_\infty} - \sqrt{q_\infty - (P_{0,\infty} - P_{0,w_{i+1}})} \right) \right] (y_i - y_{i+1}) \tag{2.29}$$

where n_{rake} represents the total number of probes that were used to measure the wake. As a result of spanwise variations of the flow due to imperfections in the model, the sectional drag of the airfoil was averaged over multiple spanwise stations to provide a spanwise invariant estimate of the sectional drag that would be characteristic of a true airfoil model of infinite span. The drag coefficient of the airfoil model was calculated from the sectional drag using,

$$C_d = \frac{D'}{q_\infty c} \tag{2.30}$$

2.5 Flow Diagnostics Methods

2.5.1 Power Spectral Density

Power spectral densities (PSD) were computed for the acquired unsteady pressure measurements in order to characterize the frequency spectrum associated with unsteady flow field oscillations. The PSDs were computed using standard fast Fourier transform (FFT) methods, which were RMS averaged to obtain a set of ensemble-averaged spectra. This averaging process was performed to highlight the recurring trends in the spectral content and reduce the influence of random fluctuations in the signal. The PSDs in the current study were calculated using the data points acquired over 19 identical runs of 30,000 samples each. Each of the runs could be split into multiple ensembles to increase the number of realizations in the ensemble, which also decreased the frequency resolution of the resulting PSD. In the current study, each time history was split into 5 realizations, and these realizations were combined across all runs to perform the ensemble average. The resulting PSD were then premultiplied by the corresponding frequency to ensure equal power weighting of each Fourier mode. Using the dominant frequencies (f) obtained from

the premultiplied spectra, a Strouhal number (St) was calculated, using the projected height of the airfoil ($c\sin\alpha$) as the characteristic length scale:

$$St = \frac{f(c\sin\alpha)}{U_\infty} \tag{2.31}$$

2.5.2 Time-resolved Particle Image Velocimetry

As a non-intrusive experimental technique, Particle Image Velocimetry (PIV) is often used to determine the instantaneous velocity fields of flows. The flow is seeded with small tracer particles whose velocity is measured to accurately track the motion of the fluid. A high-intensity coherent source of light, such as a laser, is then used to illuminate the particles. Successive image pairs of the particles are recorded at precisely-defined time intervals to determine the displacement of the particles across small regions of the field of view. The velocity fields are obtained by using the known time interval and the resulting pixel displacements. Since the data acquisition frequency is low in comparison to the frequencies observed in typical flows and it is often times not possible to phase-lock to a desired frequency, a regular 2D PIV technique cannot be used to reconstruct the temporal evolution of flow structures. Thus, in order to be able to identify the unsteady flow phenomena that are present in the current study and contribute to the hysteretic behavior, a time resolved particle image velocimetry (TR-PIV) technique was used.

In the current study, planar PIV data were acquired across a horizontal image plane centered at the mid-span of the airfoil just under the location of the Kulite pressure transducers. The field of view spanned from the region immediately upstream of the leading edge of the airfoil to x/c = 0.53, as shown in Fig. 2.12. PIV data were acquired at angles of attack of α = 13°, 14°, 15°, and 16°, where hysteresis effects were predominantly identified. A dual-pulsed 60W Quantronix Darwin Duo Nd: YLF laser was used to provide two consecutive laser pulses at a wavelength of 527 nm. The laser was operated in external double-trigger mode to produce a pair of laser pulses, separated by Δt = 60μs, at a dual-pulse repetition rate of 1.5 kHz. The resulting particle displacements in the images were on average 10 pixels. A combination of converging and diverging lenses was used to form a laser sheet expanding in the horizontal direction with a constant thickness of approximately 1 mm. Fig. 2.13 shows a representation of the PIV setup with the airfoil model installed in the wind tunnel test section.

Surface reflections off the airfoil were mitigated with the use of a matte black light adhesive paper which was affixed to the airfoil surface. Furthermore, while acquiring data, the laser was situated upstream of the airfoil model (as seen in Fig. 2.13) such that the laser sheet impinged on the surface of the airfoil at a large angle. This configuration allowed the laser to nearly graze the surface of the model, with the majority of the light scattering reflected in the downstream direction. Thus, the glow due to the light reflected from the airfoil model was significantly decreased, as compared to a direct impingement of the laser sheet.

A mineral oil based haze generator was used to seed the flow. The haze generator was capable of producing smoke particles that whose size was on the order of 10 μm in and was carefully operated to maintain a uniform seeding density inside the test section of the wind tunnel. A Photron Mini AX200 CMOS high-speed camera with 1024 × 1024 pixel resolution was used to acquire images of the seed particles at rate of 3000 fps. The high frame acquisition rate allowed for tracking the temporal and spatial evolution of flow structures from one frame to the other. The camera was equipped with a photographic lens with a focal length of f = 35 mm and was set at an f-number of 3.5 The camera manufacturer software was used to interface the camera with a computer in order to acquire images of the seeded flow.

The laser-camera system operated in a frame-straddling mode in order to acquire velocity field data at a frequency of 1.5 kHz. A BNC Model 625A digital-delay generator was used to synchronize the laser and the camera. LaVision DaVis version 8.3 was used to calculate the vector fields. A multipass method was used, with an initial interrogation window size of 128 × 128 pixels and 50% overlap, which was decreased to a 16 × 16 interrogation window at 50% overlap in the final processing steps. A set of numerical post-processing filters was also utilized to eliminate erroneous vectors in the instantaneous velocity fields.

2.6 Wind Tunnel Corrections

Since the wind tunnel testing environment is constrained with finite wall boundaries which introduces local wall effects that are not present in an unbounded freestream environment, wind tunnel corrections were made. The acquired data were corrected using the procedure outlined in the work of Barlow et al.[27] for 2D, low-Reynolds number wind tunnel testing. The applied corrections intended to compensate for solid blockage, wake blockage, and streamline curvature. It is worth noting that this correction procedure assumed an incompressible flow. The following

procedure would not be valid in a compressible environment, unless changes in air density were properly accounted for.

The presence of an airfoil model effectively reduces the cross-sectional area of the test-section and thus causes solid blockage effects. This reduction leads to, via continuity, in a local flow acceleration around the airfoil that are functions of model thickness and angle of attack. A solid-blockage velocity increment factor, ε_{sb}, defined by,

$$\varepsilon_{sb} = \frac{K_1 V_m}{C^{3/2}} \tag{2.32}$$

is used to correct for these velocity increases. In the above equation, K_1 is a constant parameter based on the airfoil configuration (K_1 = 0.52 for airfoil models spanning the height of the test-section), C is the empty test-section area, and V_m is the volume of the airfoil model. In the current study, the exact value of the airfoil model volume was obtained from CAD model, however, if such data is not available the model volume can be estimated using,

$$V_m = \frac{3}{4} tcb \tag{2.33}$$

where t and b are the dimensional thickness and span of the airfoil model.

Similar to the solid blockage effects, the wake blockage effects result in regions of local high velocities. In this instance, the velocity deficit associated with the wake of an airfoil results in an increase in velocity outside of the wake to ensure a constant mass flux across any given cross-section of the wind tunnel. Since the extent of velocity deficit in the wake is directly related to the profile drag of the airfoil, it can be empirically correlated to the profile drag. Thus, a wake blockage velocity increment factor, ε_{wb}, can be calculated using,

$$\varepsilon_{wb} = \frac{1}{2}\frac{c}{h} C_{d,u} \tag{2.34}$$

which can be used to determine the influence of the wake blockage effect. In the above equation, h is the height of the test-section and $C_{d,u}$ is the uncorrected value of the airfoil drag coefficient obtained through wake survey methods as described in Section 2.4.2. The solid blockage correction factor and the wake blockage correction factor are added together (Eq. 2.35) to establish the net velocity increment, ε.

$$\varepsilon = \varepsilon_{sb} + \varepsilon_{wb} \tag{2.35}$$

Streamline curvature effects, which would otherwise be absent in an unbounded flow field, are introduced by the solid walls of the test section. The wind tunnel walls artificially impose an apparent camber of the airfoil, as streamlines cannot penetrate these solid boundaries. Therefore, the lift and the magnitude of the quarter-chord pitching moment are incrementally changed in comparison with the lift and moment values that would be obtained in an unbounded environment. An empirically derived variable σ, can be used to compensate for the streamline curvature effect. It is calculated using,

$$\sigma = \frac{\pi^2}{48}\left(\frac{c}{h}\right)^2 \tag{2.36}$$

A set of empirically derived relations were used to calculate the correction factors in Eq. 2.32, 2.34, 2.36. The corrected airfoil angle of attack, lift coefficient, drag coefficient, quarter-chord pitching moment coefficient, and pressure coefficient, were corrected using Eqs. 2.37-2.41.

$$\alpha_{cor} = \alpha_u + \frac{57.3\sigma}{2\pi}\left(C_{l,u} + 4C_{m,u}\right) \tag{2.37}$$

$$C_{l,cor} = C_{l,u}\left(1 - \sigma - 2\varepsilon\right) \tag{2.38}$$

$$C_{d,cor} = C_{d,u}\left(1 - 3\varepsilon_{sb} - 2\varepsilon_{wb}\right) \tag{2.39}$$

$$C_{m,cor} = C_{m,u}\left(1 - 2\varepsilon\right) + \frac{1}{4}\sigma C_{l,u} \tag{2.40}$$

$$C_{p,cor} = \frac{C_{p,u}}{\left(1 + \varepsilon\right)^2} \tag{2.41}$$

2.7 Chapter 2 Figures

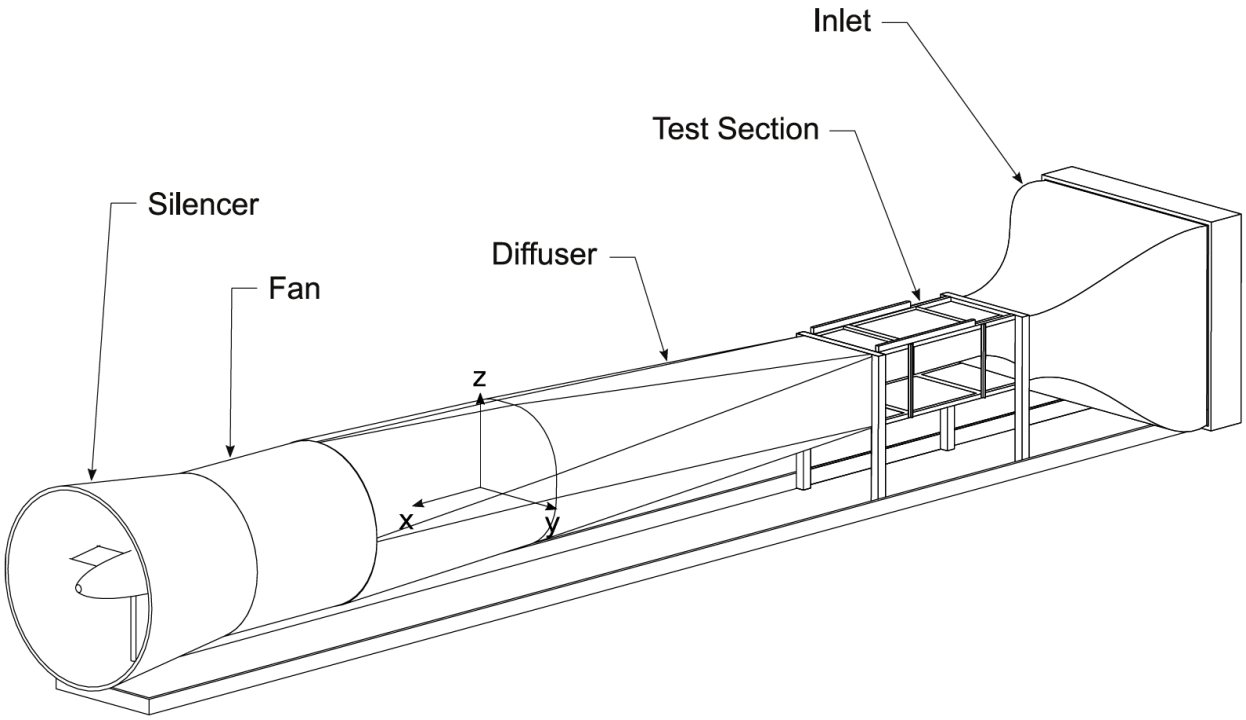

Fig. 2.1 Schematic of the University of Illinois 3-ft × 4-ft subsonic wind tunnel.

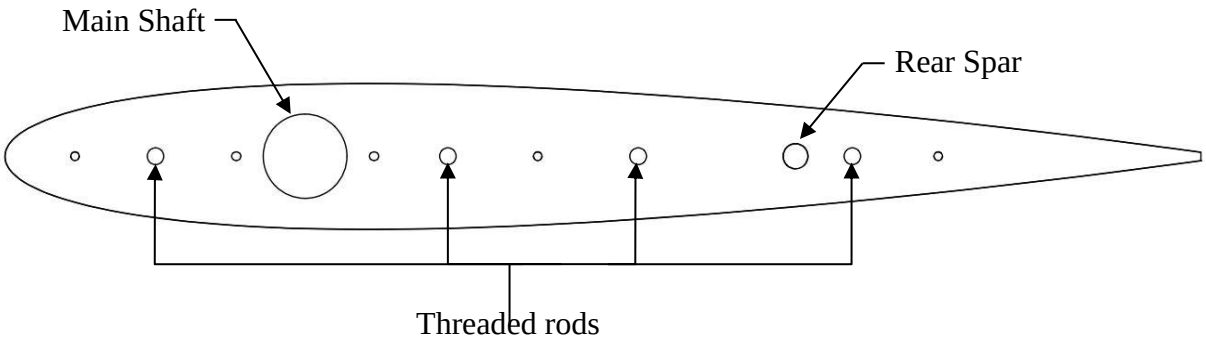

Fig. 2.2 NACA 0012 geometry indicating the relative positions of various spar elements.

Fig. 2.3 NACA 0012 airfoil model installed in the wind tunnel test section.

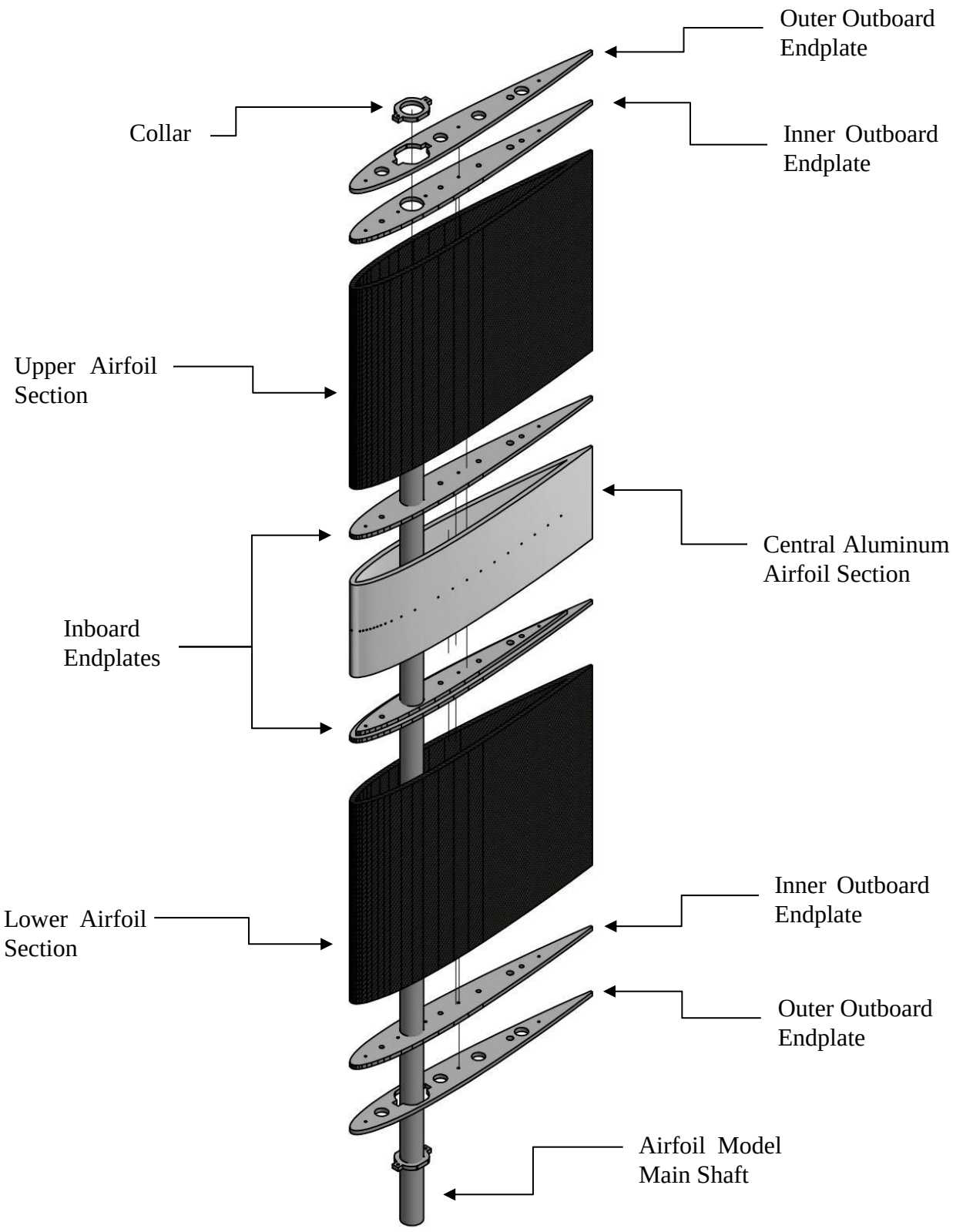

Fig. 2.4 Exploded view of the NACA 0012 airfoil model.

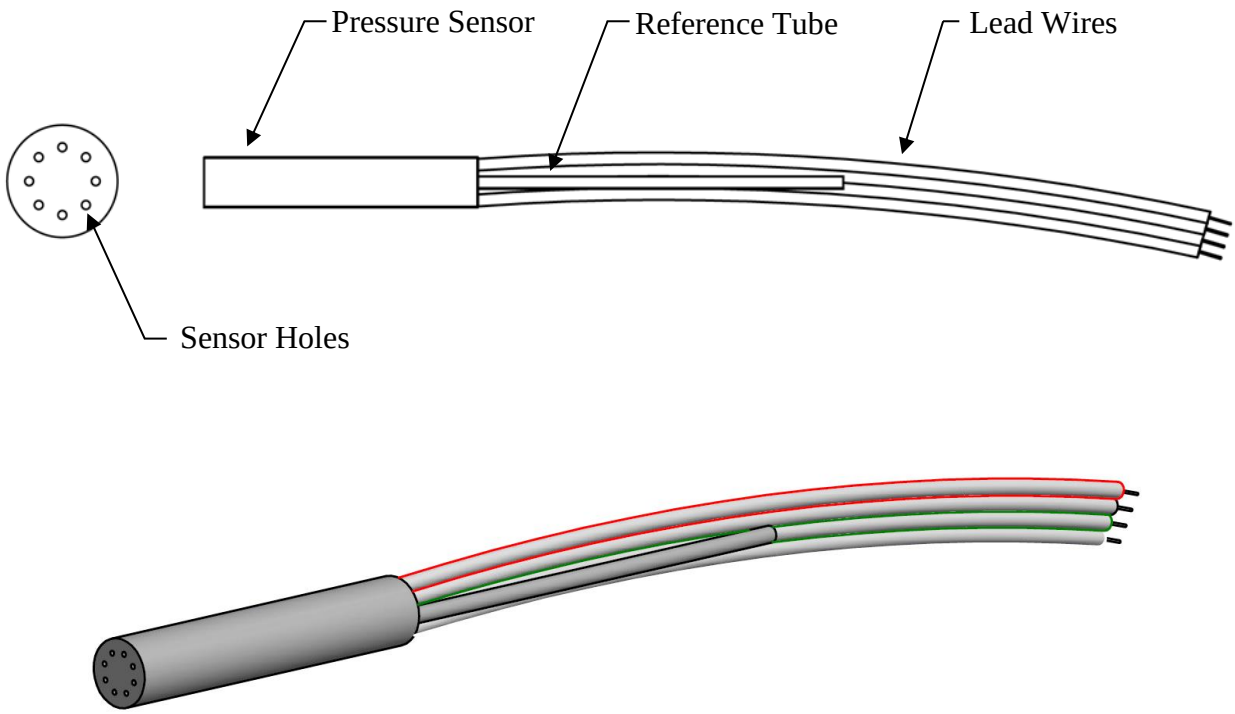

Fig. 2.5 Schematic of the Kulite XCS-062-5D high-frequency response pressure transducer, after Gupta.[28]

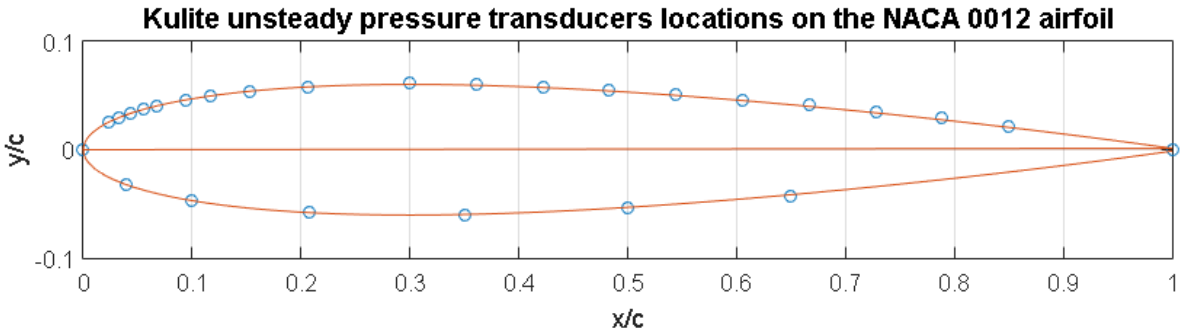

Fig. 2.6 Diagram of the unsteady pressure transducers locations on the airfoil.

Fig. 2.7 SCXI-1001 chassis and associated modules, after Ansell.[29]

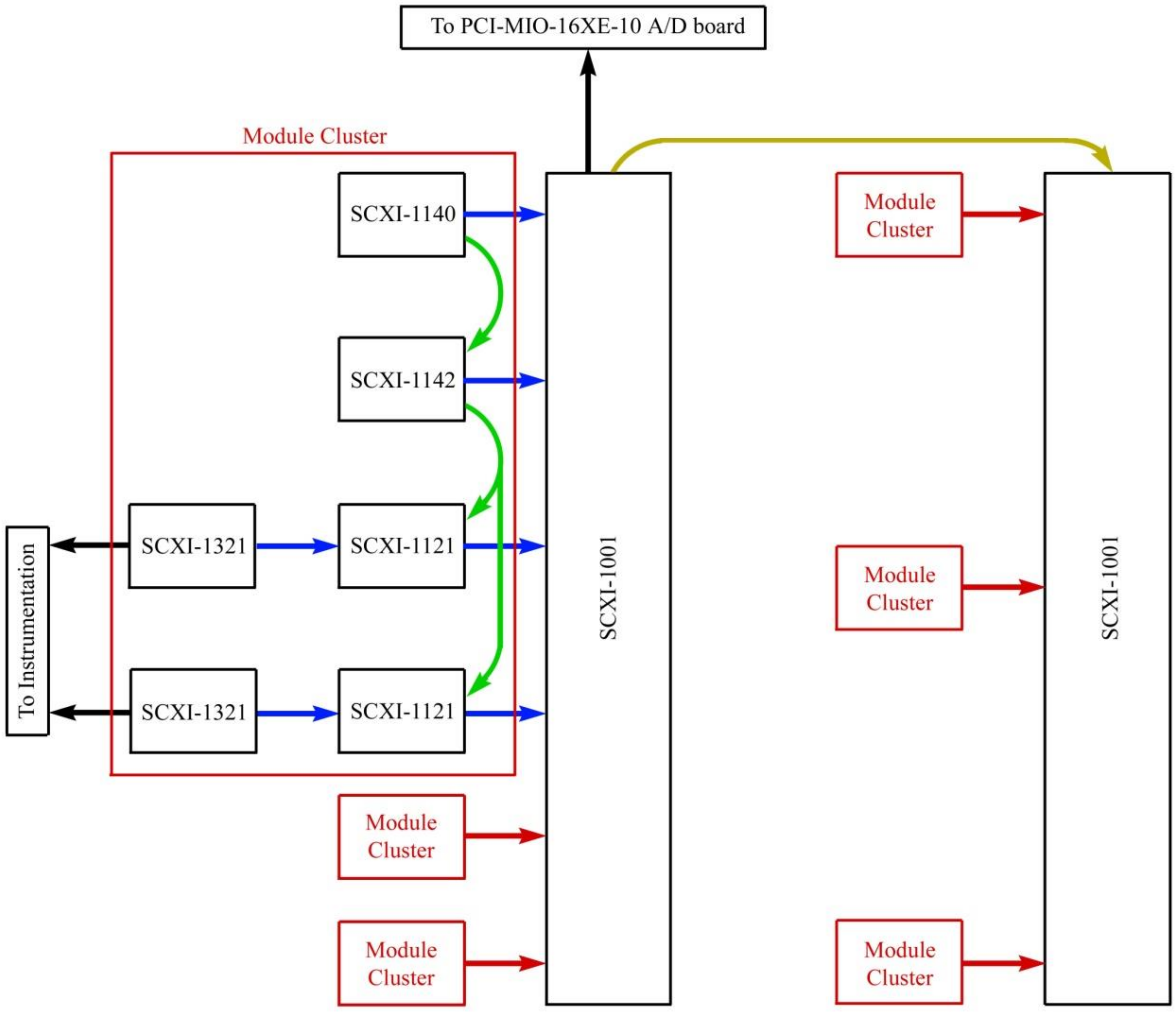

Fig. 2.8 Schematic of the SCXI module and chassis connection, after Ansell.[29]

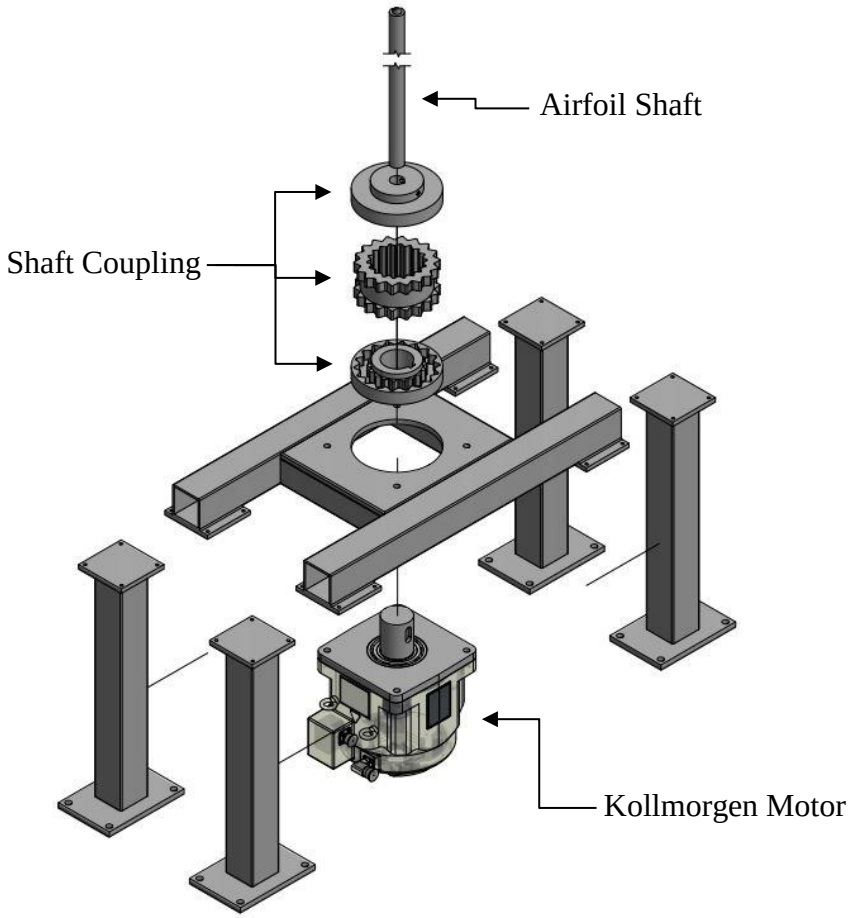

Fig. 2.9 Motor Assembly.

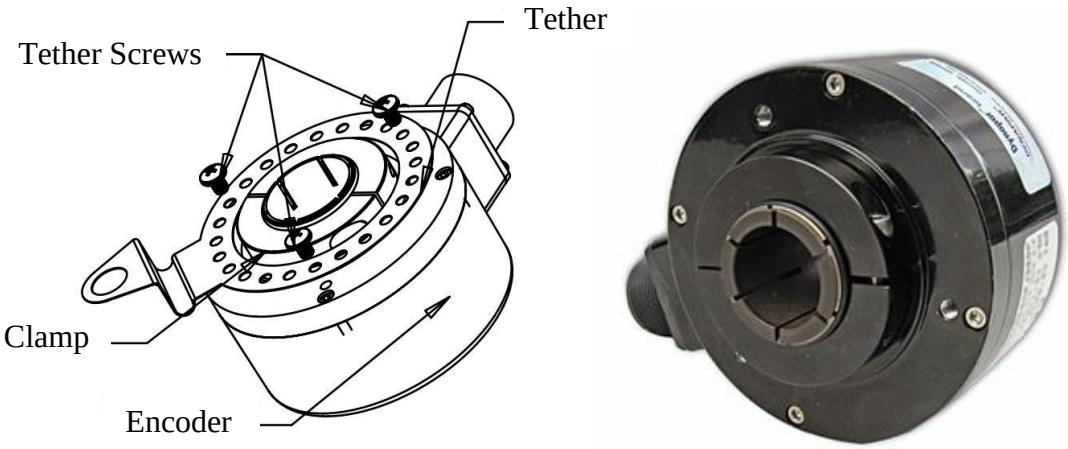

Fig. 2.10 Dynapar HS35R hollow-shaft encoder (images from manufacturer).[30]

Fig. 2.11 Wake rake installed downstream of the test section of the University of Illinois 3-ft × 4-ft subsonic wind tunnel.

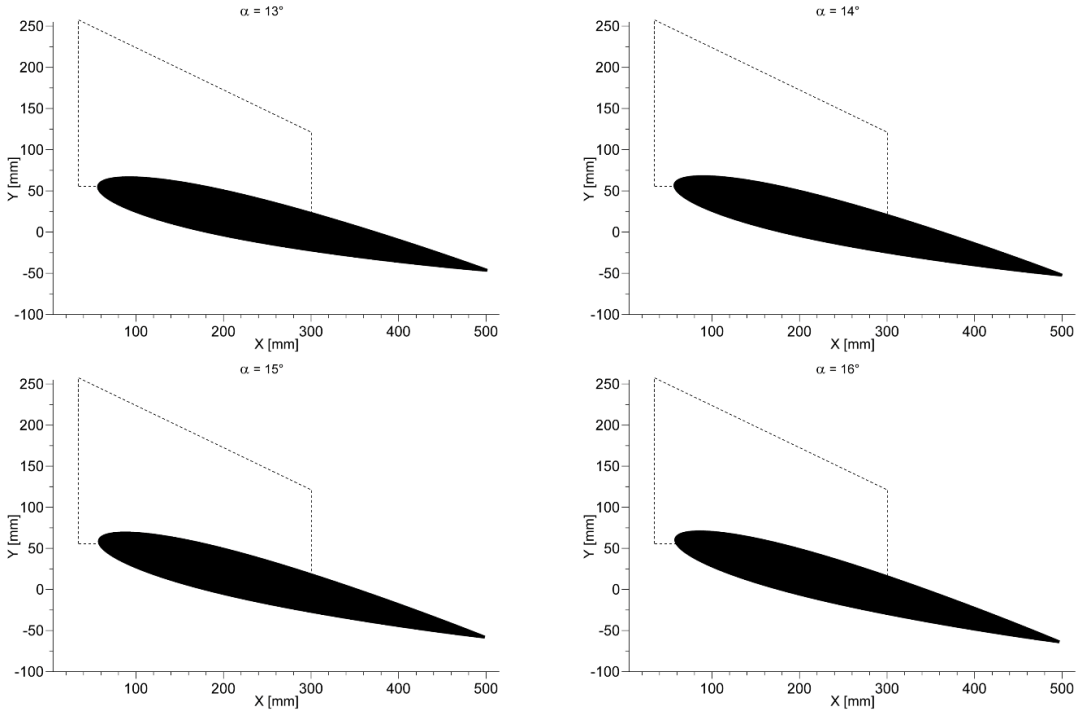

Fig. 2.12 Interrogation region for PIV measurements (to scale) at α = 13°, 14°, 15°, 16°.

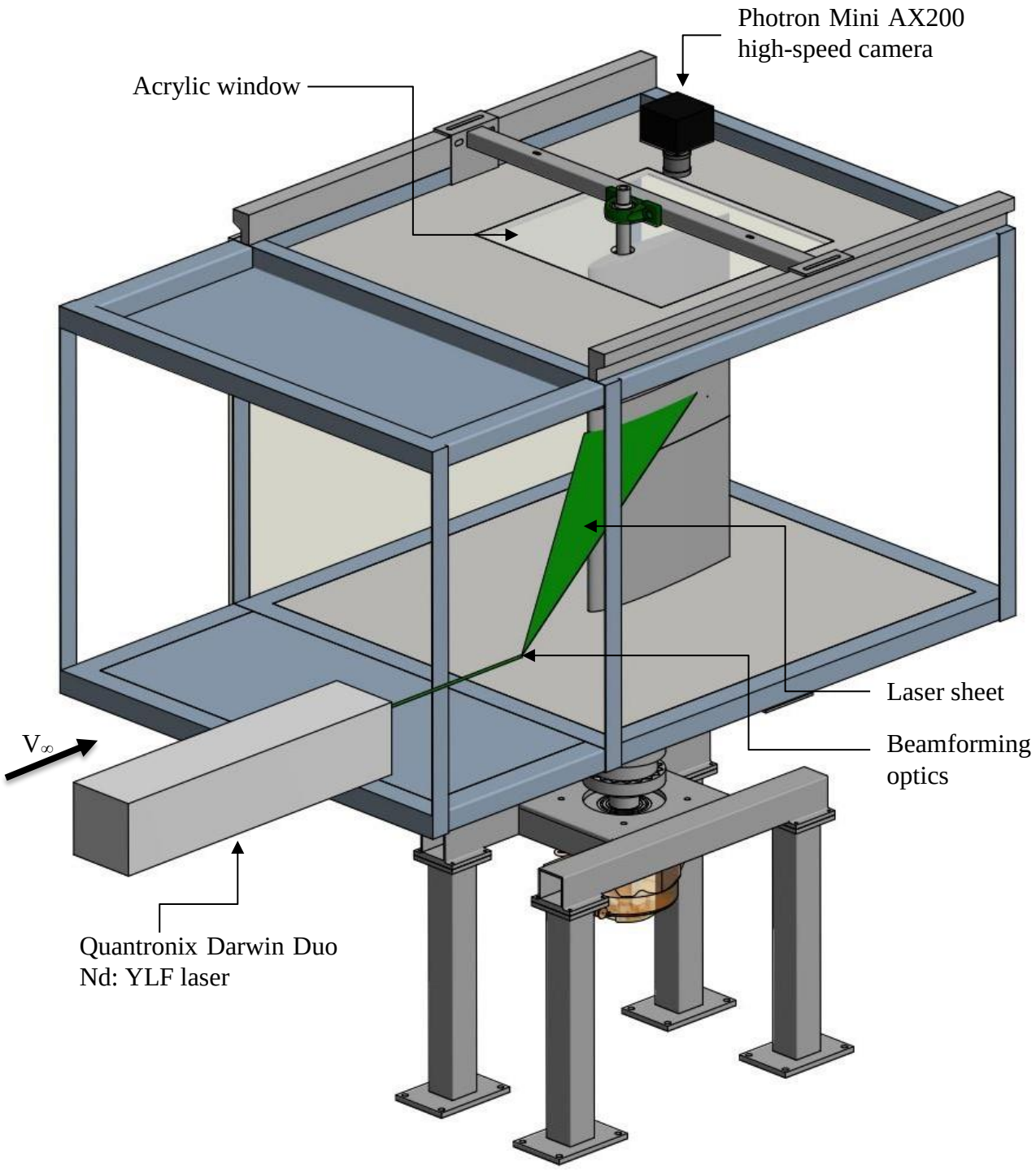

Fig. 2.13 PIV laser and camera system setup.

Chapter 3

Results and Discussion

This chapter describes the experimental results from this investigation. It includes a detailed analysis and discussion of these results. Findings resulting from the unsteady pressure measurements and the time resolved particle image velocimetry are presented in this chapter. The experimental results from the different investigation techniques were compared and conclusions were drawn in an attempt to improve the understanding of the unsteady flow effects and their relation to post-stall hysteresis.

3.1 Experimental Validation of NACA 0012 Airfoil

The NACA 0012 airfoil model performance was first validated by comparison to prior studies. Since no experimental data was available for Reynolds number of 1×10^6, comparisons were made to measurements found in literature at similar Reynolds numbers. Results from this study, after the wind tunnel corrections discussed in Section 2.6 were applied, were compared to results reported by Gurbacki[31], Ladson[32], Sheldahl and Klimas[33], and results obtained from in XFOIL[26].

The XFOIL-calculated C_l, as seen in Fig. 3.1, is in agreement with the experimental data at low angles of attack. However, with increasing angle of attack, especially around stall, the

discrepancies between the XFOIL-predicted airfoil performance coefficients and the experimental measurements increase. The difference between the predictions and the experiments are attributed to the reduced fidelity of the XFOIL modeling approach at higher angles of attack approaching stall. The C_m experimental data is in agreement with the XFOIL model in the angle of attack range of $\alpha = 6°$ to $\alpha = 14°$. Furthermore, the C_d vs. C_l polar was also qualitatively consistent with the XFOIL-calculated results. Additional validation of the airfoil used in the current study can be conducted by comparing the obtained pressure distribution results to those computed by XFOIL. Fig. 3.2 shows an example of the comparison of the C_p distribution determined in the current study at $\alpha = 10°$ to those predicted by XFOIL. The measured C_p distributions were qualitatively and quantitatively consistent with the computation. The magnitudes of the pressures calculated by XFOIL are slightly lower than the experimental data, however, besides this difference, the C_p distribution across the chord is fairly consistent with the experiment.

The experimental measurements for the NACA 0012 airfoil model were also validated by comparison with the results from experiments carried out by Sheldahl and Klimas[33] at Sandia National Laboratories in 1981 (Fig. 3.1). The results from the present investigation ($Re_c = 1\times10^6$) show very good agreement with those reported in the Sandia document ($Re_c = 0.86\times10^6$) for the NACA 0012 airfoil. Quantitative differences observed between the two sets of measurements are due to the slightly different Reynolds number used. It can be expected that as the Reynolds number increases, the stall angle of attack and the $C_{l,max}$ will also increase. Therefore, the comparison shows a standard lift curve behavior of the NACA 0012 model used in the current study. It is worth noting that the results for C_m, although slightly lower, are mostly consistent with the experimental data used for validation. The inconsistencies are explained by the lower density of pressure transducers on the airfoil model used for the current study. However, this was not considered a problem since the inconsistencies were minor, and the C_m data was not used to draw conclusions and interpret the results from the study.

The data from this experiment also exhibit similar trends with the performance determined by Gurbacki[31] who conducted tests at $Re_c = 1.8\times10^6$ in the same facility as the current study. These results were confirmed by comparison with Ladson[32] ($Re_c = 2\times10^6$). The stall angle of attack and the $C_{l,max}$ are higher in the results reported in those studies than they are for the current investigation. The C_d of the current study was also found to be higher than the validation data.

Similar to the study by Sheldahl and Klimas, these discrepancies can be explained by the difference in Reynolds number between the compared studies which is consistent with the expectations.

3.2 Time-Averaged Airfoil Performance

3.2.1 Time-Averaged Performance Coefficients

Steady surface pressure measurements around the NACA 0012 airfoil model were acquired at a chord-based Reynolds number of $Re_c = 1.0 \times 10^6$ ($M_\infty = 0.1$). Corrected data was reported for all performance results unless otherwise noted. A combined leading-edge and trailing-edge type stall behavior was observed from the characteristics of the lift coefficient (C_l) and the airfoil quarter-chord pitching moment coefficient (C_m) polars (Fig. 3.1). The C_l vs. α curve remained mostly linear until the near stall region with a semi-rounded lift-curve peak and a relatively sharp decrease in C_l. A maximum lift coefficient of $C_{l,max} = 1.16$ was recorded at $\alpha = 13.75°$ Therefore, $\alpha = 13.75°$ was defined as the stall angle of attack. The lift-curve exhibited a slight decrease at $\alpha = 14.5°$ and a steep drop at $\alpha = 15°$. Similarly, the C_m vs. α curve reached a maximum value at $\alpha = 13.75°$, and showed a sharp decrease at $\alpha = 15°$. The decreased pressure over the airfoil trailing edge leads to a strong negative contribution to C_m. The high sensitivity to initial conditions at $\alpha = 14.5°$ in combination with the sharp drop in C_l and C_m that followed at $\alpha = 15°$ justified the classification as a combined leading-edge and trailing-edge type.

Hysteresis loops were identified in the airfoil lift coefficient (C_l), quarter-chord pitching moment coefficient (C_m) and drag coefficient (C_d) polars during static stall. This hysteretic behavior was not expected to be present at the test Reynolds number as hysteresis loops are typically observed in the stall behavior of various airfoils at Reynolds numbers an order of magnitude lower than that used in the current study. Fig. 3.3 displays corrected data for the airfoil C_l, C_m, and C_d for commanded angle-of-attack range from $\alpha = -1°$ to $\alpha = 20°$ during an upstroke (increasing α) and across an angle-of-attack range from $\alpha = 20°$ to $\alpha = 11°$ during a downstroke (decreasing α). These results were acquired in a continuous run by changing α in increments of approximately 1°. A short pause of approximately 30 seconds was made immediately after each change of the angle of attack in order to allow the flow and freestream conditions to stabilize. A clockwise hysteresis loop can be clearly observed for angles of attack beyond $C_{l,max}$ from $\alpha = 14°$ to $\alpha = 17°$ inclusive. Two stable and distinct C_l results for a given α are obtained by increasing and

decreasing the angle of attack respectively. For example, C_l = 0.94 at α = 15° across the upstroke, while C_l = 0.68 at α = 15° across the downstroke. An even sharper drop of ΔC_l = 0.35 can be observed at α = 14°. For this case, the flow in the downstroke branch of the hysteresis loop reattaches only after the angle of attack was set below 14°. These significant differences in lift coefficients across the upstroke and downstroke branches of the hysteresis loop indicate the presence of a bistable state in the system.[34]

3.2.2 Pressure Coefficients

The lift and the quarter-chord pitching moment polars were useful in illustrating the hysteresis loop and pointed towards a bistable state of the flow about the airfoil. In order to gain a better understanding of the hysteresis process, the time-averaged pressure coefficients for both the increasing and the decreasing branches of the hysteresis loop were studied. Results for commanded α = 13°, 14°, 15° and 16° as a function of the chord location are shown in Fig. 3.4. As shown in the C_p distribution at α = 13° in Fig. 3.4 a), just before the hysteresis loop begins the surface pressure distributions are essentially identical for the upstroke and downstroke cases. They are characterized by a sharp suction peak of negative pressure near the leading edge and a pressure recovery region consisting of continuously increasing pressure in the downstream direction. Both upstroke and downstroke pressure coefficients reach a minimum of C_p = -5 at the leading edge. In contrast, the pressure distributions in Fig. 3.4 b), c), and d) display completely different behaviors during the hysteresis loop at post-stall angles of attack. For the upstroke, a high suction peak is present near the leading edge, whereas for the downstroke a region of nearly uniform pressure is observed due to a massively separated flow. It is worth noting that for the upstroke at α = 14° the suction peak observed in the upstroke is of lower pressure than the suction peak at α = 13°. This is an interesting observation because $C_{l,max}$ was reached at α = 13°, with subsequent reduction in C_l noticed at α = 14°, as discussed in Section 3.2.1. For the downstroke, the C_p distributions indicate a gradual increase in pressure of this plateau with increasing angle of attack. The persistence of the suction peak and the greater pressure recovery also describe the reason for the higher C_m exhibited by the upstroke, as compared to the downstroke in Fig. 3.3. For the upstroke, as the angle of attack is increased to α = 15°, a plateau can also be observed in the upper-surface C_p distribution, beginning at x/c = 0.20. The emergence of this plateau is also associated with a decrease in the magnitude of the suction peak at the leading edge. With further increase in angle of attack, the

magnitude of the suction peak is further decreased across the upstroke. The drastic differences in C_p distributions between the upstroke and the downstroke indicates two distinctly different flow fields for each of these cases.

3.3 Unsteady Airfoil Performance

As shown in Fig. 3.3, the airfoil performance coefficients revealed the existence of clockwise post-stall hysteresis loops both in C_l and C_m, and a counterclockwise hysteresis loop in C_d. This suggested the existence of a bistable state at a fixed angle of attack characterized by distinctly different flow fields, as discussed previously. However, the analysis of the airfoil performance coefficients and the steady surface pressure distributions did not reveal much about the flow physics and the fundamental processes that give rise to a particular state of the aforementioned bistable system. Therefore, in order to provide additional insight to the processes that were not captured by the time-averaged data, the unsteady content of the flow field was examined. Unsteady pressure measurements were taken at 3000 Hz and multiple ensembles of surface pressure data were acquired to ensure that the unsteady content of interest was sufficiently captured. The findings were discussed in detail in the following sections. Since the wind tunnel corrections resulted in slight shifts in the angles of attack from the commanded values which did not affect the interpretations of the results, the following sections utilize commanded angles of attack unless otherwise noted. For example, a commanded angle of attack of $\alpha = 15°$ resulted in a corrected value of $\alpha = 15.4°$.

3.3.1 C_p Standard Deviation

In order to better understand the unsteadiness exhibited in the post-stall flow field hysteresis, the standard deviation of the surface pressures $C_{p,SD}$ distribution was calculated. These distributions provide a general understanding of the unsteadiness in the surface pressure by essentially describing the magnitude and regularity of variations in the C_p time trace from the mean value. Fig. 3.5 presents a comparison of the $C_{p,SD}$ distributions at commanded $\alpha = 13°$, 14°, 15° and 16° for both the upstroke and downstroke. When the flow is attached at $\alpha = 13°$, a low degree of unsteadiness is observed in the acquired measurements. However, the magnitude of the $C_{p,SD}$ distribution drastically increases for post-stall angles of attack. At $\alpha = 14°$ the $C_{p,SD}$ of the upstroke remains low, though a slight elevation in unsteadiness can be observed across the aft region of the

airfoil due to the small or marginally separated flow region across the surface. However, a substantially higher $C_{p,SD}$ is produced for the downstroke at α = 14° due to the massively separated flow field. An interesting observation is the abnormally high values of the $C_{p,SD}$ in the first 20% of the chord for the upstroke at α = 15° and α = 16°, which correlates to the region associated with the suction peak in Fig. 3.4 c) and d). Across this region, the unsteadiness associated with the upstroke is actually higher than that associated with the downstroke. However, downstream of this suction peak the unsteadiness in the surface pressure decreases below those associated with the downstroke.

3.3.2 Airfoil Flow Field Spectral Content

The acquired unsteady pressure measurements were also used to characterize the spectral content of the flow and identify the unsteady modes which produced the unique signatures of the $C_{p,SD}$ distributions in Fig. 3.5. The resulting premultiplied C_p spectra produced at α = 14°, 15°, and 16° are shown in Fig. 3.6 for the upstroke and downstroke cases. Since the flow is attached for both the upstroke and downstroke at α = 13°, the spectra at this angle of attack are not shown due to the lack of relevant spectral content. From Fig. 3.6 a), no significant spectral content is observed in the unsteady C_p distribution across the upper surface at α = 14° during the upstroke. In contrast, concentrated regions of high spectral content can be observed at α = 14° during the downstroke in Fig. 3.6 d). Two distinct regions of unsteadiness can be observed, with a low-frequency contribution centered at St = 0.02 in the region upstream of x/c = 0.20 as well as a higher frequency centered at St = 0.14 across the region between x/c = 0.20 and x/c = 0.90. The Strouhal number of the unsteadiness across the leading-edge region is consistent with prior studies on circulation-induced low-frequency oscillations in airfoil surface pressure and lift.[8,18-22] Additionally, the spectral content of the low-frequency oscillation is predominantly observed across the leading-edge region, similar to Bernardini et al.[21] Further comparison of Fig. 3.5 and Fig. 3.6 indicates that the unusually-high values of $C_{p,SD}$ observed across the leading-edge region for the upstroke at α = 15° and α = 16° is attributed to the low-frequency oscillations occurring at approximately St = 0.02. Similarly, the Strouhal number of the unsteadiness across the downstream regions of the airfoil are consistent with typical values for bluff-body shedding, including Roshko's Strouhal scaling of 0.14 for normally-oriented flat plates.[16]

For the upstroke at α = 15°, the low-frequency spectral peak can be observed upstream of x/c = 0.20 in Fig. 3.6 b). This low-frequency unsteadiness is similar, but much more narrow-band and isolated as compared to that observed for the downstroke at α = 14° in Fig. 3.6 d). Conversely, for the downstroke at α = 15° in Fig. 3.6 e), the low-frequency oscillations are perceptible upstream of x/c = 0.20, though the magnitude is significantly decreased as compared to the upstroke. Similarly, the spectral peak associated with bluff-body shedding can also be observed for the upstroke at α = 15° in Fig. 3.6 b) between x/c = 0.5 and x/c = 1.0, though the amplitude is much lower and the streamwise extent of the spectral peak is smaller than that observed for the downstroke in Fig. 3.6 e). This decrease in the length and magnitude of the bluff-body shedding in the premultiplied spectrum is due to the smaller extent of the separated flow for the upstroke. Comparison of Fig. 3.6 c) and f) reveals consistent trends for α = 16° with those observed at α = 15°, although the spectral amplitudes are lower at α = 16°.

Interestingly, it is observed that, with the exception of the upstroke at α = 14° when the flow is mostly attached, the spectral energy of the post-stall unsteadiness is higher at lower angles of attack. This observation is consistent with the $C_{p,SD}$ distributions from Fig. 3.5, where the highest measure of unsteadiness was observed during the downstroke at α = 14°. As the angle of attack increases, the unsteadiness in the separated flow field would be expected to also increase. However, as the recirculation region of the separated flow grows, the shear layer forms father off the surface of the airfoil. Therefore, the decrease in the spectral amplitudes as the angle of attack increased could be attributed to a decreased influence of the shear layer unsteadiness to the surface pressure measurements.

In order to provide an additional comparison of the spectral content, the premultiplied spectra across the upstroke (blue) and downstroke (red) are shown in Fig. 3.7 and Fig. 3.8 for α = 14°, α = 15°, and α = 16°. Only the leading-edge region is shown in Fig. 3.7 to provide a detailed comparison of the low-frequency oscillations, while spectra for the C_p acquired across a greater extent of the airfoil upper surface are shown in Fig. 3.8 to display the bluff-body shedding frequencies. The spectra displayed in both Fig. 3.7 and Fig. 3.8 have been offset by a factor of 1×10^4 for each sequential downstream location in order to assist in making comparisons between the spectra between different locations.

From Fig. 3.7, the same narrow-band of amplified low-frequencies observed in Fig. 3.6 are identified across the leading-edge region. This low-frequency content can also be seen across the

upstroke at α = 15° and α = 16° in Fig. 3.8 b) and c) across the entire airfoil upper surface, even after the spectral content of the bluff-body shedding emerges. This result indicates that, while predominantly identified across the leading edge, the low-frequency oscillations actually contribute to the unsteadiness across the entire surface. This mechanism is consistent with the viscous-inviscid coupling effects discussed by Ansell and Bragg[22] and Sandham[35], where the low-frequency oscillations are representative of a feedback-based variation of the airfoil circulation in response to the separated flow. In previous studies, the low-frequency oscillations were thought to be similar to a quasi-periodic oscillation in the airfoil circulation, similar to what would be an oscillating circulation strength vortex in a freestream potential flow. As a result, the low-frequency mode would be expected to be present across the entire airfoil surface.

Observations from the literature have also identified an increase in the spectral energy associated with vortex shedding at high angles of attack is accompanied by a decrease in the bandwidth and the dimensional center frequency of the spectral peak.[31,36] This observation is consistent with what can be seen in the bluff-body shedding frequencies in Fig. 3.8. Across the upstream portion of the separated region, the bluff-body oscillations are associated with a broad-band, high-frequency distribution of energy. In contrast, with increased streamwise distance to the trailing edge, more amplified content with distinct center frequencies can be seen. An interesting observation is that at almost any point, until the trailing edge is reached, the spectral content of the downstroke branch of the hysteresis loop exhibits higher amplitudes than the upstroke branch. This is interpreted as higher unsteadiness in the flow in the downstroke, consistent with prior studies on hysteresis.

3.3.3 Airfoil Unsteady Lift Coefficient

As shown in Fig. 3.6, the low-frequency oscillations were predominantly present in the pressure spectrum around the leading edge. However, further investigation of the power spectral densities showed that traces of the low-frequency oscillation were detected across the entire surface of the airfoil. This, as previous studies have suggested, implied that the observed oscillations are possibly related to global oscillations in the flow circulation. In their study on low-frequency oscillations Bernardini et al.[21] highlight, as it has been documented experimentally and numerically in the literature, that large amplitude low-frequency oscillations in the lift force are generally detected for airfoils experiencing leading edge type stall at post-stall angles of attack.

This behavior, in combination with the classification of the airfoil performance at the studied Reynolds number as a combined leading-edge and trailing-edge type, matches the observed oscillations in the spectral content.

To more conclusively illustrate this observation, the unsteady lift coefficient was calculated. Fig. 3.9 shows an example of the observed variation in the lift coefficient for angle of attack of $\alpha = 15°$ over a time period of one second. The data for different angles of attack followed a similar pattern. The upstroke data for $\alpha = 15°$ is compared against the more irregular and chaotic lift variations observed in the downstoke branch of the hysteresis loop. This is consistent with the literature and confirms the previous observation that the unsteadiness during the downstroke is elevated compared to the upstroke. Furthermore, the observed variations in lift coefficient during the upstroke occur at a frequency that is consistent with the low-frequency mode described in greater detail in Section 3.3.2, thus confirming the suggestion that the observed low-frequency oscillations in the flow field have a direct effect on lift. The plot in Fig. 3.9 reveals some of the irregularities, such as variations in amplitude, that are present in the cyclic behavior characteristic of the unsteady lift coefficient. These irregularities further justify the classification of the low-frequency mode as quasi-periodic. In order to provide a more complete characterization of the low-frequency oscillations in C_l, the premultiplied spectra observed in the lift across the upstroke is presented in Fig. 3.10. The spectrum resembles the PSDs of the C_p distribution with two distinct regions of higher spectral content. These regions coincide with the previously observed low-frequency and bluff body shedding modes.

3.4 Time Resolved Particle Image Velocimetry

In order to provide a further understanding of the underlying mechanisms contributing to the flow field unsteadiness, measurements of the velocity field across the leading-edge region of the airfoil were acquired using TR-PIV at $\alpha = 14°$, 15°, and 16°. The vector fields for each of these cases consisted of 5,458 instantaneous velocity fields. Only results associated with $\alpha = 15°$ will be presented here, due to the similarity in results observed between different angles of attack, with the exception of $\alpha = 14°$ where no dominant unsteady contributions were identified for the upstroke.

After carefully examining the sequential TR-PIV velocity field data for the upstroke and downstroke branches of the hysteresis loop, a quasi-periodic movement of the location of the

boundary layer separation point was noticed. As a quasi-periodic process, it was characterized by distinct cycle to cycle irregularities such as variations in the amplitude and the period of the oscillations. However, the overall process occurred at a frequency comparable to the low-frequency oscillation mode observed in the spectral content of the flow. As noted in Section 3.3.2 the low-frequency mode was perceptible in the spectral content observed in the downstroke branch of the hysteresis loop. However, the amplitude of this mode was significantly lower than the magnitude of the oscillation in the upstroke case. This was reflected in the TR-PIV data collected for the downstroke cases. It was observed that the downstroke branch was not associated with a well-defined global variation in the flow field across the series of sequential TR-PIV data. While local variations exist from instance to instance due to vortex shedding, the movement in the separation location does not substantially change, and the shear layer for the downstroke remained relatively fixed.

A closer examination of the acquired instantaneous velocity fields for the upstroke branch revealed details about the quasi-periodic oscillation in the flow and some of the processes associated with it. A set of equally spaced instantaneous velocity fields, along with the corresponding *z*-vorticity fields, were extracted from a single cycle out of the full data for the upstroke branch of the hysteresis loop. These example instantaneous fields are presented in Fig. 3.11 - Fig. 3.14. From Fig. 3.11, at the beginning of the oscillation for the upstroke, the flow separation point is located upstream relative to the other instances in time. However, at the next instance of the oscillation process in Fig. 3.12, the flow separation location begins to move downstream and the velocity at the leading edge slightly increases. Then, the boundary layer about the leading edge of the airfoil re-establishes to form a local suction peak in Fig. 3.13. This is visualized as a surging flow about the leading edge of the airfoil. As a result, the separation location is moved farther downstream and the flow velocity around the leading edge of the airfoil is higher than that of the preceding instances of the low-frequency cycle. The shear layer has been deflected closer towards the airfoil surface at this instance. This development suggests that the boundary layer has reached an attached or marginally attached state at the leading edge of the airfoil, where it was once separated. This behavior is similar to the quasi-periodic stalling and unstalling behavior observed for low-frequency oscillations in previous studies.[20] Across later phases (Fig. 3.14) of the oscillation process for the upstroke branch, the accelerated flow region about the leading edge has begun to subside. After that, the flow again returns a state similar to the one in the beginning

of the cycle. The separation point also retreats back upstream to complete one oscillation. A closer examination of the flow fields revealed that the upstream movement of the separation location process was associated with shedding of small-scale vortices which appear to coalesce in a larger-scale vortex (Fig. 3.14). This mechanism is believed to be similar to the one observed by Bernardini et al.[21] for flow control-induced low-frequency oscillations of a post-stall airfoil.

As instantaneous flow fields are not necessarily representative of the overall process due to irregularities and variations in the flow, the off-body flow field associated with the low-frequency oscillation was studied through a conditional averaging process. For this purpose, a single cycle was divided in 4 distinct phase angles – $\phi = 0, \pi/2, \pi, 3\pi/2$. Each of these phase angles corresponded to one quarter of the period of the low-frequency oscillation. The phase angle corresponding to $\phi = 2\pi$ from a given cycle coincided with the phase angle $\phi = 0$ from the next cycle. Since the low-frequency oscillation process was only quasi-periodic, the beginning of each cycle was determined by identifying the instance of local maximum in the velocity within the external, inviscid region of the flow. Therefore, the irregularities in the cycles were accounted for by this conditional averaging process.

The resulting conditionally averaged flow fields are presented in Fig. 3.15, Fig. 3.16, Fig. 3.17, and Fig. 3.18. Contour plots were used to show the magnitude of the flow velocity normalized by the freestream velocity. The *x*- and *y*-direction velocity components are overlaid on top of these contour plots. Conditionally averaged vorticity fields for the same phase angles are presented in parallel with the velocity fields. The conditionally averaged vorticity fields were useful for providing insights into the evolution of the flow field and the location of the shear layer in particular. The instance when the boundary layer separation location was farthest downstream, which is equivalent to the surging of the flow about the leading edge, was set as phase angle $\phi = 0$. The averaged velocity field for $\phi = 0$ shows a region of high flow velocity across the leading edge of the airfoil (Fig. 3.15 a). The flow slows down in the downstream direction and a region reversed flow is observed. Fig. 3.15 b) shows the vorticity distribution which approximately tracks the location of the shear layer. Across the next phase of the oscillation process $\phi = \pi/2$, the accelerated flow region about the leading edge begins to subside and the separation location moves upstream, as shown in Fig. 3.16 a). This upstream movement in the separation location is also observed in the shear-layer location which is approximately tracked by the vorticity distribution (Fig. 3.16 b). During the phase angle of $\phi = \pi$, the velocity across the leading edge has reached its

lowest value and the separation location has moved farthest upstream as seen in Fig. 3.17 a). It is worth noting that the upstream movement of the separation point is accompanied by an increase in vorticity shed from the airfoil (Fig. 3.16 b and Fig. 3.17 b). Across the later phases of the cycle, the flow starts to re-establish over the leading-edge region of the airfoil to form a local suction peak. At $\phi = 3\pi/2$ (Fig. 3.18) the velocity field resembles that observed at $\phi = \pi/2$. Finally, as the phase angle $\phi = 2\pi$ coincides with $\phi = 0$, the low-frequency oscillation has completed one cycle, making the flow again reach characteristic velocity and vorticity contours of Fig. 3.15 a) and b).

It should be noted that the velocity variation across the low-frequency oscillation associated with the upstroke branch is quite substantial. The flow across the leading edge at the phase angle $\phi = 0$ reached an average velocity magnitude of V = 55.5 m/s, which is a 38.75% higher than the freestream. In contrast, at $\phi = \pi$, when the separation point was farthest upstream, the average velocity magnitude was V = 48.7 m/s – a value 21.75% higher than the freestream. The velocity difference between the two extremes of the low-frequency oscillation cycle was calculated to be 17% relative to the freestream velocity. To better visualize the observed surging behavior of the flow across the extremities of the cycle ($\phi = 0$ and $\phi = \pi$), Fig. 3.19 provides a comparison between the areas in the flow field where the velocity was above 46 m/s or 1.15 times the freestream velocity. This velocity difference is predominantly observed across the leading-edge region of the airfoil, providing further understanding on the source of the unsteadiness observed in the C_p across this region in Fig. 3.5. Furthermore, this surging of the flow is accompanied by a significant chordwise movement of the separation location within a single cycle. The change in the separation location between phase angles $\phi = 0$ and $\phi = \pi$ was calculated to be 11.8% of the airfoil chord length. This movement is illustrated in Fig. 3.20 where the dashed lines show the Δx between $\phi = 0$ and $\phi = \pi$. Fig. 3.20 also shows the stagnation streamlines, demarcating the regions of reverse flow, for the corresponding cases. This analysis of the TR-PIV results indicates that, rather than the unsteadiness being due to a distinct vortex shedding process or directly due to a formation of coherent, periodic structures, the low-frequency oscillations across the leading edge are produced by a local surging of the flow velocity associated with an unstalling behavior. Additionally, the total period of the oscillation observed in the TR-PIV data was consistent with the dimensional frequency of the oscillations observed in the spectrum content of the flow.

3.5 Chapter 3 Figures

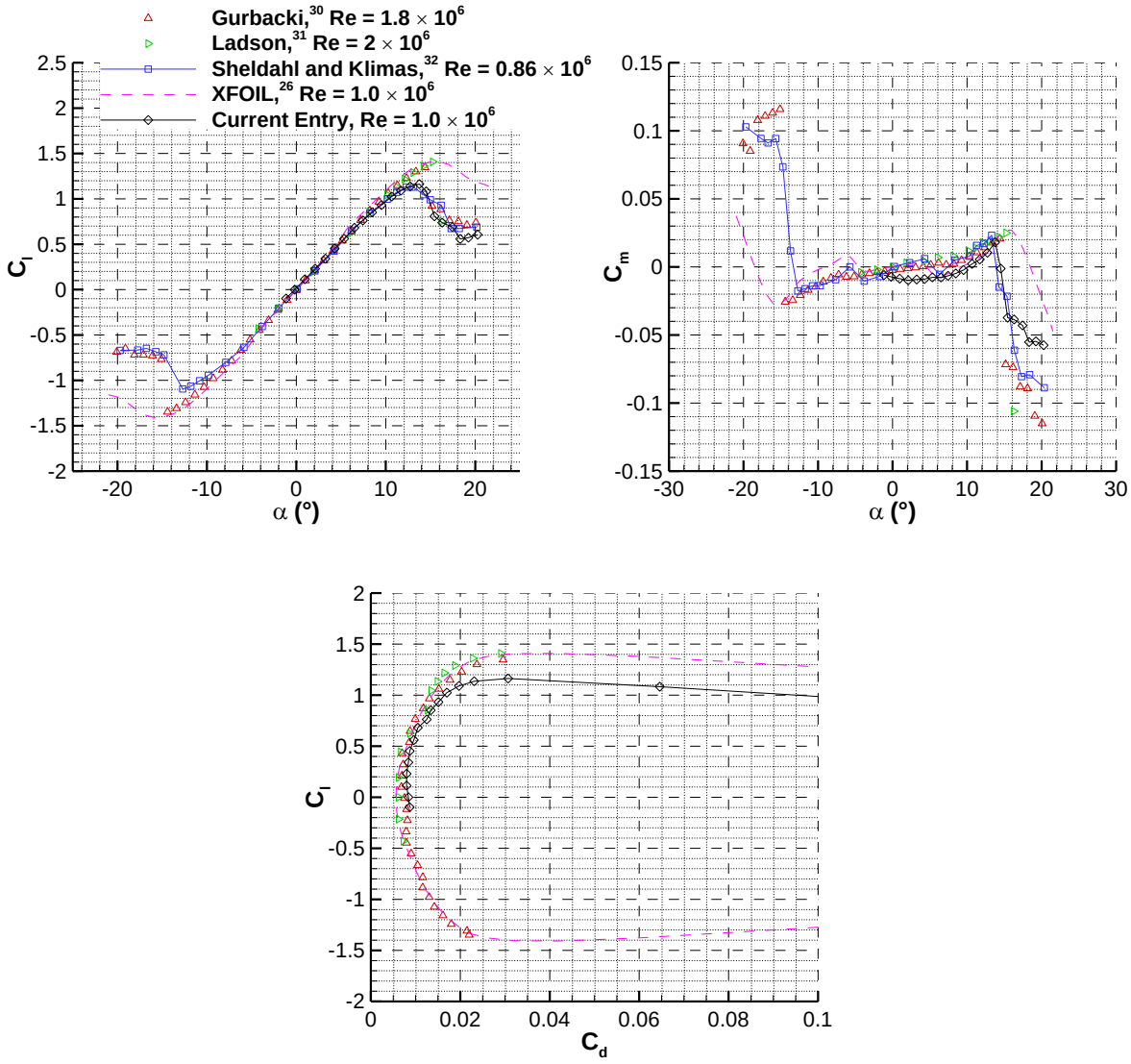

Fig. 3.1 Comparison of NACA 0012 airfoil data from the current study to performance results reported in the literature and XFOIL.

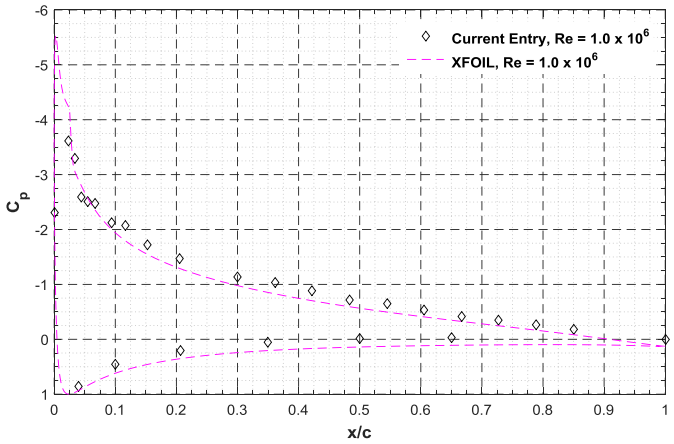

Fig. 3.2 Comparison of NACA 0012 airfoil C_p distribution from the current investigation to XFOIL calculations; all data corresponds to α = 10°.

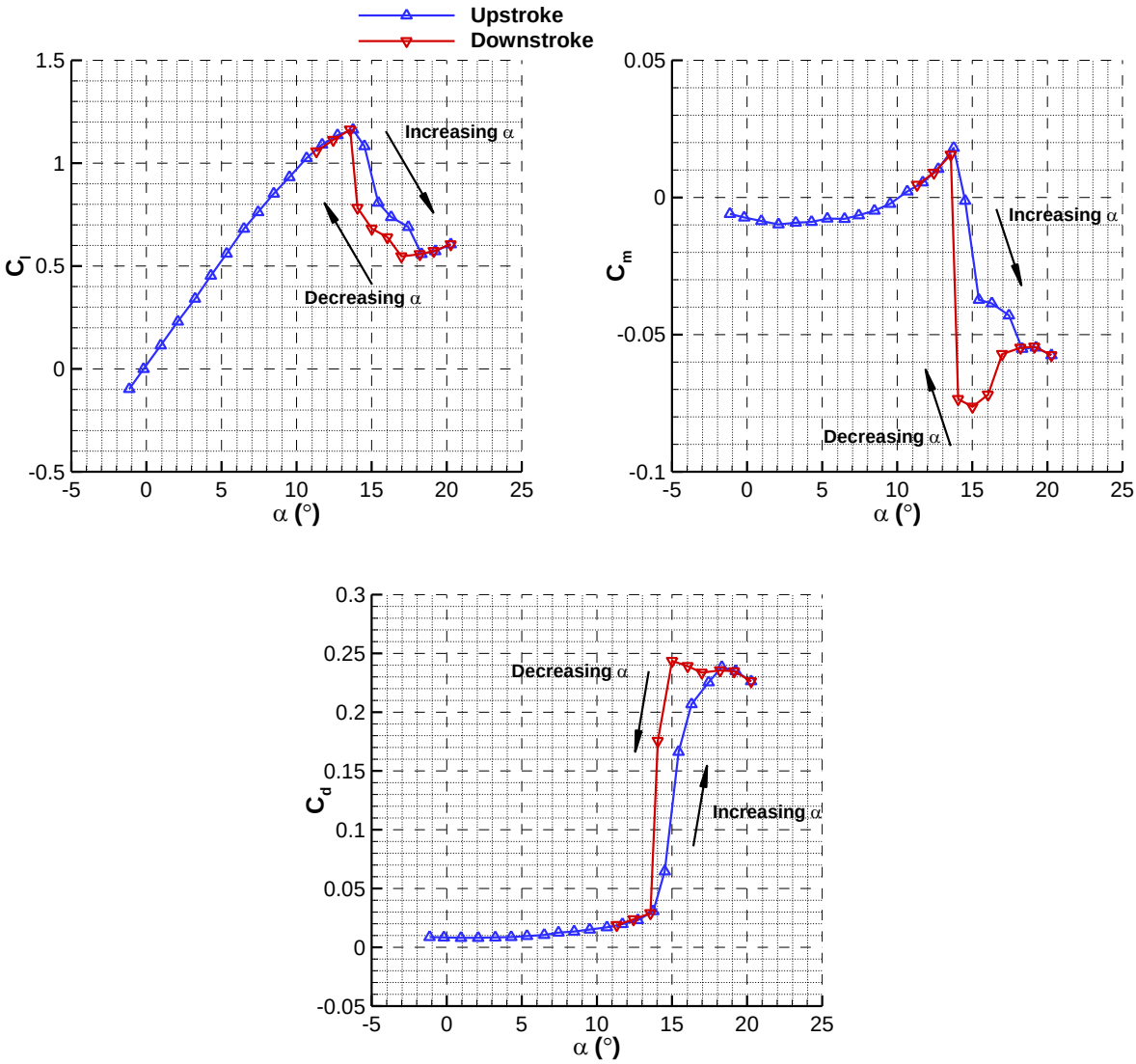

Fig. 3.3 Performance of NACA 0012 airfoil (Re_c = 1 × 10^6), with upstroke and downstroke across post-stall angles of attack.

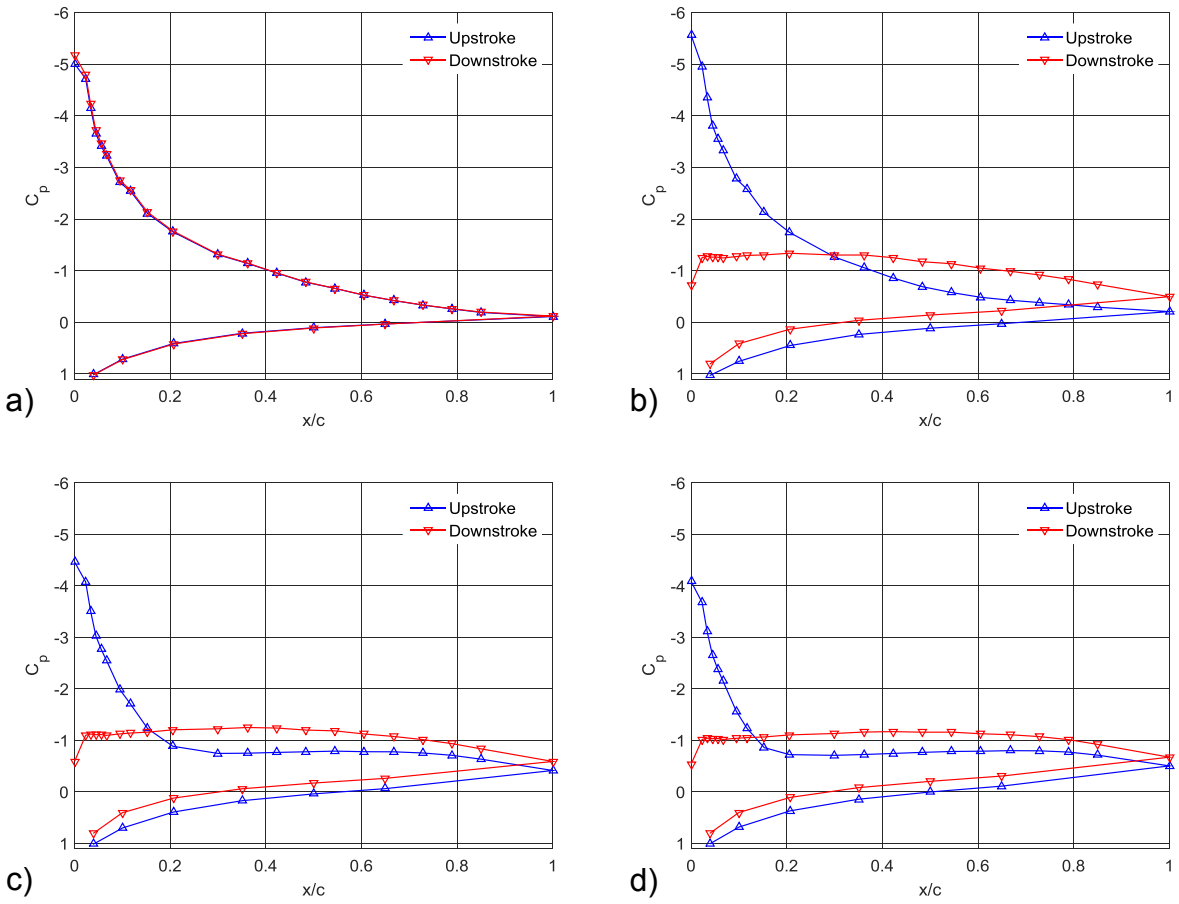

Fig. 3.4 Comparison of C_p distributions for the NACA 0012 ($Re_c = 1 \times 10^6$) across the upstroke and downstroke branches, for a) $\alpha = 13°$, b) $\alpha = 14°$, c) $\alpha = 15°$, and d) $\alpha = 16°$.

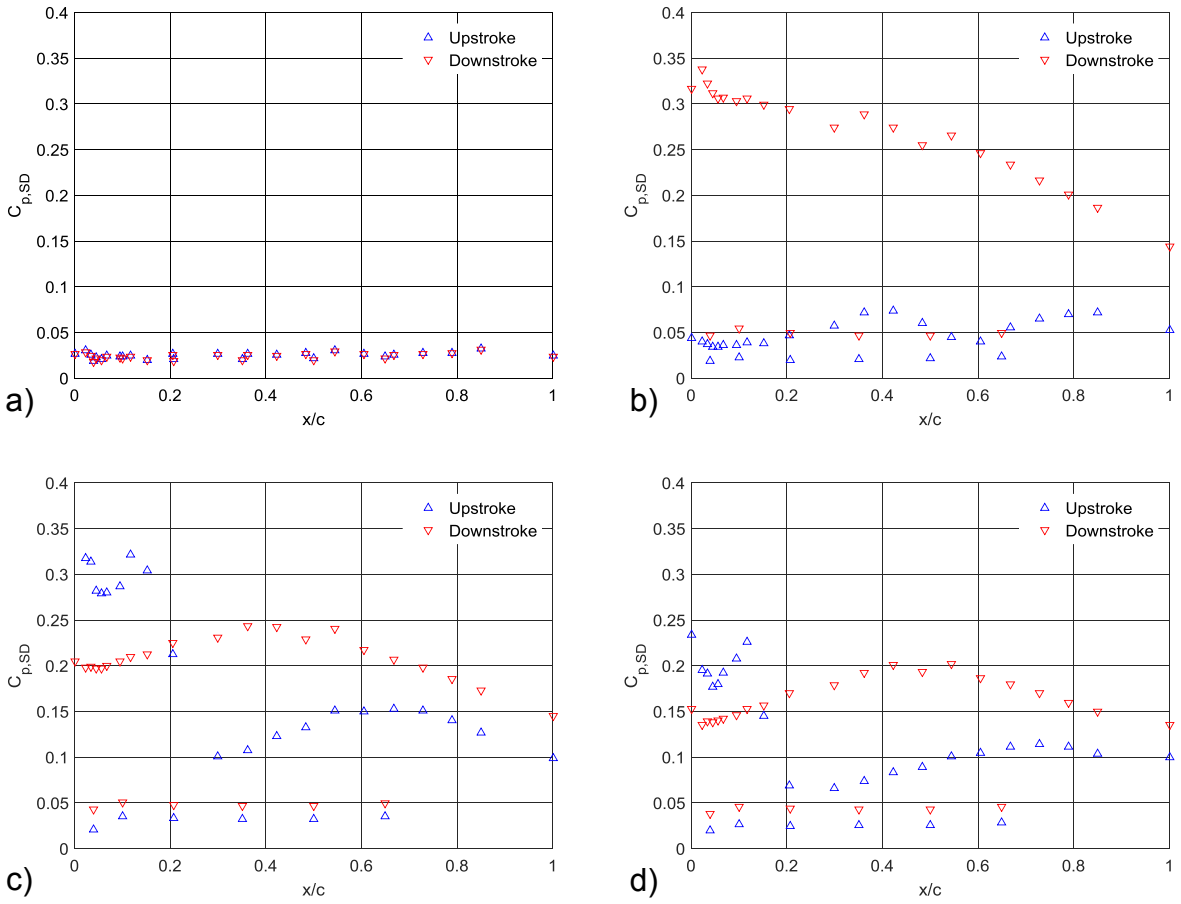

Fig. 3.5 Comparison of the $C_{p,SD}$ distribution around the NACA 0012 (Re_c = 1 × 10^6) for the upstroke and the downstroke at a) α = 13°, b) α = 14°, c) α = 15°, and d) α = 16°.

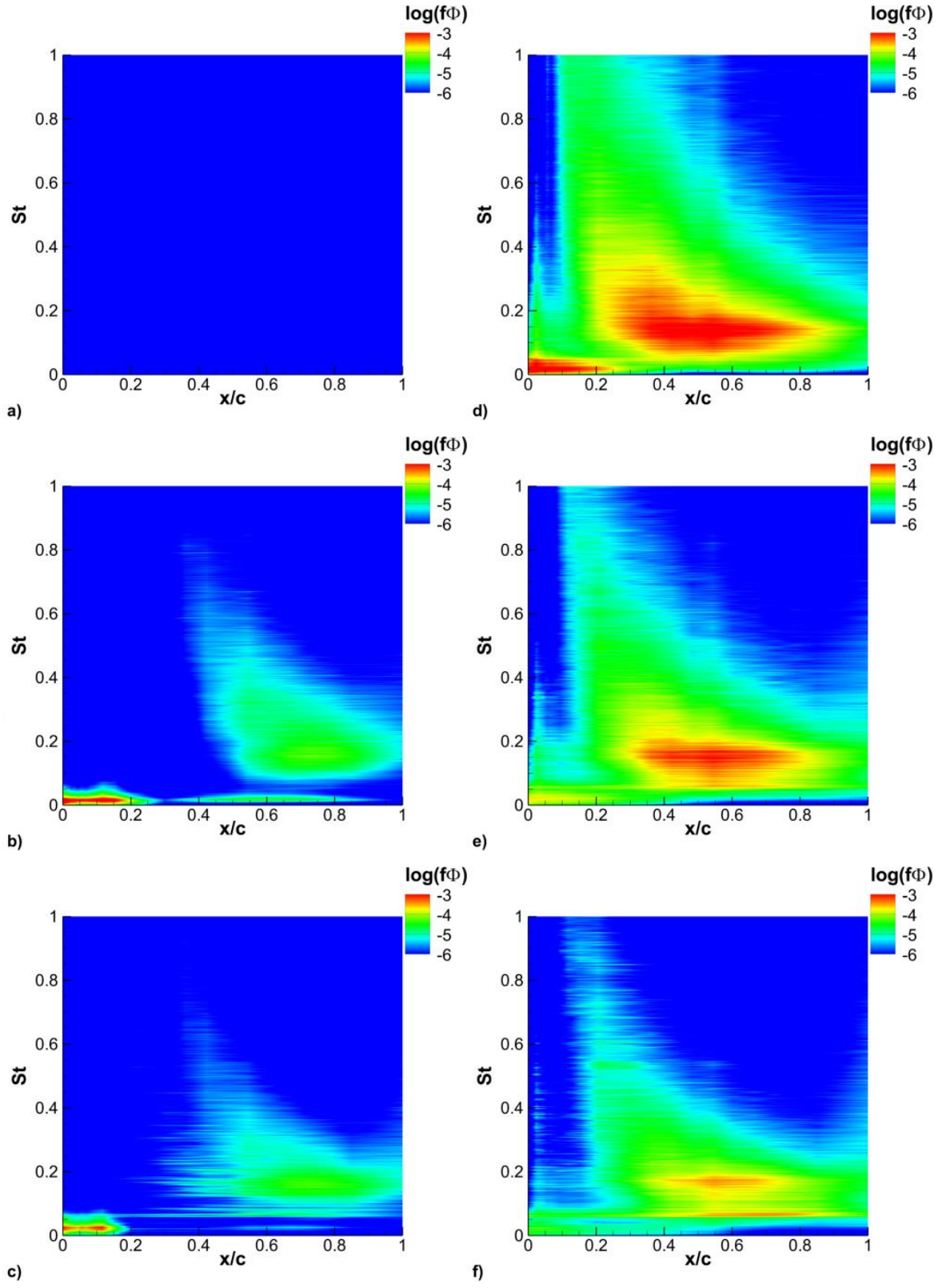

Fig. 3.6 Isocontour of premultiplied spectra across airfoil upper surface for upstroke: a) α = 14°, b) α = 15°, c) α = 16°; downstroke: d) α = 14°, e) α = 15°, f) α = 16°.

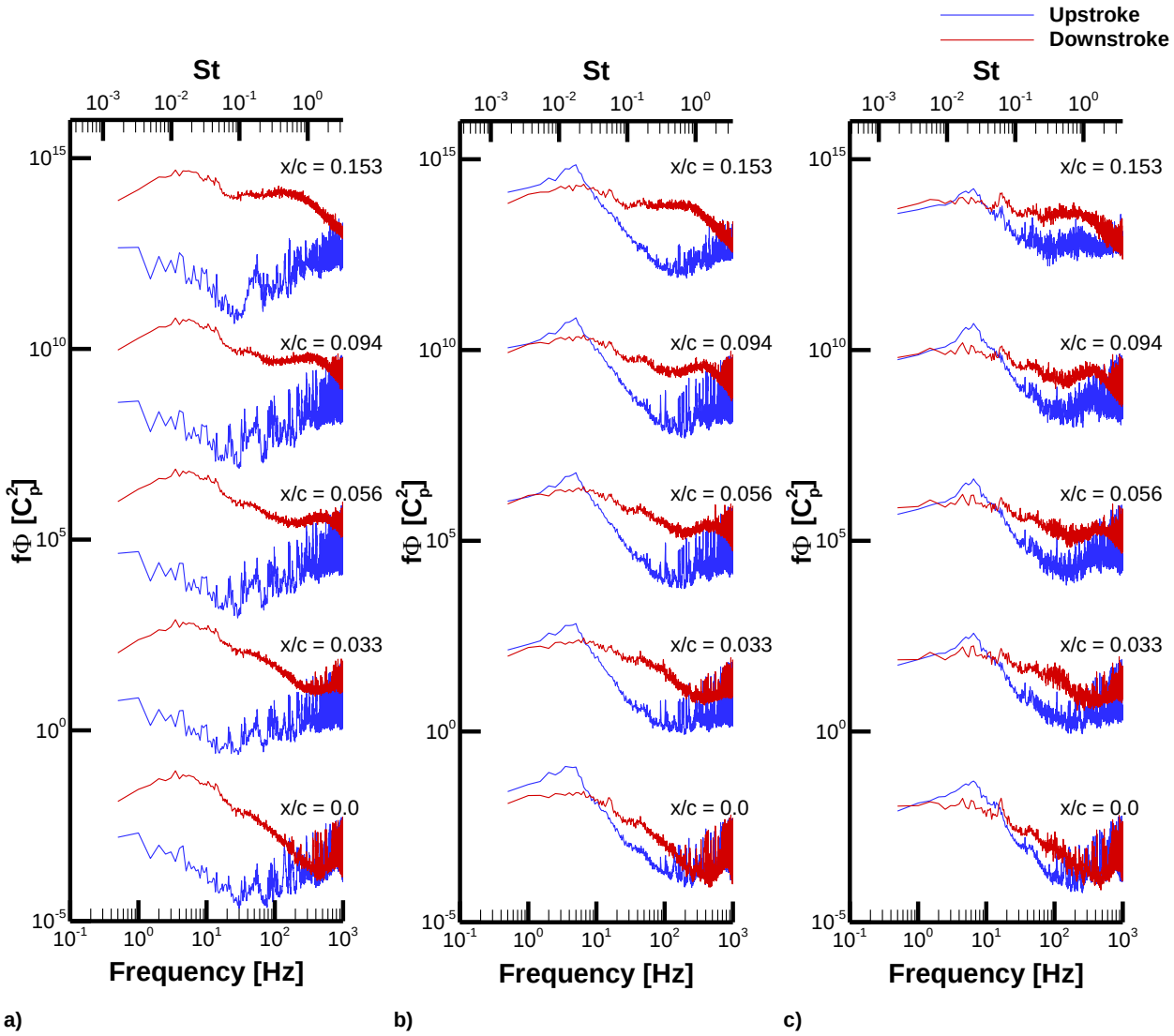

Fig. 3.7 Premultiplied spectra for unsteady C_p measurements acquired across the leading-edge region during both the upstroke and downstroke branches: a) α = 14°, b) α = 15°, c) α = 16°.

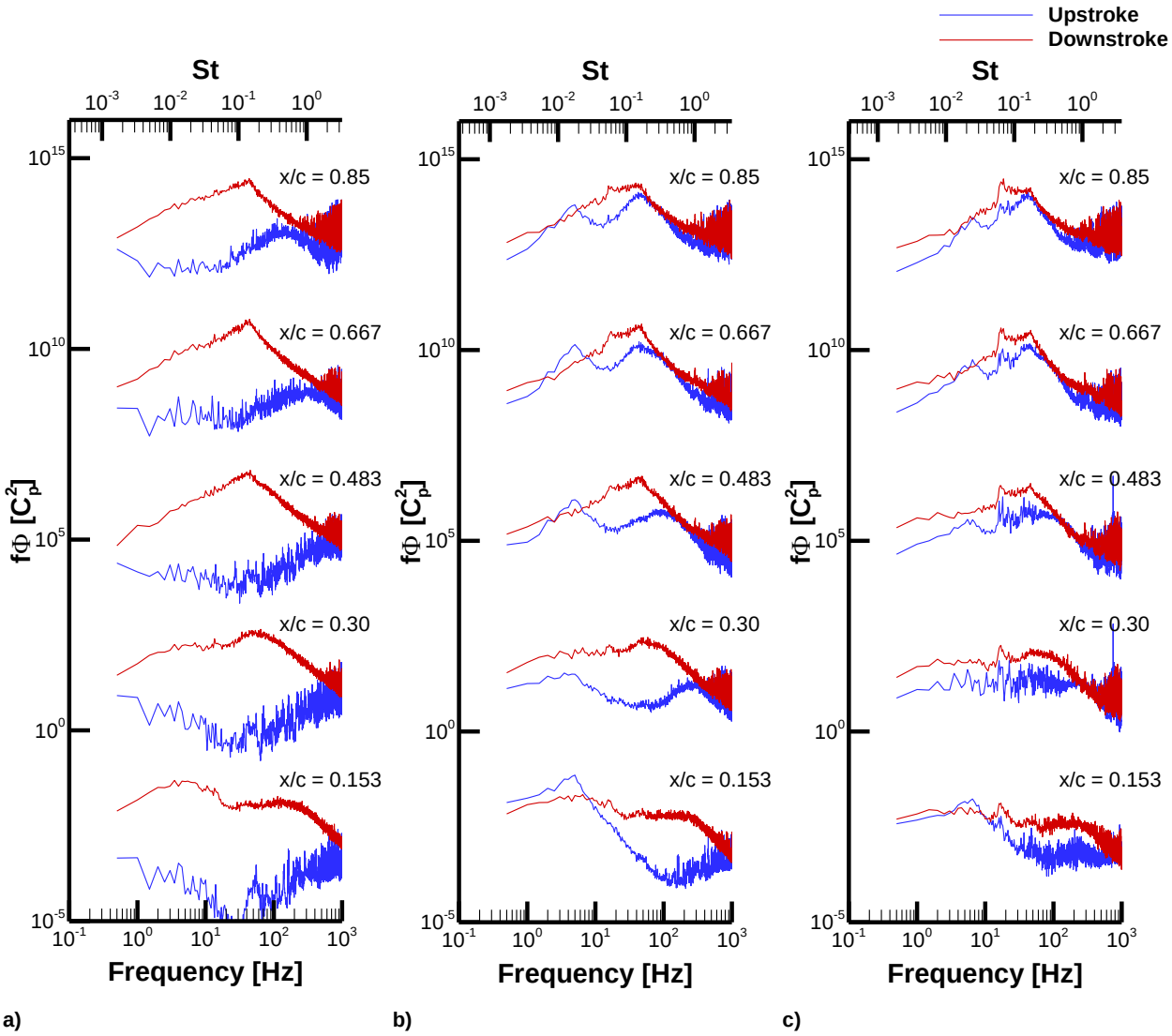

Fig. 3.8 Premultiplied spectra for unsteady C_p measurements acquired across the airfoil upper surface during both the upstroke and downstroke branches: a) α = 14°, b) α = 15°, c) α = 16°.

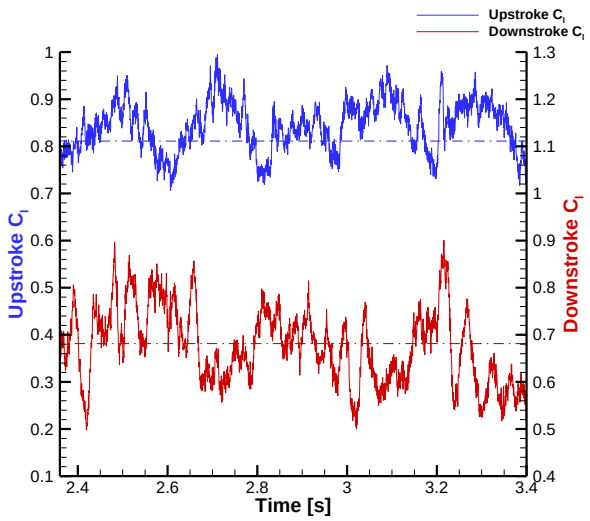

Fig. 3.9 Variation of C_l with time during the upstroke and downstroke branches of the hysteresis loop for NACA 0012 at α = 15°. The average C_l value for each case is shown with a dotted line.

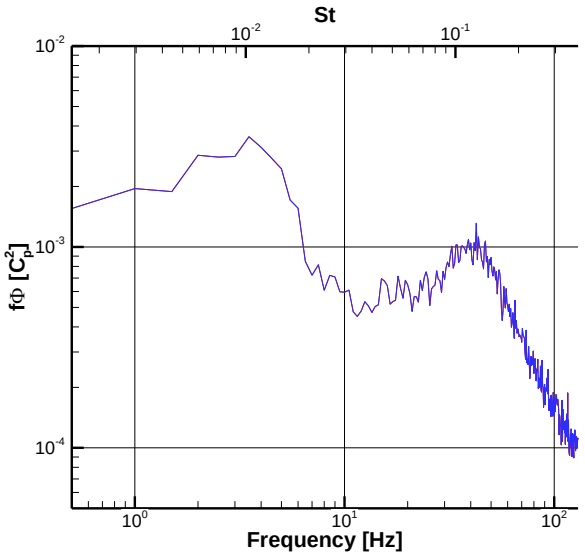

Fig. 3.10 PSD of unsteady C_l during the upstroke branch of the hysteresis loop for NACA 0012 at α = 15°.

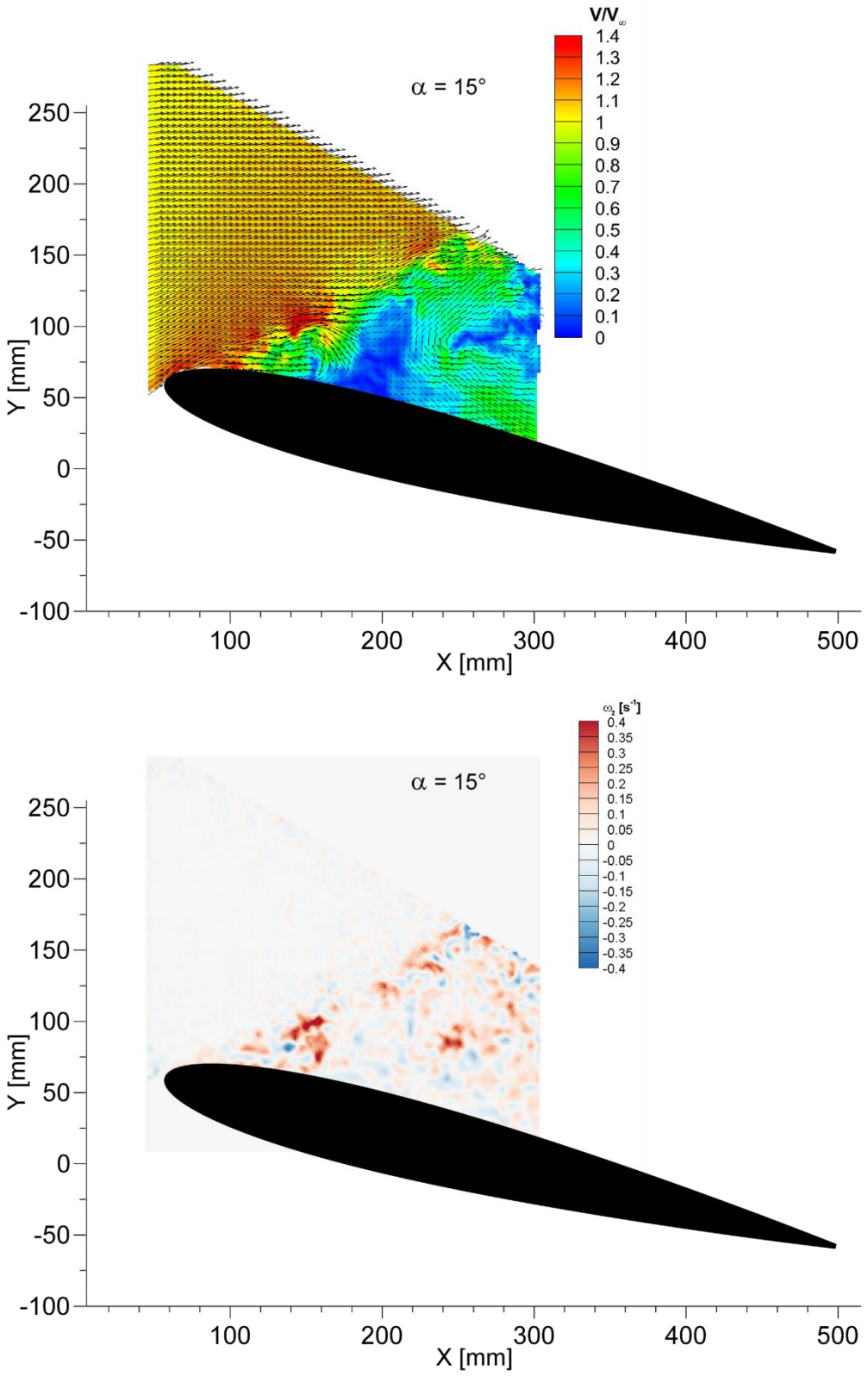

Fig. 3.11 Instantaneous time-resolved PIV velocity a) and vorticity data b) for α = 15° during upstroke when the separation point is farthest upstream and the size of the recirculation area is largest.

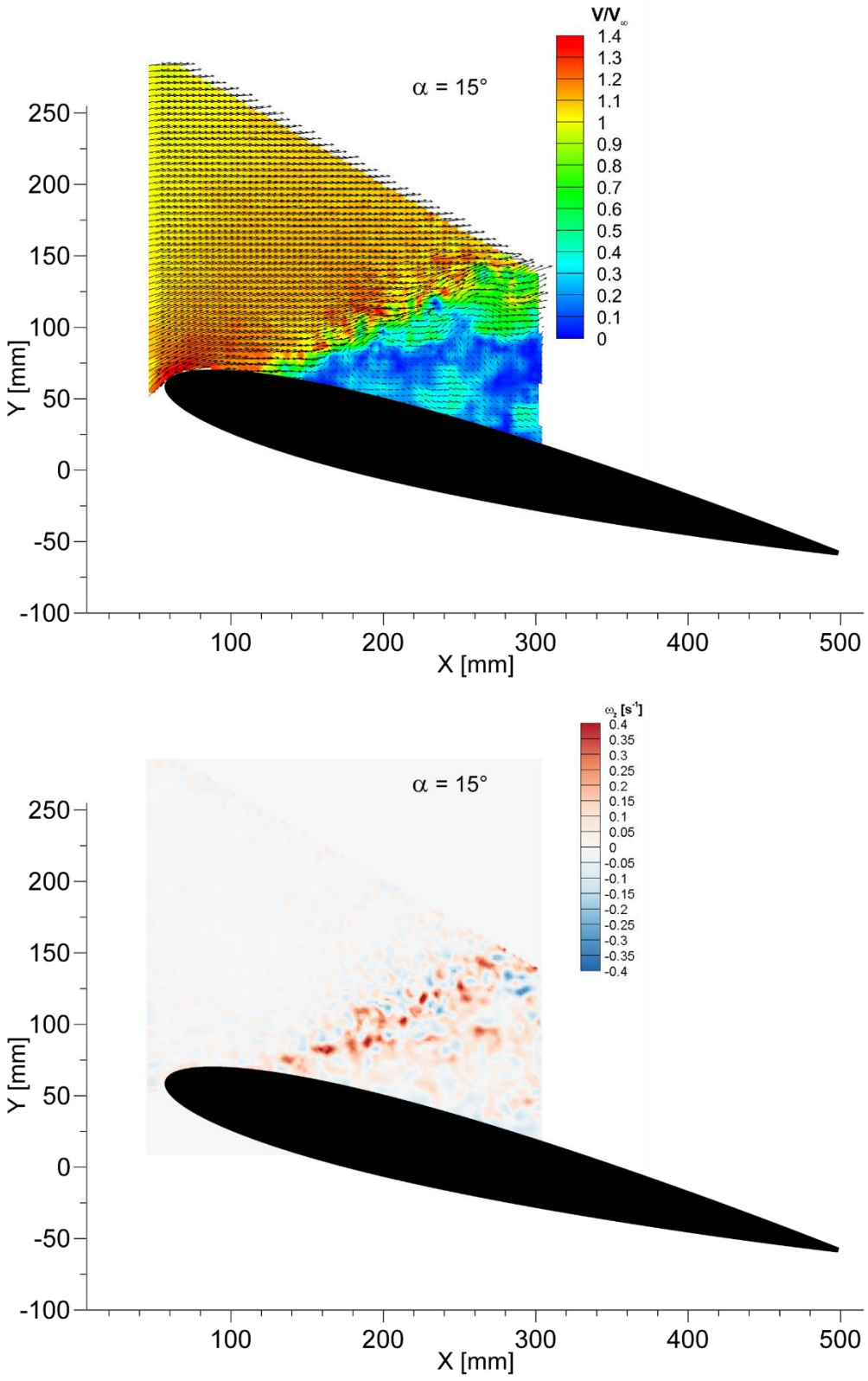

Fig. 3.12 Instantaneous time-resolved PIV velocity data a) and vorticity data b) for α = 15° during upstroke when the separation point moves downstream.

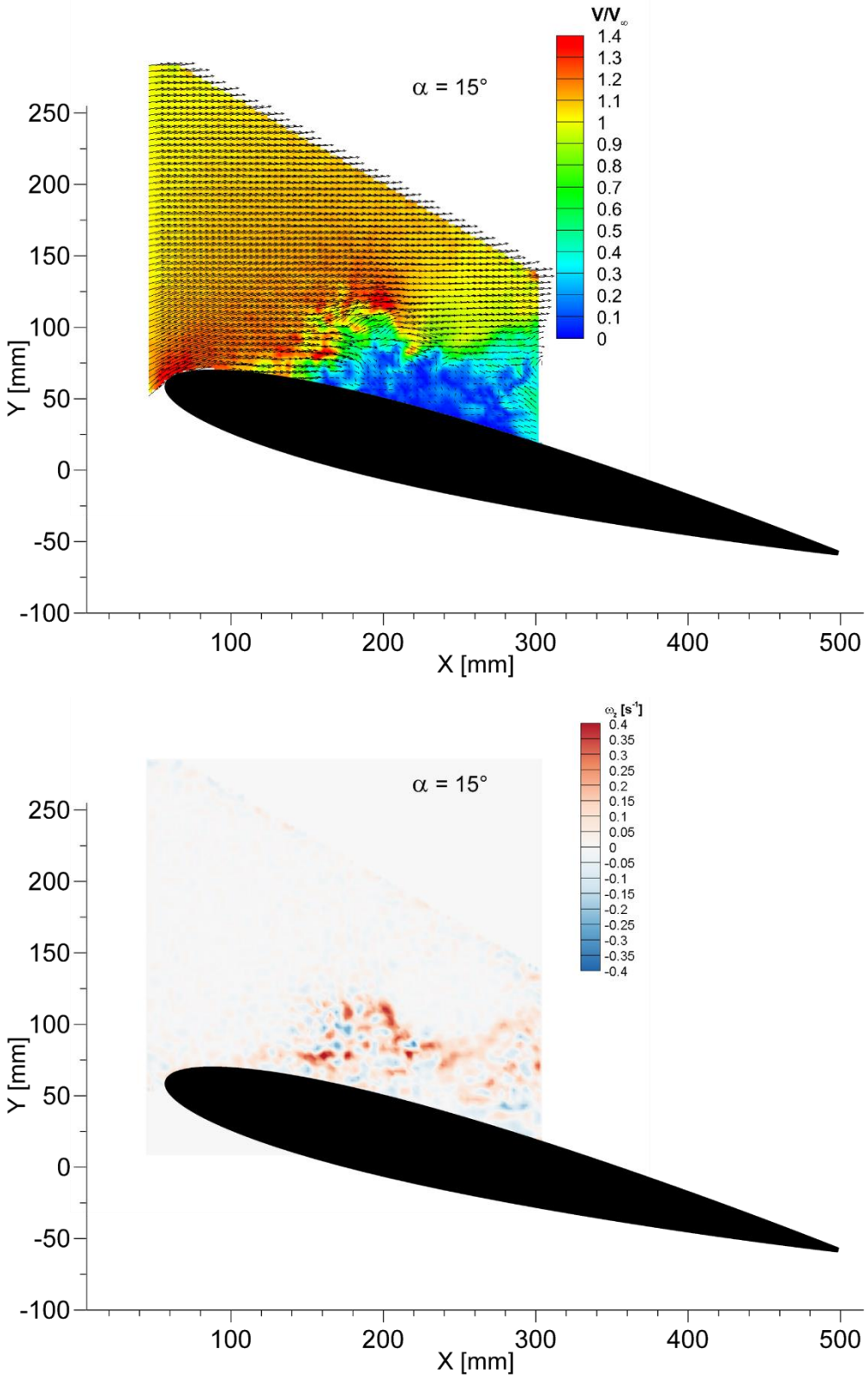

Fig. 3.13 Instantaneous time-resolved PIV velocity data a) and vorticity data b) for α = 15° during upstroke when the separation point is farthest downstream and the size of the recirculation area is lowest.

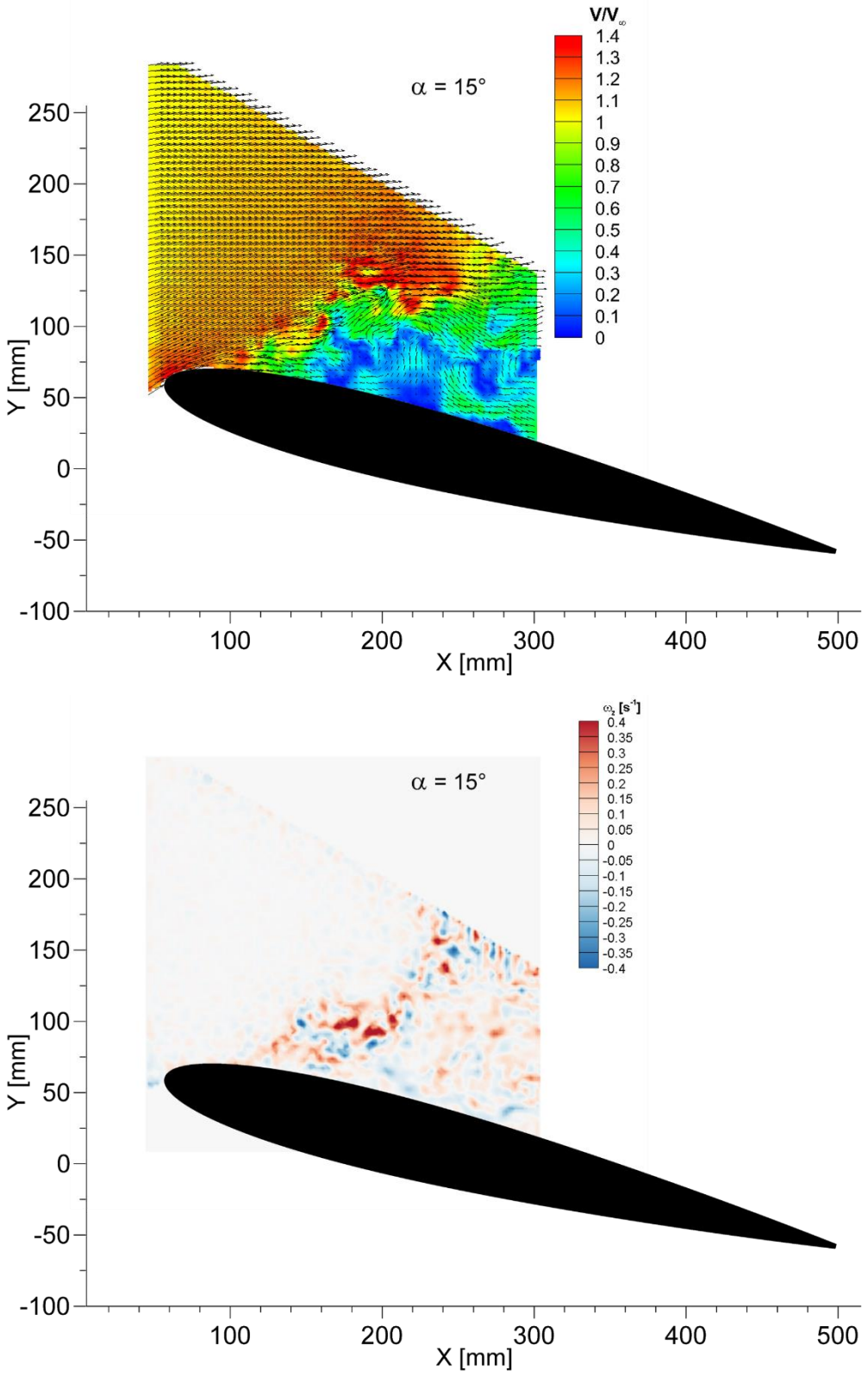

Fig. 3.14 Instantaneous time-resolved PIV velocity data a) and vorticity data b) for α = 15° during upstroke when the separation point moves upstream.

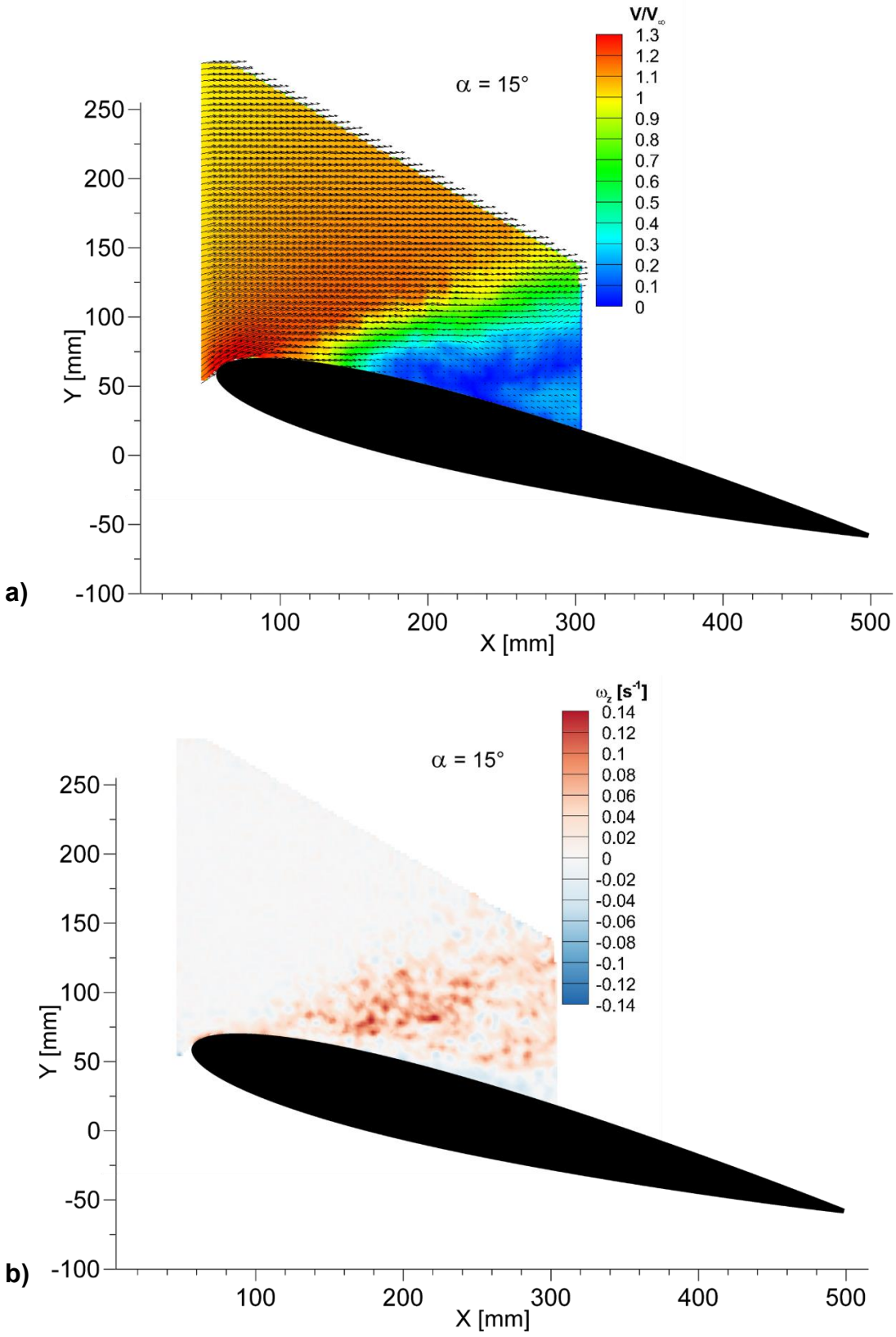

Fig. 3.15 Conditionally averaged time-resolved PIV velocity data a) and vorticity data b) for α = 15°, during upstroke phase angle Φ = 0.

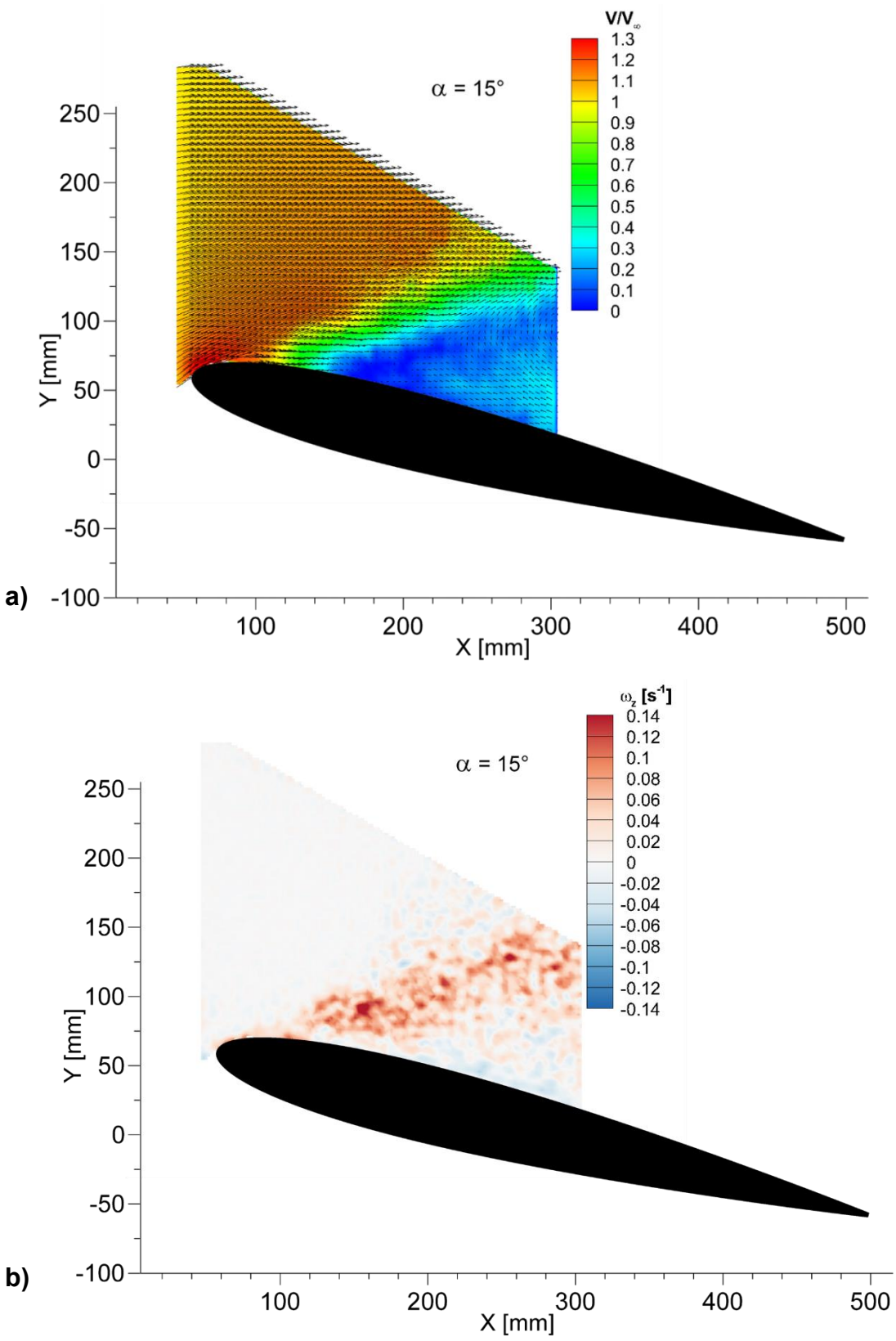

Fig. 3.16 Conditionally averaged time-resolved PIV velocity data a) and vorticity data b) for α = 15°, during upstroke phase angle $\Phi = \pi/2$.

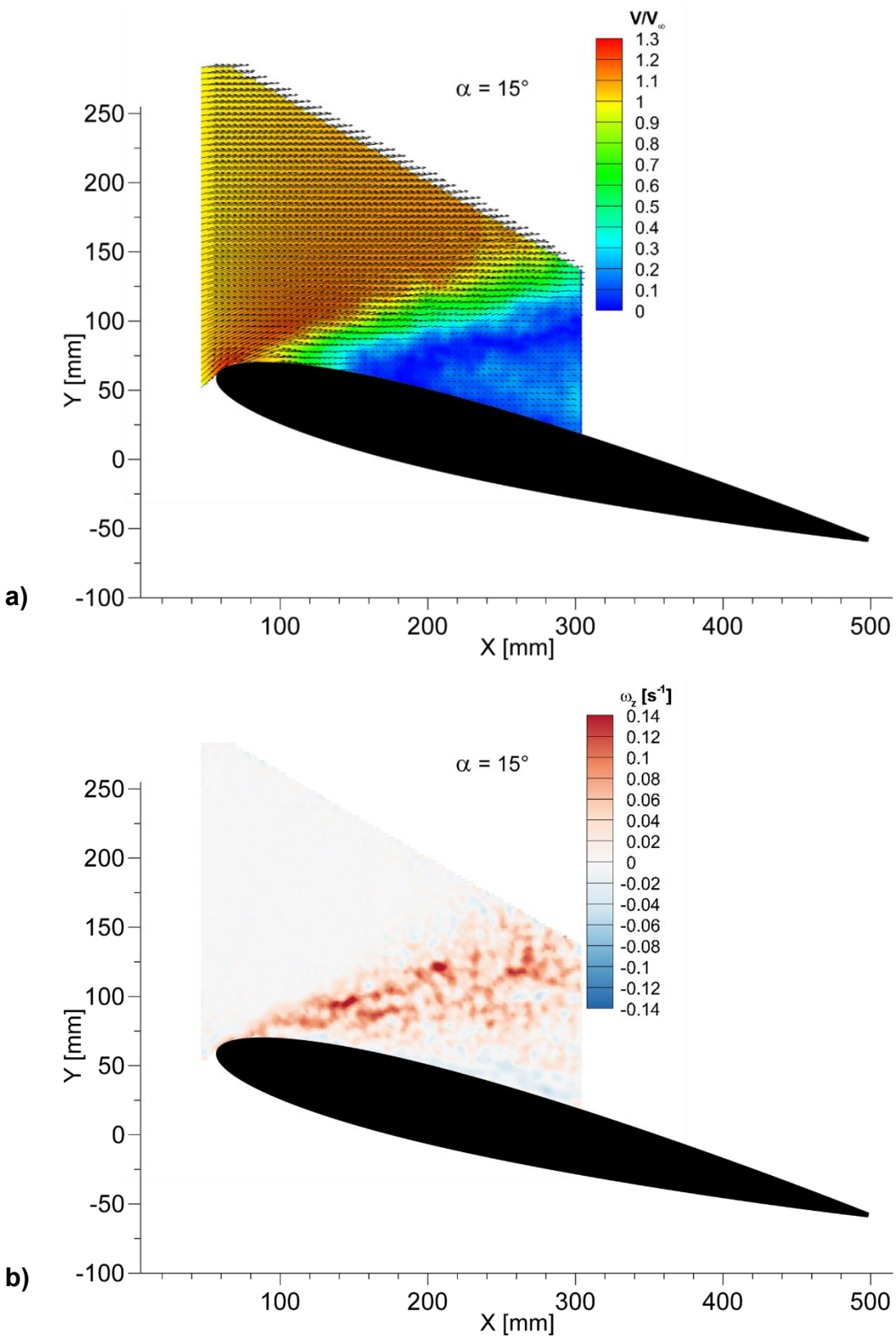

Fig. 3.17 Conditionally averaged time-resolved PIV velocity data a) and vorticity data b) for α = 15°, during upstroke phase angle $\Phi = \pi$.

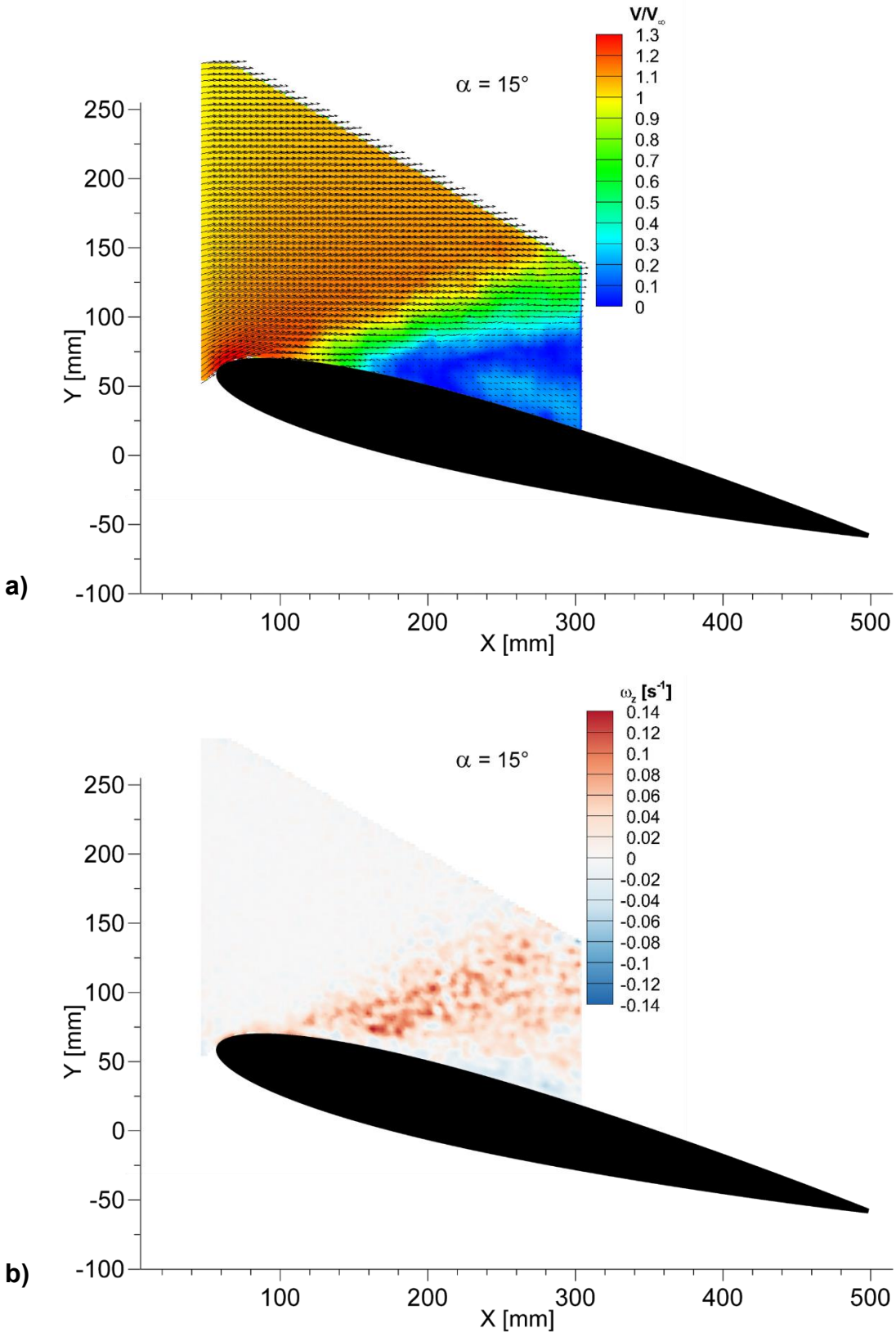

Fig. 3.18 Conditionally averaged time-resolved PIV velocity data a) and vorticity data b) for α = 15°, during upstroke phase angle $\Phi = 3\pi/2$.

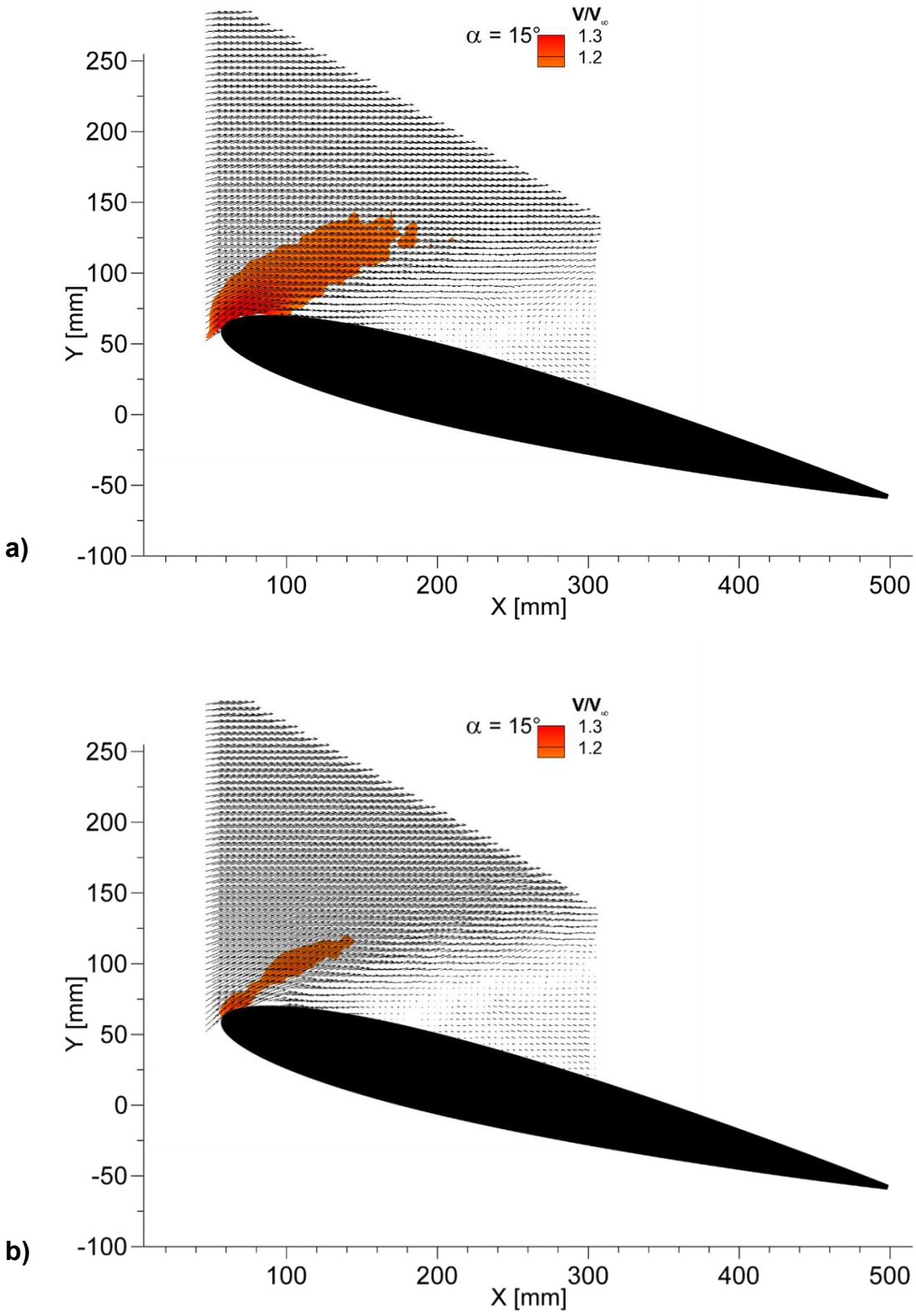

Fig. 3.19 Comparison of the regions with velocity above 1.15V_∞ (46 m/s) for $\Phi = 0$ a) and $\Phi = \pi$ b) for $\alpha = 15°$ during upstroke. Conditionally averaged data were used.

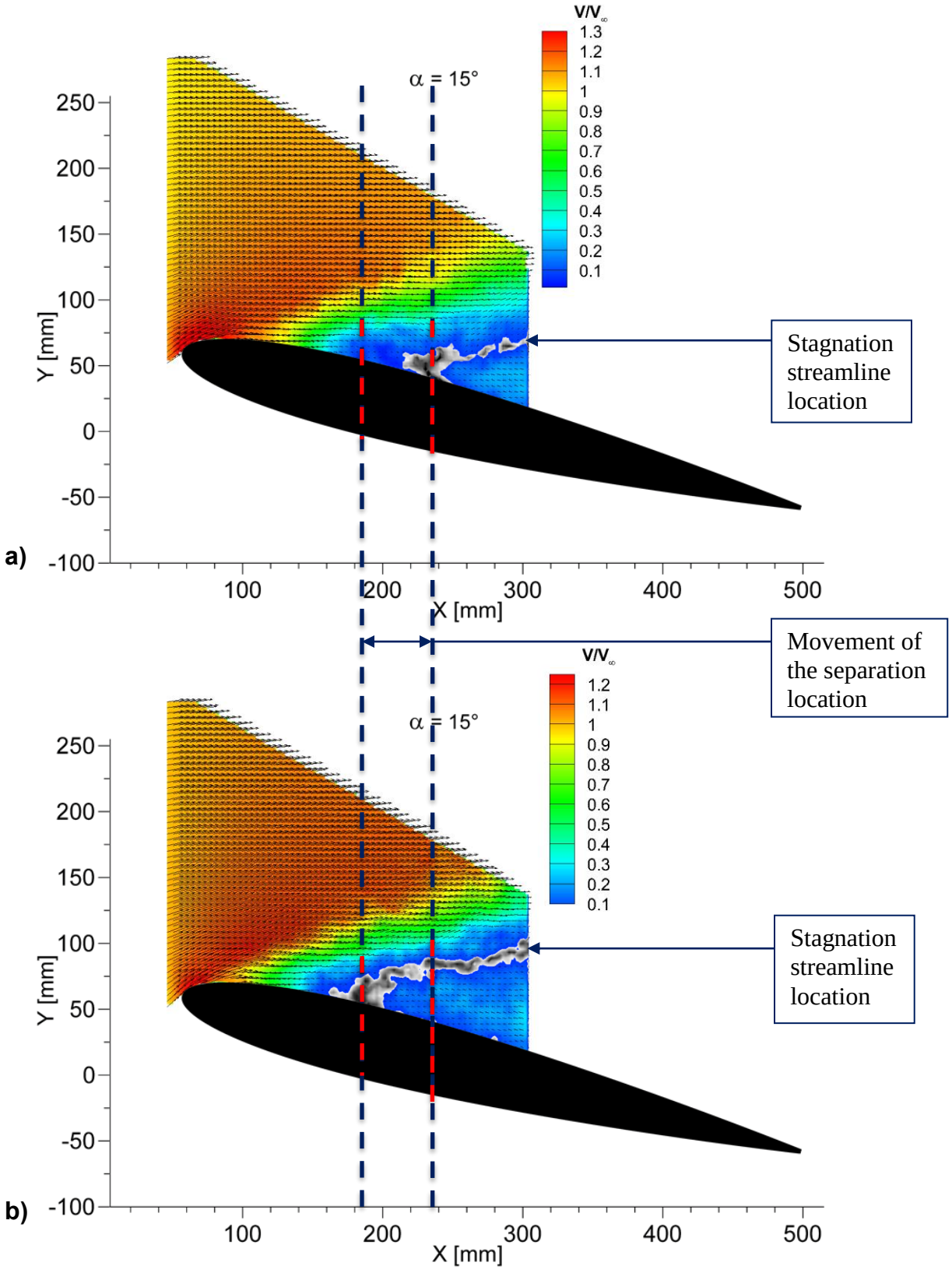

Fig. 3.20 Boundary layer separation locations for $\Phi = 0$ a) and $\Phi = \pi$ b) for the upstroke at $\alpha = 15°$. The gray regions indicate zero velocity, demarcating regions of reversed flow.

Chapter 4

Summary and Conclusions

An experimental study was conducted to understand the unsteady flow field associated with static stall hysteresis. Experiments were conducted on an NACA 0012 airfoil model at a chord-based Reynolds number of Re = 1×10^6. Hysteresis effects were observed in the airfoil C_l, C_m and C_d beyond the static stall angle of attack. This difference was attributed to markedly different pressure distributions across the leading-edge region of the airfoil. For a fixed post-stall angle of attack, the upstroke was associated with a distinct suction peak, followed by a constant-pressure plateau. Conversely, the downstroke was associated with a constant pressure across the entire upper surface, representative of a massive separation. A concentrated region of unsteadiness in surface $C_{p,SD}$ was prominently observed across the leading-edge region for the upstroke branch, while the massively separated flow for the downstroke branch exhibited clear elevated levels of flow field unsteadiness across the entire upper surface.

A Fourier analysis of the unsteady surface pressures revealed that the leading-edge unsteady flow of the upstroke branch was associated with a low-frequency oscillation near St = 0.02. Conversely, for the downstroke branch a bluff-body shedding frequency was observed across the mid- and aft-chord regions of the airfoil, with St = 0.14. The amplitude of the flow field unsteadiness was observed to be higher at the lower angles of attack during both the upstroke and downstroke branches, with the exception of the upstroke at α = 14°, as much of the flow was still

attached under these conditions. Generally, the overall unsteadiness exhibited during the downstroke was greater than that of the upstroke, which was consistent with prior studies in static stall hysteresis. Consistent with the observations from the spectral analysis of the flow, the variation of lift coefficient with time for the upstroke branch of the hysteresis loop at $\alpha = 15°$ showed the presence of the previously observed low-frequency. In contrast with the upstroke, the downstroke case revealed a more chaotic variation of lift coefficient with time which was not characterized by a periodic oscillation across a single representative frequency band. This result implied that the observed low-frequency oscillations in the pressure data had a direct effect on lift, and thus hysteresis.

Time-resolved PIV was used to identify off-body characteristics of the flow field unsteadiness observed in the surface C_p measurements. Sequential PIV velocity field data revealed a distinct movement of the separation location and surging of the flow velocity across the leading edge for the upstroke branch at a fixed angle of attack. This low-frequency oscillation represented a large-scale, global modulation of the flow velocity across the airfoil. Conversely, oscillations in the flow field were observed due to bluff-body shedding for the downstroke branch, though these variations provided little movement of the separation location and were contained to localized regions near the shear layer.

Appendix A

Uncertainty Analysis

The experimental results from this investigation were associated with certain uncertainties which are presented in this chapter. Analyzing the uncertainties of acquired measurements is important in assessing the significance of the scatter associated with experimental results over multiple trials[37] and thus provide a more robust interpretation of the experimental results. As described by Kline and McClintock[38] and Airy[39], the uncertainty in a measurement is the "possible value that an error may have". Two sources of error – bias and precision errors – that contribute to the uncertainties were evaluated in this study. Bias errors are typically associated with uncertainties in the measurement capabilities of the equipment or accuracy of the calibration. These errors are also referred to as "fixed" errors because they are accompanied with a consistent and repeatable offset. Precision errors, on the other hand, are classified as being "random", since they behave randomly with zero mean. The sum of these two sources of error provided the best estimate of the measurement error.

The precision or uncertainty (U_X) associated with a set of N observations of the variable (X) having a mean ($X_{(N)}$) can be calculated using,[37]

$$U_X = \frac{tS_{(N)}}{\sqrt{N}} \tag{A.1}$$

where $S_{(N)}$ is the standard deviation of the set of N observations used to calculate the mean value $X_{(N)}$, and t is the Student's t statistic determined by the desired confidence interval and the number of samples N. The variable (X) is assumed to follow a Gaussian distribution.

The reduced variable of an experiment (R) that is determined using several independently measured variables (x_i) is represented by,

$$R = R(x_1, x_2, ..., x_n) \tag{A.2}$$

Since the separate measurements were acquired from different measurements, it is natural to assume that the uncertainties of each measured variable were independent from each other. Therefore, the "bias" or "fixed" uncertainty (U_R) associated with the result is then calculated by taking the square root of the sum of the squares of the corresponding uncertainty components produced by each variable,[38]

$$U_R = \sqrt{\left(\frac{\partial R}{\partial x_1} U_{x_1}\right)^2 + \left(\frac{\partial R}{\partial x_2} U_{x_2}\right)^2 + ... + \left(\frac{\partial R}{\partial x_n} U_{x_n}\right)^2} \tag{A.3}$$

This method was used to calculate the "bias" uncertainties associated with the flow conditions, pressure and performance coefficients. A derivation of the equations used for these reduced variables was outlined in Section A.1. The resulting "precision" uncertainty associated with the PIV measurements were also calculated using the methods described above and are discussed in Section A.2 .

A.1 Uncertainty in Performance Measurements

A.1.1 Uncertainty in Flow Conditions

The uncertainties in the flow conditions for the experiments in this study were calculated using the equations in this section. Uncertainty estimates for the freestream dynamic pressure, atmospheric density, dynamic viscosity, freestream velocity, and Reynolds number are presented in Table A.1.

The freestream dynamic pressure calculation (Eq. 2.9) involved the contraction ratio across the tunnel inlet. Since the contraction ratio was constant and the uncertainty in the area ratio was assumed to be very low, the uncertainty in the contraction ratio was assumed to be negligible.

Therefore, the pressure difference was the only factor that contributed to the uncertainty of the freestream dynamic pressure. Using Eq. A.3, the uncertainty in the dynamic pressure was calculated to be,

$$U_{q_\infty} = \sqrt{\left(\frac{\partial q_\infty}{\partial \left(P_{ss} - P_{ts} \right)} U_{(P_{ss}-P_{ts})} \right)^2} \tag{A.4}$$

The uncertainty in the measured pressure difference between the settling section and the test section was also assumed constant. Thus, Eq. A.4 can be rewritten as,

$$U_{q_\infty} = \frac{\partial q_\infty}{\partial \left(P_{ss} - P_{ts} \right)} U_{(P_{ss}-P_{ts})} = \frac{1}{1 - \left(\frac{A_{ts}}{A_{ss}} \right)^2} U_{(P_{ss}-P_{ts})} \tag{A.5}$$

The atmospheric density was calculated using the ideal gas law. Since, the gas constant of air, R, is a constant, the only contributing quantities to the uncertainty of ρ_{amb} were P_{amb} and T_{amb}. The uncertainty was calculated using,

$$U_{\rho_{amb}} = \sqrt{\left(\frac{\partial \rho_{amb}}{\partial P_{amb}} U_{P_{amb}} \right)^2 + \left(\frac{\partial \rho_{amb}}{\partial T_{amb}} U_{T_{amb}} \right)^2} \tag{A.6}$$

where

$$\frac{\partial \rho_{amb}}{\partial P_{amb}} = \frac{1}{R T_{amb}} \tag{A.7}$$

$$\frac{\partial \rho_{amb}}{\partial T_{amb}} = -\frac{P_{amb}}{R T_{amb}^2} \tag{A.8}$$

The dynamic viscosity was calculated using Sutherland's formula,

$$\mu_{amb} = \mu_0 \frac{T_0 + C}{T_{amb} + C} \left(\frac{T_{amb}}{T_0} \right)^{3/2} \tag{A.9}$$

with known constants $\mu_0 = 3.58404 \times 10^{-7}$ lb-s/ft^2, $T_0 = 491.6$ R, and $C = 199.8$ R. Therefore, the only contributing factor to the uncertainty of the dynamic viscosity was the ambient temperature. The uncertainty was calculated using,

$$U_{\mu_{amb}} = \sqrt{\left(\frac{\partial \mu_{amb}}{\partial T_{amb}} U_{T_{amb}}\right)^2} \tag{A.10}$$

Since the freestream velocity can be expressed in terms of the dynamic pressure using,

$$U_\infty = \sqrt{\frac{2q_\infty}{\rho_{amb}}} \tag{A.11}$$

The uncertainty in the freestream velocity was calculated using the already calculated $U_{\rho_{amb}}$ and U_{q_∞},

$$U_{U_\infty} = \sqrt{\left(\frac{\partial U_\infty}{\partial q_\infty} U_{q_\infty}\right)^2 + \left(\frac{\partial U_\infty}{\partial \rho_{amb}} U_{\rho_{amb}}\right)^2} \tag{A.12}$$

where

$$\frac{\partial U_\infty}{\partial q_\infty} = \frac{1}{\sqrt{2q_\infty \rho_{amb}}} \tag{A.13}$$

$$\frac{\partial U_\infty}{\partial \rho_{amb}} = -\frac{1}{\rho_{amb}} \frac{q_\infty}{\sqrt{2\rho_{amb}}} \tag{A.14}$$

The uncertainty of the Reynolds number had contributions from the freestream velocity, dynamic viscosity, density, and chord length. The machining precision for the aluminum sections of the model was assumed to be 0.005 inches, based on standard precision of computer numerical control fabrication machines. Therefore, the uncertainty in the Reynolds number was determined using,

$$U_{\mathrm{Re}} = \sqrt{\left(\frac{\partial \mathrm{Re}}{\partial U_\infty} U_{U_\infty}\right)^2 + \left(\frac{\partial \mathrm{Re}}{\partial \rho_{amb}} U_{\rho_{amb}}\right)^2 + \left(\frac{\partial \mathrm{Re}}{\partial \mu_{amb}} U_{\mu_{amb}}\right)^2 + \left(\frac{\partial \mathrm{Re}}{\partial c} U_c\right)^2} \tag{A.15}$$

where

$$\frac{\partial \mathrm{Re}}{\partial U_\infty} = \frac{\rho_{amb} c}{\mu_{amb}} \tag{A.16}$$

$$\frac{\partial \mathrm{Re}}{\partial \rho_{amb}} = \frac{U_\infty c}{\mu_{amb}} \tag{A.17}$$

$$\frac{\partial \mathrm{Re}}{\partial \mu_{amb}} = -\frac{\rho_{amb} U_\infty c}{\mu_{amb}^2} \tag{A.18}$$

$$\frac{\partial \mathrm{Re}}{\partial c} = \frac{\rho_{amb} U_\infty}{\mu_{amb}} \tag{A.19}$$

A.1.2 Uncertainty in Pressure and Performance Coefficients

The uncertainties in the pressure and performance coefficient results, i.e., C_p, C_l, C_m and C_d, were calculated using the equations in this section. Uncertainty estimates for the reduced performance coefficients are presented in Table A.2.

The unsteady pressure measurements that were acquired in this study were used to calculate the time averaged performance coefficients, C_l and C_m. The uncertainty of the Kulite unsteady pressure transducers, which was quoted by the manufacturer to be within ±0.1% of the full-scale ±5 psid range, was used in evaluating these uncertainties. Since the C_p results were obtained using measurements of the pressure difference ($P_{s,i} - P_{ts}$) and the calculated dynamic pressure (Eq. 2.10), the uncertainty in the C_p could be estimated using,

$$U_{C_p} = \sqrt{\left(\frac{\partial C_p}{\partial \left(P_{s,i} - P_{ts} \right)} U_{(P_{s,i} - P_{ts})} \right)^2 + \left(\frac{\partial C_p}{\partial q_\infty} U_{q_\infty} \right)^2} \tag{A.20}$$

where

$$\frac{\partial C_p}{\partial \left(P_{s,i} - P_{ts} \right)} = \frac{1}{q_\infty} \tag{A.21}$$

$$\frac{\partial C_p}{\partial q_\infty} = -\frac{P_{s,i} - P_{ts}}{q_\infty^2} \tag{A.22}$$

The uncertainty of the lift coefficient (Eq. 2.20) can be estimated using,

$$U_{C_l} = \sqrt{\left(\frac{\partial C_l}{\partial L'} U_{L'}\right)^2 + \left(\frac{\partial C_l}{\partial q_\infty} U_{q_\infty}\right)^2 + \left(\frac{\partial C_l}{\partial c} U_c\right)^2} \tag{A.23}$$

where

$$\frac{\partial C_l}{\partial L'} = \frac{1}{q_\infty c} \tag{A.24}$$

$$\frac{\partial C_l}{\partial q_\infty} = -\frac{L'}{q_\infty^2 c} \tag{A.25}$$

$$\frac{\partial C_l}{\partial c} = -\frac{L'}{q_\infty c^2} \tag{A.26}$$

In order to determine the uncertainty in the lift coefficient, the uncertainty in the sectional lift, $U_{L'}$, needed to be calculated first. Therefore, the sectional lift uncertainty was first divided into its normal and axial contributions. The expressions for the sectional normal, F_N', and axial, F_A', forces were calculated using,

$$F_{N'} = \frac{1}{2}\left[P_1(x_2 - x_1) + \sum_{i=2}^{n-1} P_i(x_{i+1} - x_{i-1}) + P_n(x_n - x_{n-1})\right] \tag{A.27}$$

and

$$F_{A'} = \frac{1}{2}\left[P_1(y_2 - y_1) + \sum_{i=2}^{n-1} P_i(y_{i+1} - y_{i-1}) + P_n(y_n - y_{n-1})\right] \tag{A.28}$$

Combining the above equations with Eq. 2.17, the sectional lift expression was derived.

$$\begin{aligned} L' = {} & \frac{1}{2}\cos\alpha\left[P_1(x_2 - x_1) + \sum_{i=2}^{n-1} P_i(x_{i+1} - x_{i-1}) + P_n(x_n - x_{n-1})\right] \\ & -\frac{1}{2}\sin\alpha\left[P_1(y_2 - y_1) + \sum_{i=2}^{n-1} P_i(y_{i+1} - y_{i-1}) + P_n(y_n - y_{n-1})\right] \end{aligned} \tag{A.29}$$

The uncertainty in the resulting sectional lift could be then estimated using,

$$U_{L'} = \sqrt{\left(\frac{\partial L'}{\partial \alpha} U_\alpha\right)^2 + \sum_{i=1}^{n}\left(\frac{\partial L'}{\partial P_i} U_{P_i}\right)^2} \tag{A.30}$$

where

$$\begin{aligned}\frac{\partial L'}{\partial \alpha} = &-\frac{1}{2}\sin\alpha\left[P_1(x_2 - x_1) + \sum_{i=2}^{n-1} P_i(x_{i+1} - x_{i-1}) + P_n(x_n - x_{n-1})\right] \\ &-\frac{1}{2}\cos\alpha\left[P_1(y_2 - y_1) + \sum_{i=2}^{n-1} P_i(y_{i+1} - y_{i-1}) + P_n(y_n - y_{n-1})\right]\end{aligned} \tag{A.31}$$

$$\begin{aligned}\frac{\partial L'}{\partial P_1} &= \frac{1}{2}\cos\alpha(x_2 - x_1) + \frac{1}{2}\sin\alpha(y_1 - y_2) \\ \frac{\partial L'}{\partial P_i} &= \frac{1}{2}\cos\alpha(x_{i+1} - x_{i-1}) + \frac{1}{2}\sin\alpha(y_{i-1} - y_{i+1}); \quad i = 2, n-1 \\ \frac{\partial L'}{\partial P_n} &= \frac{1}{2}\cos\alpha(x_N - x_{N-1}) + \frac{1}{2}\sin\alpha(y_{n-1} - y_n)\end{aligned} \tag{A.32}$$

Similarly, the Kulite pressure transducers used to determine the quarter-chord pitching moment coefficient. As a result, the uncertainty of the quarter-chord pitching moment coefficient (Eq. 2.21) was estimated using,

$$U_{C_m} = \sqrt{\left(\frac{\partial C_m}{\partial M'_{c/4}} U_{M'_{c/4}}\right)^2 + \left(\frac{\partial C_m}{\partial q_\infty} U_{q_\infty}\right)^2 + \left(\frac{\partial C_m}{\partial c} U_c\right)^2} \tag{A.33}$$

where

$$\frac{\partial C_m}{\partial M'_{c/4}} = \frac{1}{q_\infty c^2} \tag{A.34}$$

$$\frac{\partial C_m}{\partial q_\infty} = -\frac{M'_{c/4}}{q_\infty^2 c^2} \tag{A.35}$$

$$\frac{\partial C_m}{\partial c} = -\frac{2M'_{c/4}}{q_\infty c^3} \tag{A.36}$$

Using Eqs. 2.18 and 2.19 along with the expanded forms of the axial and normal forces derived in Eqs. A.27 and A.28, the expanded form of the sectional quarter-chord pitching moment was expressed as,

$$M'_{c/4} = \frac{1}{4}\left[\begin{array}{l} P_1\left(x_1^2 - x_2^2 - 2x_1x_{c/4} + 2x_2x_{c/4} + y_1^2 - y_2^2\right) \\ + \sum_{i=2}^{n-1}\left[P_i\left(x_{i-1}^2 - x_{i+1}^2 - 2x_{i-1}x_{c/4} + 2x_{i+1}x_{c/4} + y_{i-1}^2 - y_{i+1}^2\right)\right] \\ + P_n\left(x_{n-1}^2 - x_n^2 - 2x_{n-1}x_{c/4} + 2x_nx_{c/4} + y_{n-1}^2 - y_n^2\right) \end{array}\right] \tag{A.37}$$

The uncertainty of the sectional quarter-chord pitching moment was then estimated using,

$$U_{M'_{c/4}} = \sqrt{\sum_{i=1}^{n}\left(\frac{\partial M'_{c/4}}{\partial P_i}U_{P_i}\right)^2} \tag{A.38}$$

where

$$\begin{aligned} \frac{\partial M'_{c/4}}{\partial P_1} &= \frac{1}{4}\left(x_1^2 - x_2^2 - 2x_1x_{c/4} + 2x_2x_{c/4} + y_1^2 - y_2^2\right) \\ \frac{\partial M'_{c/4}}{\partial P_i} &= \frac{1}{4}\left(x_{i-1}^2 - x_{i+1}^2 - 2x_{i-1}x_{c/4} + 2x_{i+1}x_{c/4} + y_{i-1}^2 - y_{i+1}^2\right); \quad i = 2, n-1 \\ \frac{\partial M'_{c/4}}{\partial P_n} &= \frac{1}{4}\left(x_{n-1}^2 - x_n^2 - 2x_{n-1}x_{c/4} + 2x_nx_{c/4} + y_{n-1}^2 - y_n^2\right) \end{aligned} \tag{A.39}$$

Unlike the quarter-chord pitching moment and lift coefficients, the drag coefficient of the airfoil was determined using the wake survey system. Therefore, the uncertainties associated with the ESP modules of the PSI system, that was used to acquire the wake data, were examined. The ESP module uncertainty was provided by the manufacturer to be 0.10% of the full-scale range for the ±0.35 psid module. Using the uncertainties of these PSI system measurements, the uncertainties of the wake survey results could be evaluated.

By combining Eq. 2.29 and Eq. 2.30, the expanded form of the drag coefficient expression becomes,

$$\begin{aligned} C_d = \frac{1}{q_\infty c}\sum_{i=1}^{n_{rake}-1}\Bigg(&\sqrt{q_\infty^2 - q_\infty\left(P_{0,\infty} - P_{0,w_i}\right)} + \sqrt{q_\infty^2 - q_\infty\left(P_{0,\infty} - P_{0,w_{i+1}}\right)} \\ &- 2q_\infty + 2P_{0,\infty} - P_{0,w_i} - P_{0,w_{i+1}}\Bigg)\left(y_i - y_{i+1}\right) \end{aligned} \tag{A.40}$$

Both $P_{0,\infty}$ and $P_{0,w}$ were referenced to atmospheric pressure. Therefore, the only contribution to the uncertainty in the drag coefficient was due to uncertainty in the measurements of the dynamic pressure, the airfoil chord, the wake pressures and the freestream total pressure. Thus, the uncertainty in the drag coefficient can be expressed using,

$$U_{C_d} = \sqrt{\left(\frac{\partial C_d}{\partial q_\infty}U_{q_\infty}\right)^2 + \left(\frac{\partial C_d}{\partial c}U_c\right)^2 + \left(\frac{\partial C_d}{\partial P_{0,\infty}}U_{P_{0,\infty}}\right)^2 + \sum_{i=1}^{n_{rake}-1}\left(\frac{\partial C_d}{\partial P_{0,w}}U_{P_{0,w}}\right)^2} \tag{A.41}$$

where

$$\begin{aligned}\frac{\partial C_d}{\partial q_\infty} = -\frac{1}{q_\infty^2 c}\sum_{i=1}^{n_{rake}-1}\Bigg(&\sqrt{q_\infty^2 - q_\infty\left(P_{0,\infty} - P_{0,w_i}\right)} + \sqrt{q_\infty^2 - q_\infty\left(P_{0,\infty} - P_{0,w_{i+1}}\right)} \\ &- 2q_\infty + 2P_{0,\infty} - P_{0,w_i} - P_{0,w_{i+1}}\Bigg)\left(y_i - y_{i+1}\right) + \frac{1}{q_\infty c}\sum_{i=1}^{n_{rake}-1}\Bigg[\frac{2q_\infty - \left(P_{0,\infty} - P_{0,w_i}\right)}{2\sqrt{q_\infty^2 - q_\infty\left(P_{0,\infty} - P_{0,w_i}\right)}} \\ &+ \frac{2q_\infty - \left(P_{0,\infty} - P_{0,w_{i+1}}\right)}{2\sqrt{q_\infty^2 - q_\infty\left(P_{0,\infty} - P_{0,w_{i+1}}\right)}} - 2\Bigg]\left(y_i - y_{i+1}\right)\end{aligned} \tag{A.42}$$

$$\begin{aligned}\frac{\partial C_d}{\partial c} = -\frac{1}{q_\infty c^2}\sum_{i=1}^{n_{rake}-1}\Bigg(&\sqrt{q_\infty^2 - q_\infty\left(P_{0,\infty} - P_{0,w_i}\right)} + \sqrt{q_\infty^2 - q_\infty\left(P_{0,\infty} - P_{0,w_{i+1}}\right)} \\ &- 2q_\infty + 2P_{0,\infty} - P_{0,w_i} - P_{0,w_{i+1}}\Bigg)\left(y_i - y_{i+1}\right)\end{aligned} \tag{A.43}$$

$$\begin{aligned}\frac{\partial C_d}{\partial P_{0,\infty}} = \frac{1}{q_\infty c}\sum_{i=1}^{n_{rake}-1}\Bigg(&2 - \frac{q_\infty}{2\sqrt{q_\infty^2 - q_\infty\left(P_{0,\infty} - P_{0,w_i}\right)}} \\ &- \frac{q_\infty}{2\sqrt{q_\infty^2 - q_\infty\left(P_{0,\infty} - P_{0,w_{i+1}}\right)}}\Bigg)\left(y_i - y_{i+1}\right)\end{aligned} \tag{A.44}$$

$$\frac{\partial C_d}{\partial P_{0,w_i}} = \frac{1}{q_\infty c}\left(\frac{q_\infty}{2\sqrt{q_\infty^2 - q_\infty\left(P_{0,\infty} - P_{0,w_i}\right)}} - 1\right)\left(y_i - y_{i+1}\right) \tag{A.45}$$

A1.3 Uncertainty in Strouhal Number

The uncertainty of the Strouhal number in Eq. 2.31 was evaluated. The resulting expression for the Strouhal number uncertainty calculation was,

$$U_{St} = \sqrt{\left(\frac{\partial St_h}{\partial U_\infty} U_{U_\infty}\right)^2 + \left(\frac{\partial St_h}{\partial f} U_f\right)^2 + \left(\frac{\partial St_h}{\partial c} U_c\right)^2 + \left(\frac{\partial St_h}{\partial \alpha} U_\alpha\right)^2} \tag{A.46}$$

where

$$\frac{\partial St}{\partial U_\infty} = -\frac{fc\sin\alpha}{U_\infty^2} \tag{A.47}$$

$$\frac{\partial St}{\partial f} = \frac{c\sin\alpha}{U_\infty} \tag{A.48}$$

$$\frac{\partial St}{\partial c} = \frac{f\sin\alpha}{U_\infty} \tag{A.49}$$

$$\frac{\partial St}{\partial \alpha} = \frac{fc\cos\alpha}{U_\infty} \tag{A.50}$$

Example uncertainty values are presented in Table A.3.

Table A.1 Example uncertainties for test conditions of NACA 0012 airfoil model at $Re_c = 1 \times 10^6$ and $\alpha = 15°$ on the upstroke branch of the hysteresis loop.

Parameter	Reference Value	Absolute Uncertainty	Relative Uncertainty (%)
c	18 in	±0.005 in	±0.0278
α	15.038°	±0.02°	±1.33
$q_{\infty,Setra}$	0.09577 psi	±0.000771 psi	±0.8026
P_{amb}	14.38 psi	±0.008 psi	±0.0556
T_{amb}	528.78 °R	±1.8 °R	±0.3404
ρ_{amb}	2.283×10^{-3} slugs/ft^3	$\pm 7.771 \times 10^{-6}$ slugs/ft^3	±0.3404
μ_{amb}	3.794×10^{-7} lb-s/ft^2	$\pm 1.270 \times 10^{-9}$ lb-s/ft^2	±0.3342
U_∞	109.9 ft/sec	±0.1871 ft/sec	±0.1702
Re_c	992124	±5033	±0.5073

Table A.2 Example uncertainties for airfoil pressure and performance coefficients of NACA 0012 airfoil model at $Re_c = 1 \times 10^6$ and $\alpha = 15°$ on the upstroke branch of the hysteresis loop.

Parameter	Reference Value	Absolute Uncertainty	Relative Uncertainty (%)
$C_{p,i}$ ($x/c = 0.44$)	-2.8218	± 0.056935	± 2.0177
C_l	0.8583	± 0.023424	± 2.7290
C_m	-0.0633	± 0.008767	± 13.860
C_d	0.4591	± 0.002393	± 0.5212

Table A.3 Example uncertainties for the Strouhal number of unsteady modes present in the flow field about the NACA 0012 airfoil model at $Re_c = 1 \times 10^6$ and $\alpha = 15°$ on the upstroke branch of the hysteresis loop.

Parameter	Reference Value	Absolute Uncertainty	Relative Uncertainty (%)
$St_{Low\text{-}Freq.}$	0.02	± 0.001034	± 5.1689
$St_{shedding}$	0.14	± 0.002033	± 1.4521

A.2 PIV Uncertainty Analysis

The methods described by Lazar et al.[40] were used to estimate the uncertainties of the PIV results. Four sources of uncertainty are considered by these methods: equipment uncertainty, uncertainty in particle dynamics, sampling, and processing uncertainties. Uncertainties associated with the calibration scale, image distortion, jitter in the laser pulse timing and the accuracy of the delay generator used to control the timings of the laser and camera system were accounted for by the equipment uncertainty (U_E).

The out-of-plane motion of the seed particles is accounts for by the uncertainty in the particle dynamics (U_L). The uncertainty in particle dynamics also includes the particle lag that results from Stokes drag force. A lag in the motion of the seed particles with respect to the local flow velocity is observed particularly in regions with large velocity gradients. This particle lag velocity can be calculated as the difference between the local velocity of the fluid, u_f, and the velocity of the seed particle, u_p, using,

$$u_f - u_p = \frac{1}{18}\frac{\rho_p d_p^2}{\mu_f}\left(\frac{\partial u_p}{\partial x_p}\frac{\partial x_p}{\partial t} + \frac{\partial u_p}{\partial y_p}\frac{\partial y_p}{\partial t}\right) \tag{A.60}$$

where ρ_p is the density of the seed particles, d_p is the particle diameter, μ_f is the fluid viscosity, and x_p and y_p represent the local coordinate directions.

The sampling uncertainty (U_S) was used to estimate the scatter associated with the instantaneous velocity vector fields used to calculate the time-averaged PIV results at a given confidence interval. The instantaneous velocity vector fields collected during this investigation were assumed to be statistically independent and to follow a Gaussian distribution. Therefore, the sampling uncertainty was evaluated following a process identical to the precision uncertainty process discussed at the beginning of this appendix. Thus, Eq. A.61 is used to calculate the scatter in the flow velocity (σ_V) evaluated at a certain confidence level around the sample mean $V_{(N)}$ for a set of N samples with a standard deviation $S_{(N)}$.

$$\sigma_V = V_{(N)} \pm \frac{tS_{(N)}}{\sqrt{N}} \tag{A.61}$$

The accuracy and reliability of the digital processing techniques used to correlate the raw particle image pairs into meaningful vector fields were assessed using the processing uncertainty (U_P). The processing uncertainty addressed the image pre- and post-processing algorithms, filtering procedures and cross-correlation methods. In order to evaluate these uncertainties, a synthetic PIV script written in MATLAB was used to generate synthetic image pairs for the studied flow field. The resulting synthetic image pairs were processed using the processing steps used to obtain the experimentally-acquired particle image pairs. The vector fields generated by the synthetic image pairs were compared against the experimental particle image pairs in order to establish the processing uncertainty.

The total PIV uncertainty (U_T) can be calculated through the method used to calculate the performance uncertainties. The total PIV uncertainty (Eq. A.62) was calculated by taking the square root of the sum of the squares of the individual uncertainties that were obtained in this section.

$$U_T = \sqrt{U_E^2 + U_L^2 + U_S^2 + U_P^2} \tag{A.62}$$

The uncertainties associated with PIV acquisition for the flow field about the NACA 0012 airfoil at $Re_c = 1 \times 10^6$ during the upstroke branch of the hysteresis loop at $\alpha = 15°$ were calculated at a 95% confidence level. The uncertainties in the streamwise and transverse velocity directions were

normalized by the freestream velocity and presented in Fig. A.1. The mean uncertainties of the velocity fields in the *x*- and *y*-directions were calculated to be 0.24% and 0.53% respectively.

Appendix A Figures

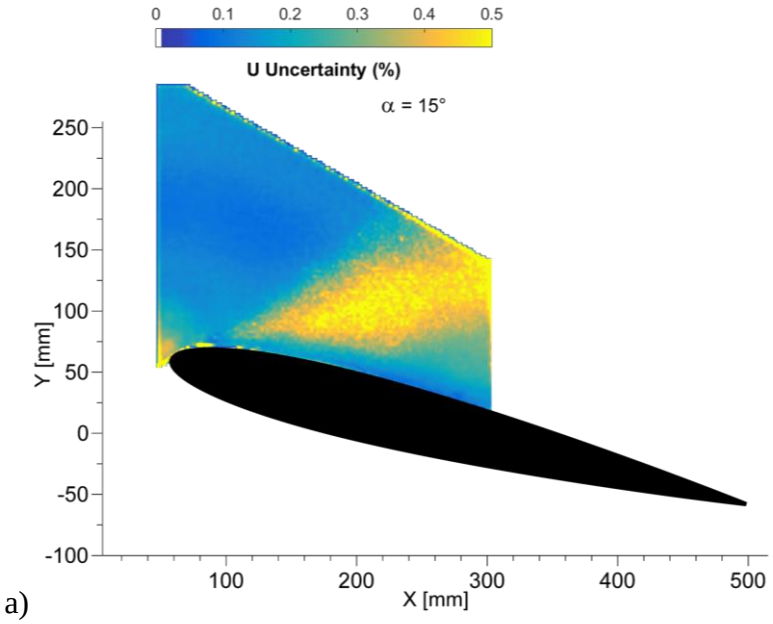

a)

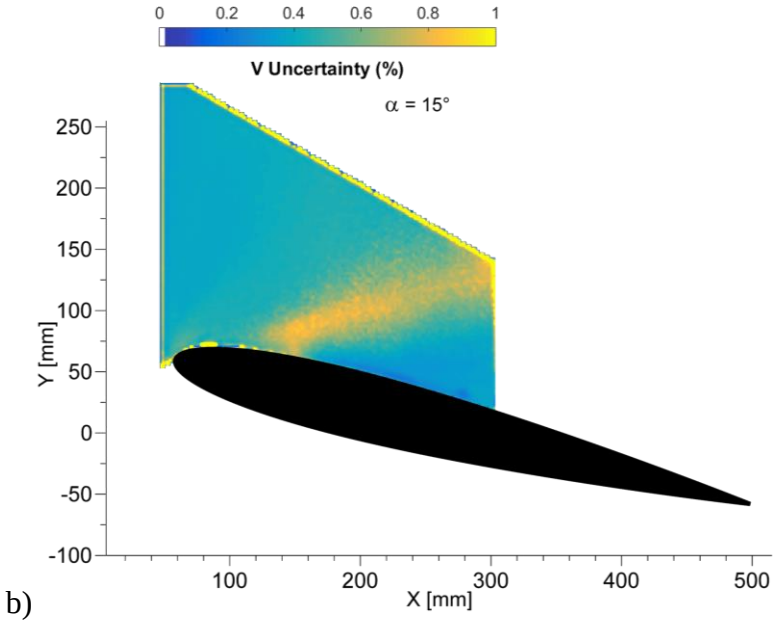

b)

Fig. A.1 PIV Uncertainty for freestream normalized a) streamwise and b) transverse velocity components at $Re_c = 1 \times 10^6$ and $\alpha = 15°$.

References

[1] Biber, K., and G. W. Zumwalt, "Hysteresis Effect on Wind Tunnel Measurements of a Two-Element Airfoil", *AIAA Journal*, Vol. 31, No. 2, 1993, pp. 326-330.

[2] Traub, L., "Semi-Empirical Prediction of Airfoil Hysteresis", *Aerospace*, Vol, 3, No. 9, 2016.

[3] Pohlen, L. J., and Mueller, T. J., "Boundary Layer Characteristics of the Miley Airfoil at Low Reynolds Numbers", *Journal of Aircraft*, Vol. 21, No.9, 1984, pp658-664.

[4] Mueller, T. J., "The influence of laminar separation and transition on low Reynolds number airfoil hysteresis", *Journal of Aircraft*, Vol. 22, No. 9, 1985, pp. 763-770.

[5] Yang, Z., Igarashi, H., "An Experimental Investigation on Aerodynamic Hysteresis of a Low-Reynolds Number Airfoil", AIAA Paper 2008-0315, 2008.

[6] Hoffmann, J. A., "Effects of freestream turbulence on the performance characteristics of an airfoil," *AIAA Journal*, Vol. 29, No. 9, 1991, pp. 1353-1354.

[7] Mittal, S. and Saxena P., "Prediction of hysteresis associated with static stall of an airfoil", *AIAA Journal*, Vol. 38, No. 5, 2002, pp. 933-935.

[8] Zaman, K. B. M. Q., McKinzie, D. J., and Rumsey, C. L., "A Natural Low-Frequency Oscillation of the Flow over an Airfoil Near Stalling Conditions," *Journal of Fluid Mechanics*, Vol. 202, 1989, pp. 403–442.

[9] Yon, S. A., and Katz, J., "Study of the Unsteady Flow Features on a Stalled Wing," *AIAA Journal*, Vol. 36, No. 3, 1998, pp. 305–312.

[10] Huang, R. F.,Wu, J. Y., Jeng, J. H., and Chen, R. C., "Surface Flow and Vortex Shedding of an Impulsively Started Wing," *Journal of Fluid Mechanics*, Vol. 441, 2001, pp. 265–292.

[11] Morse, D. R., and Liburdy, J. A., "Vortex Dynamics and Shedding of a Low Aspect Ratio, Flat Wing at Low Reynolds Numbers and High Angles of Attack," *Journal of Fluids Engineering*, Vol. 131, No. 5, 2009, Paper 051202.

[12] Swalwell, K.E., Sheridan, J., and Melbourne, W.H., "Frequency Analysis of Surface Pressures on an Airfoil After Stall," AIAA Paper 2003-3416, 2003.

[13] Huang, R. F., and Lin, C. L., "Vortex Shedding and Shear-Layer Instability ofWing at Low-Reynolds Numbers," *AIAA Journal*, Vol. 33, No. 8, 1995, pp. 1398–1403.

[14] Yarusevych, S., Sullivan, P. E., and Kawall, J. G., "On Vortex Shedding from an Airfoil in Low-Reynolds-Number Flows," *Journal of Fluid Mechanics*, Vol. 632, 2009, pp. 245–271.

[15] Mabey, D.G., "Analysis and Correlation of Data on Pressure Fluctuations in Separated Flow," *Journal of Aircraft*, Vol. 9, No. 9, 1972, pp. 642–645.

[16] Roshko, A., "On the Drag and Shedding Frequency of Two-Dimensional Bluff Bodies," NACA TN-3169, 1954.

[17] Eaton, J.K., and Johnston, J.P., "Low-frequency Unsteadyness of a Reattaching Turbulent Shear Layer," *Turbulent Shear Flows 3*, edited by L.J.S. Bradbury, F. Durst, B.E. Launder, F.W. Schmidt, and J.H. Whitelaw, Springer-Verlag, New York, 1982, pp. 162–170.

[18] Bragg, M.B., Heinrich, D.C., and Khodadoust, A., "Low-Frequency Flow Oscillation over Airfoils near Stall," *AIAA Journal*, Vol. 31, No. 7, 1993, pp. 1341–1343.

[19] Bragg, M.B., Heinrich, D.C., Balow, F.A., and Zaman, K.B.M.Q., "Flow Oscillation over an Airfoil Near Stall," *AIAA Journal*, Vol. 34, No. 1, 1996, pp. 199–201.

[20] Broeren, A.P. and Bragg, M.B., "Flowfield Measurements over an Airfoil During Natural Low-Frequency Oscillations Near Stall," *AIAA Journal*, Vol. 37, No. 1, 1998, pp. 130–132.

[21] Bernardini, C., Benton, S.I., Hipp, K.D., and Bons, J.P., "Large Low-Frequency Oscillations Initiated by Flow Control on Poststall Airfoil," *AIAA Journal*, Vol. 54, No. 5, 2016, pp. 1616-1627.

[22] Ansell, P.J. and Bragg, M.B., "Characterization of Low-Frequency Oscillations in the Flowfield About an Iced Airfoil," *AIAA Journal*, Vol. 53, No. 3, 2015, pp. 629-637.

[23] Zaman, K., Bar-Sever, A., & Mangalam, S., "Effect of acoustic excitation on the flow over a low-Re airfoil", *Journal of Fluid Mechanics*, 182, 1987, 127-148.

[24] Gault, D. E., "A correlation of low speed aerofoil section stalling characteristics with Reynolds number and aerofoil geometry", N.A.C.A. Technical Note 3963. (1957).

[25] Gregory, N., O'Reilly, C. L., "Low-Speed Aerodynamic Characteristics of NACA 0012 Aerofoil Section, including the Effects of Upper-Surface Roughness Simulating Hoar Frost", Aerodynamics Division, N.P.L., London, 1973.

[26] Drela, M., XFOIL, Software Package, Ver. 6.97, Cambridge, MA, 2008.

[27] Barlow, J.B., Rae, W.H. Jr. and Pope, A., "Low-Speed Wind Tunnel Testing," 3rd Edition, John Wiley & Sons, Inc., New York, 1999.

[28] Gupta, R., "Open-Loop and Closed-Loop Trailing-Edge Separation Control on a Natural Laminar Flow Airfoil", Master's Thesis, University of Illinois at Urbana-Champaign, 2016.

[29] Ansell, P. J., "Unsteady Modes in the Flowfield About an Airfoil with a Leading-Edge Horn-Ice Shape", PhD Dissertation, University of Illinois at Urbana-Champaign, 2013.

[30] Dynapar™, Series HS35R Heavy Duty Hollowshaft Encoder, Installation Manual, 2015.

[31] Gurbacki, H. M., "Ice-Induced Flowfield Effects on Airfoil Performance", PhD Dissertation, University of Illinois at Urbana-Champaign, 2003.

[32] Ladson, C. L., "Effects of Independent Variation of Mach and Reynolds Numbers on the Low Speed Aerodynamic Characteristics of the NACA 0012 Airfoil Section", NASA TM No. 4074, October 1988.

[33] Sheldahl, R. E., Klimas, P. C., "Aerodynamic Characteristics of Seven Symmetrical Airfoil Sections Through 180-Degree Angle of Attack for Use in Aerodynamic Analysis of Vertical Axis Wind Turbines", Sandia National Laboratories, SAND80-2114, March, 1981.

[34] Liu, Y., Zhang, J., Wang, H., and Liu, L., "Numerical Bifurcation Analysis of Static Stall of Airfoil and Dynamic Stall under Unsteady Perturbation," *Communications in Nonlinear Science and Numerical Simulation*, Vol. 17, No. 8, 2012, pp. 3427-3434.

[35] Sandham, N.D., "Transitional Separation Bubbles and Unsteady Aspects of Aerofoil Stall," *Aeronautical Journal*, Vol. 112, No. 1133, 2008, pp. 395-404.

[36] Ansell, P.J. and Bragg, M.B., "Unsteady Modes in the Flowfield About an Airfoil with a Horn-Ice Shape," *Journal of Aircraft*, 2015.

[37] Moffat, R.J., "*Describing the Uncertainties in Experimental Results*," Experimental and Thermal Fluid Sciences, Vol. 1, No. 1, 1988, pp. 3–17.

[38] Kline, S. J., and McClintock, F. A., "*Describing Uncertainties in Single Sample Experiments*," Mech. Eng., 3-8 Jan. 1953.

[39] Airy, Sir George Biddle, "*Theory of Errors of Observation*," Macmillan, London, 1879.

[40] Lazar, E., DeBlauw, B., Glumac, N., Dutton, C. and Elliott, G., "*A practical approach to PIV uncertainty analysis*," 27th AIAA Aerodynamic Measurement Technology and Ground Testing Conference, Vol. 28, 2010.